The Effects of Land Surface Heating and Roughness Elements on the Structure and Scaling Laws of Atmospheric Boundary Layer Turbulence

by

Khaled Ghannam

Graduate program in Environment
Duke University

Date: _____

Approved:

_____
Gabriel G. Katul, Supervisor

_____
Amilcare Porporato

_____
James S. Clark

_____
Marcelo Chamecki

_____
Andrew D. Bragg

Dissertation submitted in partial fulfillment of the requirements for the degree of
Doctor of Philosophy in the Graduate School of
Duke University
2017

Abstract

The Effects of Land Surface Heating and Roughness Elements on the Structure and Scaling Laws of Atmospheric Boundary Layer Turbulence

by

Khaled Ghannam

Graduate program in Environment
Duke University

Date: _____

Approved:

_____
Gabriel G. Katul, Supervisor

_____
Amilcare Porporato

_____
James S. Clark

_____
Marcelo Chamecki

_____
Andrew D. Bragg

An abstract of a dissertation submitted in partial fulfillment of the requirements for the degree of Doctor of Philosophy in the Graduate School of
Duke University
2017

Abstract

The atmospheric boundary-layer is the lowest 500-2000 m of the Earth's atmosphere where much of human life and ecosystem services reside. This layer responds to land surface (e.g. buoyancy and roughness elements) and slowly evolving free tropospheric (e.g. temperature and humidity lapse rates) conditions that arguably mediate and modulate biosphere-atmosphere interactions. Such response often results in spatially- and temporally-rich turbulence scales that continue to be the subject of inquiry given their significance to a plethora of applications in environmental sciences and engineering. The work here addresses key aspects of boundary layer turbulence with a focus on the role of roughness elements (vegetation canopies) and buoyancy (surface heating) in modifying the well-studied picture of shear-dominated wall-bounded turbulence. A combination of laboratory channel experiments, field experiments, and numerical simulations are used to explore three distinct aspects of boundary layer turbulence. These are:

- The concept of ergodicity in turbulence statistics within canopies: It has been long-recognized that homogeneous and stationary turbulence is ergodic, but less is known about the effects of inhomogeneity introduced by the presence of canopies on the turbulence statistics. A high resolution (temporal and spatial) flume experiment is used here to test the convergence of the time statistics of turbulent scalar concentrations to their ensemble (spatio-temporal) counterpart. The findings indicate that within-canopy scalar statistics have a tendency to be ergodic,

mostly in shallow layers (close to canopy top) where the sweeping flow events appear to randomize the statistics. Deeper layers within the canopy are dominated by low-dimensional (quasi-deterministic) von Kármán vortices that tend to break ergodicity.

- Scaling laws of turbulent velocity spectra and structure functions in near-surface atmospheric turbulence: the existence of a logarithmic scaling in the structure function of the longitudinal and vertical velocity components is examined using five experimental data sets that span the roughness sub-layer above vegetation canopies, the atmospheric surface-layer above a lake and a grass field, and an open channel experiment. The results indicate that close to the wall/surface, this scaling exists in the longitudinal velocity structure function only, with the vertical velocity counterpart exhibiting a much narrower extent of this range due to smaller separation of scales. Phenomenological aspects of the large-scale eddies show that the length scale formed by the friction velocity and energy dissipation acts as a dominant similarity length scale in collapsing experimental data at different heights, mainly due to the imbalance between local production and dissipation of turbulence kinetic energy.

- Nonlocal heat transport in the convective atmospheric boundary-layer: Failure of the mean gradient-diffusion (K-theory) in the convective boundary-layer is explored. Using large eddy simulation runs for the atmospheric boundary layer spanning weakly to strongly convective conditions, a generic diagnostic framework that encodes the role of third-order moments in nonlocal heat transport is developed and tested. The premise is that these nonlocal effects are responsible for the inherent asymmetry in vertical transport, and hence the necessary non-Gaussian nature of the joint probability density function (JPDF) of vertical velocity and potential temperature must account for these effects. Conditional sampling (quadrant anal-

ysis) of this function and the imbalance between the flow mechanisms of ejections and sweeps are used to characterize this asymmetry, which is then linked to the third-order moments using a cumulant-discard method for the Gram-Charlier expansion of the JPDF. The connection between the ejection-sweep events and the third-order moments shows that the concepts of bottom-up/top-down diffusion, or updraft/downdraft models, are accounted for by various quadrants of this joint probability density function.

To this end, future research directions that build upon this work are also discussed.

Dedicated to my parents, Kamila and Mohammad,

and to my siblings, Mazen, Fatima, Hasan, and Abdallah

Contents

List of Tables

List of Figures

Acknowledgements

My entire Ph.D. and this dissertation would not have been possible if it were not for my parents and siblings. I thank you from the bottom of my heart for always being there for me, supporting me, and sharing my moments of success and failure from thousands of miles away. I owe it all to you; thank you! I would like to thank my advisor, Prof. Gabriel Katul, for giving me the great opportunity of being his student and friend. Gaby, your exceptional mentoring, insight, and inspiration at the personal and professional levels have shaped my thinking and personality. I hope I make you proud, and here's to a long-lasting friendship. Alessandra Trompeo and Gaby, thank you for your kindness and for the fun times at your place.

To my committee members, Prof. Amilcare Porporato, Prof. James Clark, Prof. Andrew Bragg, and Prof. Marcelo Chamecki, thank you for your guidance, discussions, and suggestions. I would like to thank Prof. Marcelo Chamecki for hosting me in his lab at the University of California, Los Angeles, and Dr. Alexandra Konings for hosting me at Stanford University. I am grateful to Prof. Mutasem El-Fadel, my Masters thesis advisor at the American University of Beirut, for his great mentoring and kindness. To my colleagues and friends, Tomer Duman, Cheng-Wei Huang, Tirtha Banerjee, Gabriele Manoli, Salvatore Calabrese, Enrico Zorzetto, Norman Pelak, Maria Blasi, Assaad Mrad, Bijan Seyednasrollah, Fateme Yousefi, Samantha Hartzell, Mark Bartlett, and many others, thank you for everything. Special thanks to Sara Bonetti for a great friendship and for the challenging and fun discussions. I

am also indebted to the wonderful friends Rassil Sayess and Joline El-Chakhtoura.

I appreciate funding from the National Science Foundation (NSF-CBET-103347 and NSF-EAR-1344703), the U.S. Department of Energy (DOE) through the office of Biological and Environmental Research (BER) Terrestrial Ecosystem Science (TES) Program (DE-SC0006967 and DE-SC0011461), the U.S. Department of Agriculture (grant 2011-67003-30222), and the Duke University WISeNet Program sponsored by the National Science Foundation (Grant DGE-1068871).

1

Introduction

1.1 Background and motivation

Almost all problems encountered in natural and engineered environments involve the flow of a fluid, and almost all such flows exhibit aspects of turbulence. Turbulent flows are chaotic and complex fluid motions (consider the smoke rising from a factory stack, flow of a river, wind flow between buildings and trees, or the wake of a ship or aircraft), and their adequate characterization has important implications on improving human well-being. For instance, the design of urban infrastructure and river flow management, air pollution mitigation and atmospheric chemistry, water and carbon exchange between the land surface and the overlying atmosphere, convective rainfall events and flash flood risk management, seed dispersal and gene flow are some settings in environmental sciences and engineering where turbulent flow of air and water is a readily observable phenomenon. While resolving such problems requires an appreciation of their unique attributes, the fundamental nature and complexity of turbulent flow in all of these contexts bears many similarities in such a manner that advances in one problem lend themselves to the others. This relevance

of turbulent flow to such diverse settings has traditionally invited contributions to its literature from mathematicians and physicists, hydrologists, oceanic and atmospheric scientists, environmental engineers and scientists, and mechanical and aeronautical engineers, among others. Nevertheless, owing to its complex multiscale nature, the topic of turbulence remains an active research venue. It is considered prototypical of systems that are far from equilibrium, thereby making turbulence a useful analogy to many human systems (e.g. economic time series). In natural environments, boundary conditions introduce additional difficulties in comparison to controlled laboratory and/or numerical experiments. Of particular interest here is turbulent flow close to a boundary, often referred to as smooth or rough wall-bounded flow and where a boundary-layer emerges as a result of boundary conditions on the flow velocity components. These are the no-slip and no-penetration conditions, i.e. both the longitudinal (streamwise) and vertical (wall-normal) fluid velocity components are zero at the wall/boundary. Such flow configuration is well-studied in laboratory channel flows and numerical experiments, but mapping its arguments to atmospheric flows close to the land surface is still inconclusive. This is the central tenet of this dissertation.

Unlike most boundary layers in engineering applications, the atmospheric boundary-layer (ABL) develops as a result of a combined effect of frictional (exerted by the land surface) and Coriolis (Earth's rotation) forces on large-scale atmospheric motion, often in the presence of density stratification (Monin, 1970). The overland ABL typically extends from the surface to ∼1-2 km in depth, and is therefore dynamically coupled to land surface processes (see Fig. 1.1), where mechanical (shear) and thermal (buoyancy) generation (or destruction) of turbulence play a central role in shaping the diurnal biosphere-atmosphere interactions (Garratt, 1994). Turbulence in the ABL is responsible for vertical mixing of momentum, heat, and other scalars (e.g. CO_2, H_2O, O_3), which in turn, dictates hydrological (e.g. rainfall) (Manoli

et al., 2016), physico-chemical (e.g. air pollution and aerosol deposition and chemistry) (Huang et al., 2014), and ecological (ecosystem function and activity) (Huang et al., 2015) processes. However, the practical importance of turbulence is often met with the lack of its explicit resolution in coarse-scale numerical weather prediction (NWP) and air quality models, hence emphasizing the need for its parametrization in the ABL (Mellor and Yamada, 1982). Besides the computationally-taxing large eddy simulation (LES) models, which themselves do not fully resolve all turbulence scales, the Reynolds-averaged Navier-Stokes (RANS) equations remain the most common and practical modeling approach to predict mean profiles (e.g. momentum and scalar fluxes) in the ABL. Essential to these closure models are the second- and third-order turbulence statistics, such as velocity and scalar variances, skewness, and two-point correlations (Banerjee et al., 2015; Li et al., 2016). The use of statistical moments of turbulence and their connection to the scales of motion (eddy size) has a long history of successful applications in ABL flows (e.g. Deardorff, 1966; Zeman and Lumley, 1976; Ghannam et al., 2017a). However, the perspective that the vertical structure of the ABL (Fig. 1.1) consists of a surface layer (∼100 m above the ground), well-mixed layer (few hundreds of meters), and entrainment zone (tens of meters) each with distinct and well-studied scaling laws is often challenged when i) *the existence of roughness elements such as tall vegetation canopies alters the turbulence properties compared to predictions of surface layer similarity theory* (Monin and Obukhov, 1954), and ii) *the local turbulence statistics at a given height within the ABL are determined by all scales of motion, i.e. transport processes of momentum and scalars are nonlocal.* In other words, modeling ABL flows as canonical turbulent boundary layers (vertically-layered wall-bounded turbulence), consisting of an (i) inner region: ∼ few millimeters above the smooth/rough wall where the action of viscous dissipation is significant, (ii) inertial/intermediate region: ∼ several tens of meters above the inner region in the ABL where the mean velocity follows a logarith-

mic vertical profile, and (iii) outer region: $\sim$ several hundreds of meters above the inertial sublayer, can all be challenged when surface heating and roughness elements introduce modifications to these classical scaling laws. This dissertation is dedicated to explore how these distinct features of ABL flows shape the structure and scaling laws of turbulence in meteorological and ecological contexts. In this respect, laboratory water channel experiments, field measurements, and numerical simulations are used here to gradually navigate different compartments of ABL flows, namely turbulence aspects within vegetation canopies, in the roughness sub-layer (RSL) above vegetation and atmospheric surface layer (ASL) above smooth/rough surfaces, and in the mixed layer (ML) where buoyancy effects are most pronounced (Fig. 1.1).

1.2 Overview

Figure 1.1 provides the outline and context of this dissertation, emphasizing the connection between the fast time scales ($\sim$ seconds to minutes) that characterize turbulent flows in the ABL and the slower (daily to inter-annual) land-atmosphere exchange of energy and matter. The integrated effect of ABL flows therefore dictates the feedbacks between terrestrial ecosystems and the climate, and hence a fundamental understanding of the response of the ABL to surface effects is warranted to quantify such feedbacks. The work here focuses on turbulent flow in different layers of the ABL, and proceeds from within-canopy turbulence in Chapter 2, to the scaling laws and structure of near-neutral flows in the roughness sublayer (Chapter 3), and the nonlocal transport of heat in the mixed layer under convective (buoyancy-dominated) ABL flows in Chapter 4. Specifically, the organization is as follows

- **Chapter 1** introduces the importance of understanding turbulent flows in the context of land-atmosphere interactions. It also introduces salient features of ABL flows that challenge the classical picture of shear-dominated wall-bounded turbu-

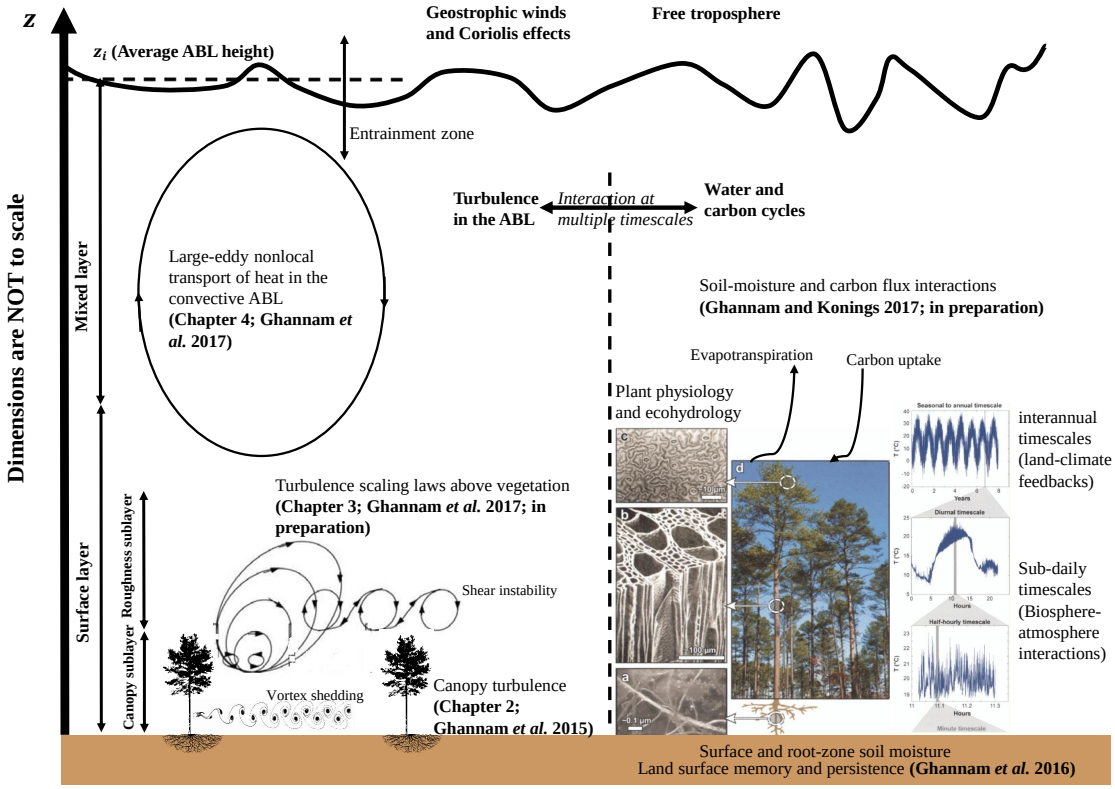

FIGURE 1.1: Left: Schematic diagram of the structure of the ABL in the presence of tall roughness elements (vegetation canopies) and when surface heating (buoyancy) is active. This is the focus of the dissertation here (see citations in the left panel within and above the canopy and in the mixed layer of the ABL). Right: connection between turbulence in the ABL and biosphere-atmosphere exchange (water and carbon transport in the soil-plant-atmosphere continuum) to emphasize their coupling at multiple timescales. Key: ABL=Atmospheric Boundary Layer.

lence, namely the existence of tall roughness elements that are porous and surface heating (buoyancy). This sets the discussion into a need to probe the vertical structure of the ABL in contrast to canonical turbulent boundary layers, hence establishing the three subsequent chapters as different aspects that advance the understanding of boundary-layer meteorology.

- **Chapter 2** discusses the role of flow inhomogeneity introduced by vegetation canopies in affecting the turbulence statistics in the context of the validity (or lack thereof) of the ergodic hypothesis. A high-resolution laser-induced fluorescence

flume experiment is used to examine whether the temporal and spatial statistics of scalars within the canopy converge to each other. The results are published in Ghannam et al. (2015).

- **Chapter 3** focuses on the scaling laws of turbulence directly above vegetation canopies. Several field experiments conducted in the roughness-sublayer of dense canopies are contrasted with atmospheric surface layer experiments under near-neutral (negligible buoyancy) conditions to explore how the additional length scales introduced by canopies affect the correlation structure and scaling laws of turbulent velocities. The results are under peer review in the Journal of Atmospheric Sciences (Ghannam et al., 2017b).

- **Chapter 4** isolates the effects of roughness elements and retains surface forcing only as it pertains to the role of buoyancy in the failure of the gradient-diffusion (K-theory), and hence in nonlocal transport of heat in the mixed layer. Numerical Large Eddy Simulation (LES) runs spanning unstably stratified to convective ABL flows are used to examine the role of large-scale eddies of size comparable to the ABL depth in this nonlocal transport. The results are published in Ghannam et al. (2017a).

- **Chapter 5** summarizes these findings and provides an outlook on future research directions that build upon these published results.

The coupling between ABL flows and land-atmosphere interactions also necessitated some understanding of surface hydrology and ecology to complement the work at much longer time scales. These complementary aspects of biosphere-atmosphere exchange already appeared in Ghannam et al. (2016) and Ghannam and Konings (2017) and are not included in this dissertation.

1.3 Intellectual merit and broader impacts

The parametrization of ABL turbulence in current mesoscale and climate models relies on Mellor-Yamada schemes that use a 'master' length scale (often selected as the distance to the boundary) for describing variations in the production, dissipation, and redistribution of energy, momentum and scalars. This convenience is driven by the fact that the scales of ABL flows and their connection to the statistics of turbulence remain challenging, especially in contexts of predictive modeling in the presence of roughness elements. However, the nonlocal character of momentum and scalar transport within the ABL (shortcomings of K-theory) has necessitated a global perspective on ABL flows, where the flow statistics are affected by all scales of motion including entrainment and roughness sublayer effects. Addressing these challenges requires a combination of field and laboratory measurements in addition to models to examine different features of ABL flows. Here, several data sets presented an opportunity to investigate the effects of dense canopies on flow features, and combined with the mathematical and statistical theory of turbulence, unfolded the scaling laws that are distinct from typical surface layer turbulence used in Mellor-Yamada schemes. The role of coherent structures such as von Kármán vortices and the ejection-sweep events in determining the dispersion of scalars within canopies is an important attribute that is relied upon here to reduce the dimensions and complexity of the problem.

The outcome of this work can be directly used to enhance the representation of turbulence in numerical weather prediction (NWP) and air quality models by introducing multiple length scales needed to capture the rich dynamics associated with ABL and canopy flows. Problems related to spore dispersion within vegetation canopies, heat and momentum flux parametrization, ozone deposition onto forests, and nutrient transport within submerged vegetation are particular applications that

benefit from such improvements. These outcomes, used as dissertation chapters here, are (or will be) published in peer-reviewed academic journals and presented at international conferences.

2

The spatio-temporal statistical structure and ergodic behavior of scalar turbulence within a rod canopy

2.1 Introduction

The ergodic hypothesis was first introduced by Boltzmann in 1871 in the study of equilibrium statistical mechanics. It states that in the course of sufficiently long time, the phase trajectory of a closed system of interacting particles described by a macrostate (distribution of microstates), revisits (or passes arbitrarily close to) every phase point in the manifold (Landau and Lifshitz, 1980). In other terms, the time average of some observable settles to an equilibrium value when the system 'forgets' its initial state, and becomes equivalent to a true (ensemble) average. In the context of turbulent flows, the ergodic hypothesis is often invoked when inquiring about the statistics of an ensemble from routinely measured temporal statistics in field or laboratory settings. In its strictest definition within the statistical fluid mechanics community, the hypothesis states that the temporal/spatial statistical moments converge to those of an ensemble of statistically stationary/homogeneous

flows when the sampling is sufficiently long for the flow to experience all possible independent realizations (Monin and Yaglom, 1971; Stanisic, 1985). Hence, when the flow establishes a statistically steady state, temporal and/or spatial statistics of a measured turbulence quantity such as concentration converge to those of an ensemble by averaging over intervals much longer than the integral scales, provided the corresponding auto-correlation function decays to zero at finite lags (and remains so).

Numerous studies have examined the validity, or lack thereof, of the ergodic hypothesis across a wide range of turbulence problems, both theoretically and experimentally. Support for the hypothesis has been reported using direct numerical simulations (DNS) of the Navier-Stokes (N-S) equations for statistically stationary and homogeneous flows (DaPrato and Debussche, 2003; Galanti and Tsinober, 2004). In laboratory studies, the ergodic hypothesis has also been explored using velocity time series measurements in a channel with repeated independent yet similar experiments (Lesieur, 1990), while Mattingly and Weinan (2001) and Constantin et al. (2013) addressed its theoretical validity on N-S equations in a stochastic setting. In field measurements, Higgins et al. (2013) and Chen et al. (2014) recently examined the minimum requirements of ergodicity of atmospheric water vapor measurements over a land-lake interface and that of eddy correlation flux measurements, respectively. Nevertheless, the lack of simultaneous temporal and spatial realizations, especially inside canopies, largely limits proper testing of the validity of the ergodic hypothesis. Time averaging thus remains the common framework when reporting the statistical properties of atmospheric turbulence with spatial patterns retrieved using Taylor's frozen turbulence hypothesis (Taylor, 1938a) whenever applicable (Higgins et al., 2012).

Turbulence near and within roughness elements such as canopies are drawing increased interest given their prevalence in biosphere-atmosphere studies of gas ex-

change (e.g. CO_2 and water vapor transport) (Finnigan, 2000a), ecological studies of seed and pollen spread (Nathan et al., 2002), and air quality studies such as the transport of ammonia (Sutton et al., 1995), to name a few. Turbulent flows within canopies exhibit features that distinguish them from their classical boundary layer counterpart. The work that the flow exercises against the foliage drag produces turbulent kinetic energy (TKE) by wakes that leads to a spectral short-circuiting of the energy cascade (Finnigan, 2000a; Poggi et al., 2006, 2008). Previous flume and flow visualization experiments showed that the organized vortical motion within the deep layers of a rod canopy originate from quasi two-dimensional von Kármán vortex streets (Poggi et al., 2004c,a, 2011). The shedding frequency of these vortices is encoded in the classical dimensionless Strouhal number ($St = fd_r/\overline{u}$), where f is the vortex shedding frequency, d_r is a characteristic length scale of the obstacle (here rod diameter of the model canopy), and $\overline{u}$ is the mean streamwise velocity. The impact of the aforementioned canopy-induced phenomena on the spatio-temporal statistics and possible ergodic behavior of passive scalar statistics remains unexplored and frames the scope of this work. The usefulness of such a discussion is evident when interpreting the statistical moments of turbulence quantities measured in laboratory and field campaigns as representative of theoretical ones, and to the subsequent comparison of such measurements with simulations or models. In essence, the gap between the temporal measurements at a point and the spatio-temporal extent of the equations of motion governing fluid flows requires an understanding of the conditions under which the two converge.

To this end, within-canopy laser induced fluorescence (LIF) measurements of dye concentration are used to examine aspects of the ergodic structure of concentration statistics at two different depths. The image processing of LIF measurements provides a practical framework for the concept of 'similar experiments' where spatial and temporal fields are used as proxies for multiple experiments repeated under sim-

ilar external forcing. Spatial realizations at a time and temporal realizations at a point are discussed through the corresponding correlation functions, integral scales and statistical independence in comparison to characteristic time and length scales associated with physical phenomena such as the size and frequency of von Kármán vortex streets, and the mean return period of sweeping events from the canopy top. The Kolmogorov-Smirnoff (KS) statistical test is used to evaluate the degree of convergence of each of the spatial and temporal statistics to those of an ensemble of realizations constructed from statistically quasi-independent events. This evaluation determines whether the constructed ensemble distribution represents a transposition of temporal to spatial statistics and *vice versa*. Such a transposition is also explored by computing a local eddy velocity that communicates within-canopy temporal realizations at a given location to downstream locations but with finite time lag. Using cross-correlation analysis of concentration time series at two points in the canopy space, a local advection velocity can also be retrieved and compared to published Laser Doppler Anemometry (LDA) measurements conducted for the same rod-canopy setup (Poggi et al., 2004c).

2.2 Experimental Facilities

The data used in this work were collected from an open channel flow experiment with canopy-like roughness introduced as vertical rods mounted to the bottom wall of the channel. The flume configuration, the rod canopy, the acquisition of the scalar concentration time series, and the data processing are presented elsewhere (Poggi et al., 2002, 2004c,a, 2008; Poggi and Katul, 2006). In brief, the experiment was carried out in a large rectangular constant head recirculating channel, 18 m long, 0.9 m wide, and 1 m deep with glass side walls to permit the passage of laser light. The rod canopy was composed of vertical stainless steel cylinders 0.12 m tall ($= h$) and 4×10^{-3} m in diameter ($= d_r$), arrayed in a uniform square pattern at $n_p = 1072$

rods m^{-2}, where n_p is the canopy density defined as the number of rods per unit ground area. Using h, d_r, and n_p, the effective frontal area index is 0.81 m^2 m^{-2}. The large n_p resulted in $C_d \approx 0.3$ comparable to those reported for agricultural crops and dense forests (Katul et al., 2004).

The local instantaneous dye concentration in a plane parallel to the channel bottom was measured using the laser-induced fluorescence (LIF) technique. The concentration measurements were conducted by (i) injecting Rhodamine 6G as a tracer, (ii) providing a horizontal light sheet between two lines of rods using a lens system, and (iii) recording a time sequence of images. The light source was provided by a 300 mW continuous fixed wavelength ion-argon laser (Melles Griot mod. 543-A-A03), and the images were recorded at a frequency of 30 Hz using a color CCD (Charge-Coupled Device) video camera (Poggi and Katul, 2006; Poggi et al., 2006). Digital movies with a spatial resolution of 170×10^{-6} m were collected at two levels: $z/h = 0.2$ and $z/h = 0.5$, where z is the vertical distance referenced to the channel bottom. Three 72 s video sequences for each of the two depths were then used to compute instantaneous two-dimensional planar concentration. Throughout, the heights $z/h = 0.2$ and $z/h = 0.5$ are referred to as 'deep' and 'mid-canopy' layers. In addition, the measurements were collected at two bulk canopy Reynolds numbers, $Re_* = u_* h/\nu$ of 6000 and 12000, where $u_* = (-\overline{u'w'})^{1/2}$ is the friction velocity measured at $z/h = 1$, primed quantities are turbulent excursions, and the overbar indicates time averaging over the sampling duration. The results for the two Reynolds number were similar and the subsequent analysis uses only the $Re_* = 6000$ dataset.

It is noteworthy that while the sampling resolution is much higher in space than in time (around 15 times), the temporal sample size is much longer and thus time statistics should have higher convergence. Figure 2.1 shows the ensemble-averaged temporal and spatial spectra of the measured concentration series $(z/h = 0.2)$, where the latter was transformed from a wavenumber to frequency domain by the inde-

pendently measured spatially and temporally averaged velocity reported elsewhere (Poggi et al., 2004c). Clearly, the spatial spectrum resolves much higher frequencies than its temporal counterpart but the two have similar limited 'scaling' at the overlap frequency. Hence, the ensemble of spatio-temporal realizations of concentration measurements covers a wide range of turbulent scales that are not necessarily overlapping for most frequencies.

2.3 Methodology

Because canopy flows are inhomogeneous in z, it is unlikely that ergodicity applies in a manner similar to previously studied cases obtained for flows with homogeneous coordinates (DaPrato and Debussche, 2003; Galanti and Tsinober, 2004). However, connections between temporal and spatial statistics for such a complex flow may still be explored for some distance from the boundary (i.e. in a plane parallel to the mean flow at a given z/h), and at some position far from canopy elements. This is the main guiding principle for the analysis conducted here. Two different aspects of scalar concentration statistics are analyzed at each z/h: one that is based over the entire planar flow field at a certain moment in time t; and another for one position in space over a long period of time. If canopy scalar turbulence is ergodic, these two types of statistics should converge. Lack of convergence can also be viewed as evidence against the ergodic hypothesis (operational or otherwise strict) within canopies. However, convergence of these two types of statistics cannot be used as evidence for the validity of ergodicity as such convergence is only necessary but not sufficient.

The LIF images cover one rod spacing in the streamwise direction. Hence, the spatio-temporal measurements are confined to what is referred to hereafter as the 'one-cell configuration' - a square domain between four corner rods. This one-cell configuration occurs periodically in uniformly-spaced dense canopies, and closely

resembles a domain with homogeneous coordinates for the flow field. Within such a configuration, once the flow impinges on such a cell, wakes are generated behind the upstream rods and unless disrupted by a sweeping event from the canopy top, tend to grow in size until experiencing collisions with their downstream rods counterpart. It is this alternating character of persistent and spatially coherent von Kármán vortex streets and sweeping events that the current work seeks to examine as to how it alters the concentration statistics in general and necessary conditions for 'operational' ergodicity in particular. The spatial dimension of the planar images is 171×221 (longitudinal x lateral) locations sampled 2100 times (around 72 s). While the same experiment is repeated three times at each of the two depths ($z/h = 0.2$ and $z/h = 0.5$), our analysis showed no significant differences among the replicates and the subsequent discussion illustrates the results from one experimental run at each of the two z/h.

The expansive dataset (array of $171 \times 221 \times 2100$) can be viewed as two configurations under similar external flow conditions (uniform water level, steady flow rate, fixed rod arrangement, and comparable initial conditions for dye releases). The first is a series of spatial realizations at each moment in time (i.e. 2100×221 spatial series each of length 171 points), while the second is 171×221 spatial locations that sample a concentration time series for about 72 s.

When discussing integral (temporal or spatial) scales of the flow, concentration excursions (C') from the local (temporal or spatial) mean are used instead of concentration differences (ΔC) so as to compare with well-established length and time scales associated with canopy turbulence and eddy sizes. Also, the maximum integral length and time scales are used as surrogates for delineating statistical independence of spatial and temporal realizations. While not necessarily exact, the choice of the maximum integral timescale (out of 171x221 available scales) to separate temporal events and maximum length scale (out of 221x2100 available scales) to separate spa-

tial events may warrant independence. Such maximum values of length and time scales are $5 - 10$ times their corresponding average value. When evaluating several operational aspects of ergodicity (mainly the KS test for distributions), it is more convenient to consider spatial or temporal differences in LIF concentration (ΔC) (Galanti and Tsinober, 2004) instead of concentration excursions from an arbitrarily set average for both configurations. The choice of concentration difference (in time or space) rather than absolute concentration excursions eliminates some potential effects of non-stationarity and inhomogeneity in the mean concentrations and dominant low frequency/wavenumber scales. Also, LIF measures light intensity rather than absolute concentration and any minor differences in background light intensity across experiments might become less relevant to concentration differences. The differencing operation itself tends to partly 'de-correlate' the series (at least less correlated than C') (Katul et al., 2001), which then reduces its integral scales when constructing ensembles and convergences of spatial and temporal averaging to ensembles.

Figure 2.2 shows typical 2-D images at the two depths during periods where the flow is dominated by von Kármán vortices along with a time series of $\partial C/\partial t \approx \Delta C/\Delta t$ and $\overline{u}\partial C/\partial x \approx \overline{u}\Delta C/\Delta x$, where $\overline{u}$ is the measured planar- and time-averaged streamwise velocity at the two depths (0.08 and $0.1 m/s$ at $z/h = 0.2$ and $z/h = 0.5$, respectively) presented elsewhere (Poggi et al., 2011). Here, $\Delta t = (1/30)$ s and $\Delta x = 170 \times 10^{-6}$ m. The probability density functions (pdf) of these series (see bottom panel of Fig. 2.2) exhibit a wider spread, particularly in time, relative to a standard Gaussian distribution. The discrepancies between the two distributions can be attributed to the use of the mean velocity rather than the time series of the local velocity, where the former tends to mask extreme events and therefore misses the tails in the distribution, yet constitutes the basis of Taylor's frozen turbulence hypothesis.

2.4 Results and Discussion

To address the study objective, the spatio-temporal ensemble at the deep and mid-canopy layers must first be constructed from sub-sampling the differenced concentration (ΔC) series at each z/h so as to ensure replications of independent realizations. Next, the temporal pdf at each location (and z/h) and the spatial pdf at each moment in time (and z/h) are compared against the ensemble. It is for this reason that the integral time and length scales of C are first computed and discussed, followed by the construction of the ensembles of ΔC at each z/h. Comparisons between spatial or temporal statistics of ΔC to the constructed ensemble pdf are also presented based on the KS test. The transposition of spatial statistics to their temporal counterparts is further explored (at each z/h) by computing local eddy velocity that communicates time realizations at a given location to downstream locations but with finite time lag. Using cross-correlation analysis, a local advection velocity was retrieved and its statistics are compared to independent LDA velocity measurements conducted for the same configuration and z/h as reported elsewhere (Poggi et al., 2004c).

2.4.1 Integral scales

The integral timescales of C over the spatial domain (top panel in Fig. 2.3) show longer temporal memory near the obstacles compared to all other downstream locations (for each z/h). Also, longer memory prevails in the deeper layer when compared to its mid-canopy counterpart. The maximum correlation in time was 3.2 and 1.4 s in the deep and mid-canopy layers, respectively. This result is not surprising given that the vortex streets in the deeper layer persist longer because they are less frequently disrupted by sweeping events from aloft. To the contrary, integral length scales are somewhat larger in the mid-canopy region. Also, there is no difference between near-obstacle spatial correlation and elsewhere (see Fig. 2.3) at a given z/h.

The maximum spatial correlation is around 5×10^{-3} m (rod spacing is 30×10^{-3} m and rod diameter is $d_r = 4 \times 10^{-3}$ m) and such high correlation values appear to occur during sweeping events that perturb the dominant vortical motion. Figure 2.4 shows the corresponding probability density functions of the integral time (τ) and length (l) scales normalized by h/u_* (where $h = 0.12$ m is the canopy height and $u_* = 0.045$ m s^{-1} is the friction velocity at the canopy top). The timescale h/u_* (≈ 2.67 s) is a measure of periodicity of sweeping events from the canopy top, and it often exceeds the correlation time τ at the two z/h (i.e. sweeps frequently disturb persistent vortex streets).

The ensemble pdf was constructed by taking a sub-sample of the ΔC data set. This subset consists of all spatial and temporal ΔC realizations that are separated by the maximum auto-correlation length and time scales (inferred from C not ΔC), so that each point may be viewed as an independent sample. Both ensembles for the two z/h are shown in Fig. 2.5. The ensemble pdf at $z/h = 0.2$ has a heavier tail than that at $z/h = 0.5$. It is to be noted that the integral statistics of ΔC (both spatial and temporal) are much smaller than their C counterparts, so that using the maximum integral scales of C when constructing the ensemble ensures stronger statistical independence.

2.4.2 Temporal and spatial statistics

To test the statistical similarity between the ensemble and temporal distributions of concentration, the KS test is performed for each time series (171×221 series) against the ensemble pdf. The KS test is a nonparametric test that quantifies the maximum distance between the cumulative distribution functions of two samples without any prior assumptions about the distributions. The result of the KS test is binary (0 or 1) H values with H=1 corresponding to rejecting the null hypothesis that the two pdfs originate from the same distribution at the 95% confidence level. Close to the

boundary, the temporal distribution of concentration difference is not captured by the ensemble pdf at $z/h = 0.2$ (Fig. 2.6), while all other time realizations (including higher order statistics) are represented by the spatio-temporal transposition. Figure 2.6 also shows that the mid-canopy layer exhibits a stricter ergodic behavior, where H values are almost zero everywhere. Note that while the ensemble realizations are drawn from uncorrelated (statistically independent) samples, the KS test is conducted for all time series (171×221). A drawback of conducting the KS test on all series is that the test includes some correlated events. On the other hand, the KS test is being conducted on a much more expansive set of concentration differences not used in the computation of the ensemble.

Figure 2.7 shows the similar analysis for spatial series against the ensemble. Each point in the plot is a binary result of the KS test of a spatial pdf sampled at a particular time and compared to the same ensemble pdf. While the spatial realizations are not fully ergodic, H=0 still dominates the statistical test during most times, especially in the deeper layer. The H=1 regions in Fig. 2.7 (red color) appear during relatively long periods of sweeping events, where the dye concentration almost approaches zero (i.e. the dye is entirely washed by sweeps). This is more evident in the $z/h = 0.5$ layer where sweeping events are more frequent.

A plausible explanation for broken ergodicity in the temporal statistics within the deeper layer (left panel of Fig. 2.6) and the spatial statistics in the mid-canopy layer (right panel of Fig. 2.7) may be attributed to the relatively larger integral time scale in the former and larger integral length scale in the latter. Such long correlation reduces the sample size of available independent realizations in time and space domains, which is missed when constructing the ensemble distribution.

2.4.3 Cross-correlation and advection velocity

The cross-correlation function between time series sampled at the first location (sensor) in the one cell configuration and all downstream locations was determined so as to compute an advection velocity that can be compared to velocity measurements conducted using LDA. While the peak of the cross-correlation function decays with increased downstream distance, the lag (in time) at which this peak occurs increases. Figure 2.8 shows the results where the peak in cross-correlation function (top panel) remains significant despite decaying in space. This slow decay and finite cross-correlation indicates that the quasi-deterministic vortical structure (i.e.von Kármán streets) can expand beyond the one cell domain and remain sufficiently coherent. For example, in the deeper layer ($z/h = 0.2$), the decrease of the cross-correlation with increasing spatial lags varies from 1 to 0.7, which is still significant. The maximum time lags are 0.7 and 0.5 s at $z/h = 0.2$ and $z/h = 0.5$, respectively. The average time for a uniform von Kármán vortex to cover a distance of one rod spacing is around 0.3 s, while the periodicity of shedding such vortices is around 0.2 s.

The advection velocity calculated from the above analysis is shown in the bottom panel of Fig. 2.8. On average, this calculation captures the mean streamwise velocity measured and reported by Poggi et al. (2004c) and Poggi et al. (2011) (around 0.08 and 0.1 m s^{-1} at $z/h = 0.2$ and $z/h = 0.5$, respectively). More important here is the pdf of these velocities that is shown in Fig. 2.9 along with the LDA velocity measurements in Poggi et al. (2004c). The reasonable agreement here suggests that the advection velocity may be inferred from scalar concentration statistics through a spatio-temporal transposition, which is consistent with an operational view of the ergodic hypothesis.

2.5 Conclusions

High resolution spatio-temporal datasets of within-canopy scalar concentration measurements were collected to examine necessary conditions for ergodicity. While limited in experimental scope (due to the sampling length in time and space), the current work is the first to examine the ergodic hypothesis on scalar turbulence statistics within canopies. The main premise when analyzing this data set is that if a turbulent flow is both statistically stationary in time and homogeneous in space, then its temporal and spatial statistical properties should be the same if the ergodic hypothesis is correct. Canopy turbulence is inhomogeneous in the vertical direction necessitating a modification to this premise. The proposed modification here replaces spatial with planar statistical properties defined at a given z/h. Even with this modification, the presence of rods may still break ergodic behavior because canopy turbulence in the deeper layers of the canopy appears to be dominated by low-dimensional (or even quasi-deterministic) motion (von Kármán vortex streets) that cannot be ergodic. However, frequent sweeps from aloft occasionally disturb the onset of such motion, and other mechanisms responsible for the breakdown of these von Kármán vortices (e.g. their subsequent collision with other rods) may produce fine-scaled turbulence that is locally homogeneous away from the rods. These other mechanisms may act to restore ergodicity but within a smaller or restricted spatial domain.

The experimental results here show a general tendency towards the validity of this operational version of the ergodic hypothesis, particularly for temporal statistics and in the mid-canopy layers where sweeps tend to frequently disturb the onset of von Kármán streets. Events associated with broken ergodicity were related to (i) sweeping and dye washing that homogenized the spatial domain (an unavoidable experimental limitation) or (ii) long memory in time near physical obstacles that prohibit proper testing of the hypothesis due to insufficient sampling of statistically in-

dependent events. However, even within the single-cell, the pdf of the independently measured LDA advection velocity was reasonably recovered from cross-correlation functions of concentration time series lagged in space. This agreement suggests that the transposition of spatio-temporal scalar concentration statistics in turbulent flows within canopies can still be achieved by a local advection velocity. Hence, it can be surmised that scalar canopy turbulence does exhibit similarity between its temporal and spatial statistical properties. This transposition is deemed as necessary but not sufficient for accepting operational ergodicity within canopies.

Broader implications of these findings pertain to how combined eco-physiological and canopy transport models are compared to tower measurements. Comparisons between tower-based measurements and modeled scalar (or momentum) flux calculations are often presented using ensemble-averages, where ensemble averaging is often conducted over many days but presented by time of day (presumably reflecting similar light conditions) or by atmospheric stability class (Baldocchi and Meyers, 1998; Katul and Albertson, 1998). The work here suggests that such a representation may be theoretically more sound than comparisons by individual events whose duration is 30 minutes or so. Conducting time and some ensemble averaging over 'similar' conditions (be they light regimes or atmospheric stability classes) is likely to converge to the spatio-temporal average over which the combined eco-physiological and canopy transport models are derived from (if operational ergodicity is assumed). Hence, the work here provides some support to the recent approaches to model-data comparisons and assessments, where ensemble averaging over similar conditions (or hydro-meteorological states) is now commonly practiced in canopy turbulence studies (but without strong rationale).

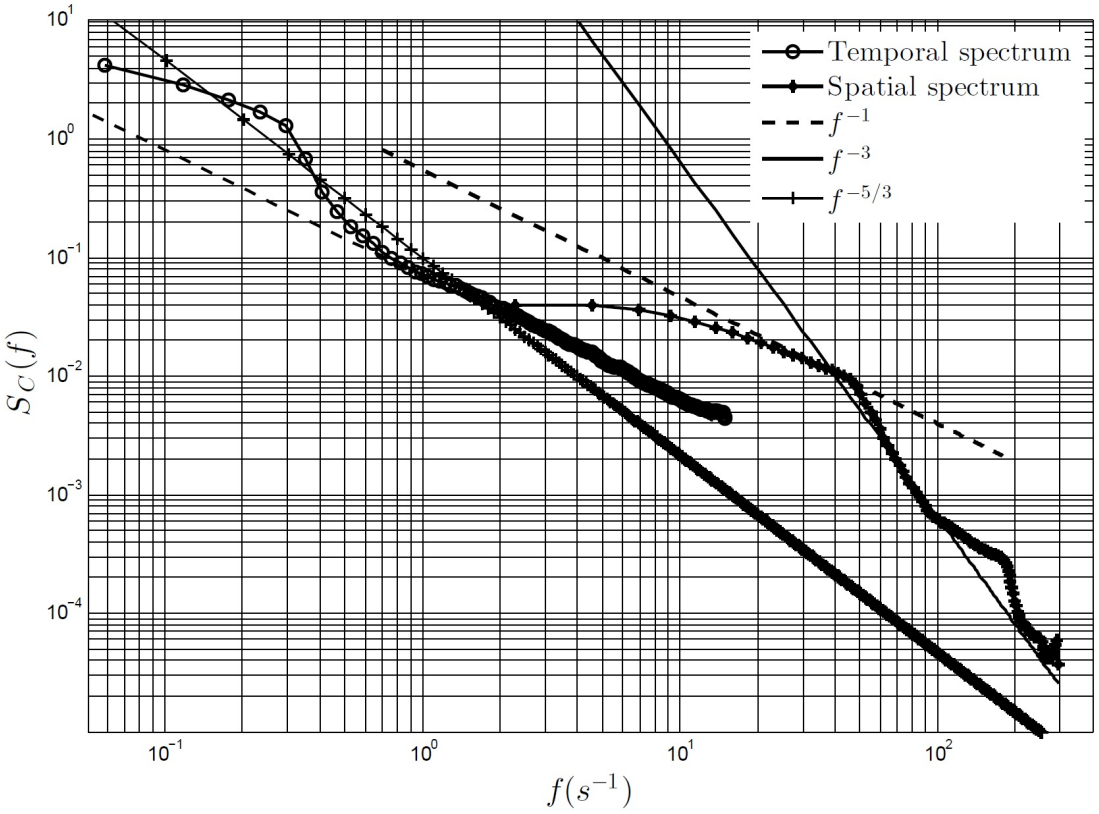

FIGURE 2.1: Ensemble-averaged temporal (171×221 time series) and spatial (221×2100 spatial series) power spectra of concentration fluctuations. The spatial spectrum was transformed into a corresponding temporal spectrum by the relation $f = \overline{u} \times k$, where k is the wavenumber (inverse of spatial resolution), $\overline{u}$ is the average streamwise velocity (≈ 0.1 m s^{-1}) and f is the frequency (s^{-1}). The linear (log scale) fits for parts of the spectra are also shown to emphasize the overlapping regions (f^{-1}). The f^{-3} scaling of the spatial spectrum reported in Poggi et al. (2011) and the Kolmogorov ($-5/3$) scaling are also shown. The high frequency component of the spatial spectrum reveals the effect of pixel size (high spatial resolution).

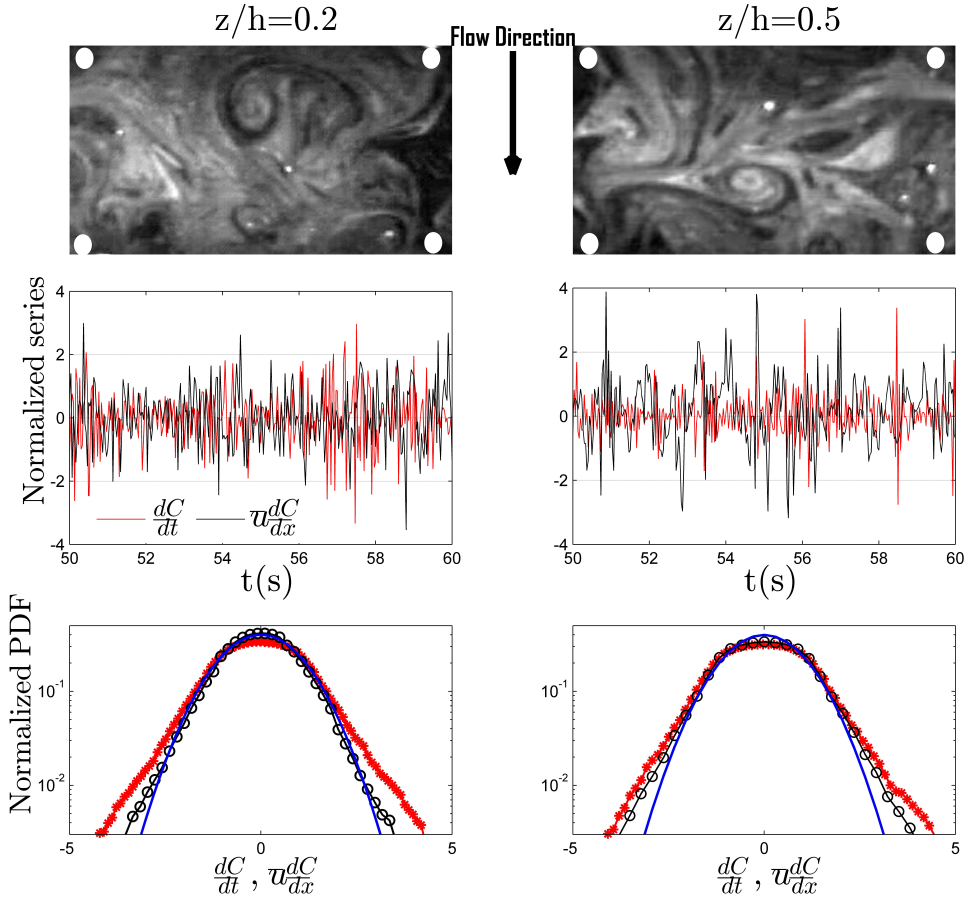

FIGURE 2.2: Top panel: 2D images of the flow field at the two depths ($z/h = 0.2$ and 0.5) during quiescent von Kármán vortex events. White circles denote rod locations. Middle panel: Typical normalized time series of $\Delta C/\Delta t$ (red color) and $\overline{u}\Delta C/\Delta x$ (black). Bottom panel: The normalized pdf of the time series shown in the middle panel with a Gaussian pdf shown for reference (blue line).

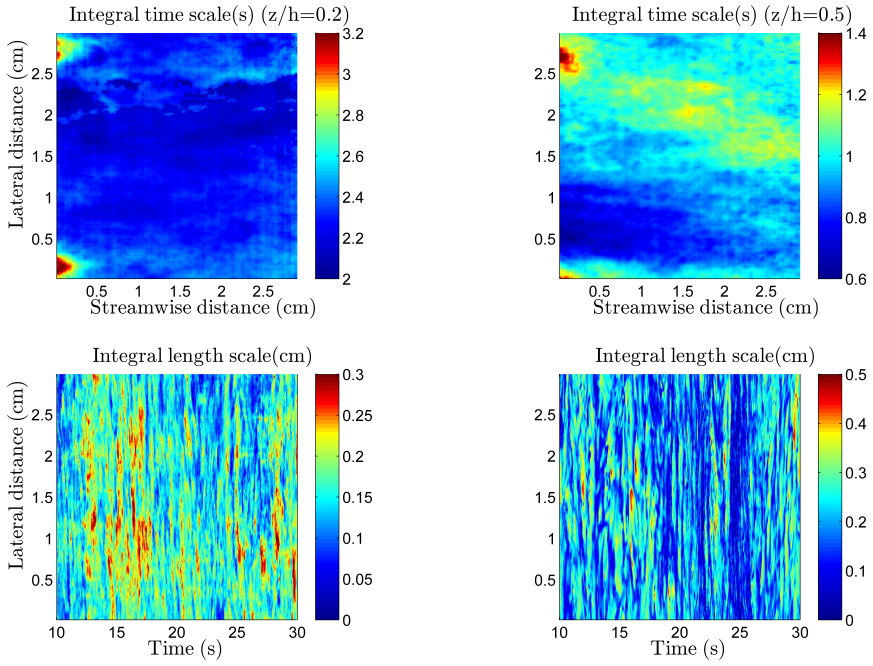

FIGURE 2.3: Integral time (τ) and length (l) scales estimated from zero-crossings of temporal and spatial auto-correlation functions, respectively. Top panel: A total of 171×221 time series were analyzed. The flow direction is from left to right. Bottom panel: Evolution of integral length scale over a 20 s time interval. At a given time (each image), a total of 221 spatial series each of length 171 points downstream.

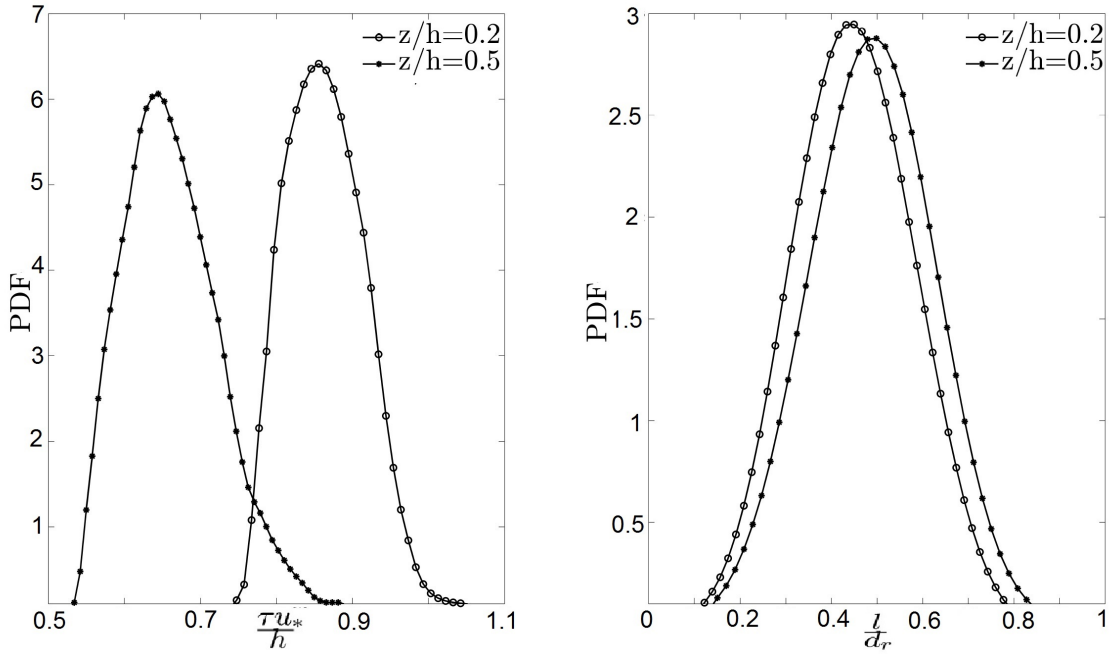

FIGURE 2.4: The PDF of integral time (τ) and length (l) scales normalized by h/u_* and d_r respectively. The h is the canopy height, u_* is the friction velocity at canopy top, and d_r is rod diameter.

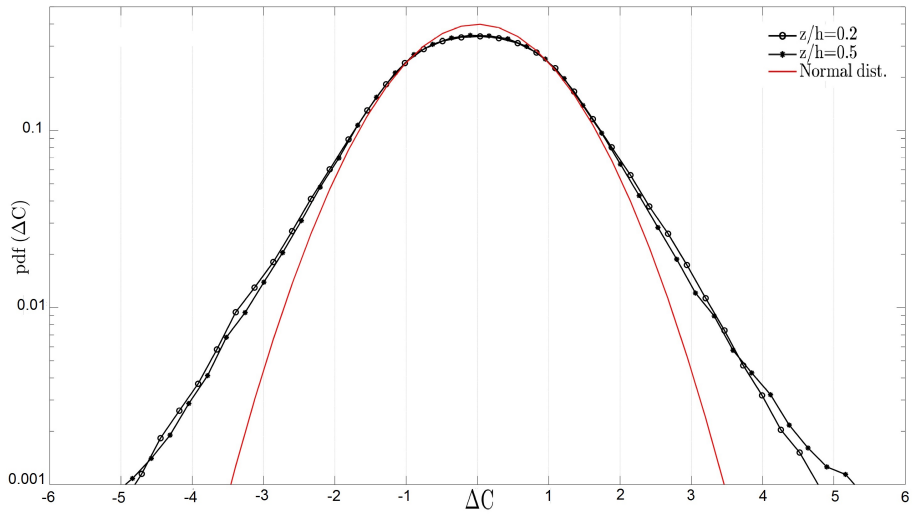

FIGURE 2.5: The pdf of the ensembles of independent spatial and temporal realizations of concentration differences at the two depths $z/h = 0.2, 0.5$, with Gaussian distribution shown for reference.

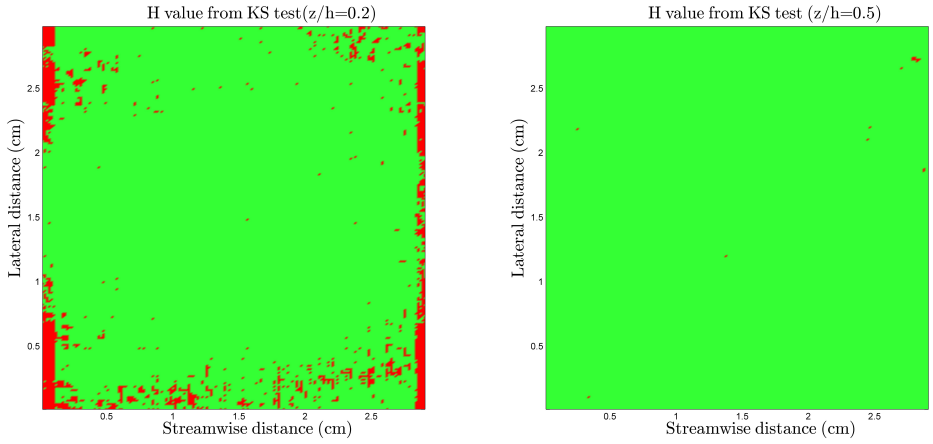

FIGURE 2.6: Binary result of the Kolmogorov-Smirnoff test when comparing the pdf of each time series at each z/h against the corresponding ensemble pdf. The H value is binary and is 0 (green color indicates that the null hypothesis cannot be rejected at the 95% confidence interval) or 1 (red color indicates that the null hypothesis can be rejected at the 95% confidence interval).

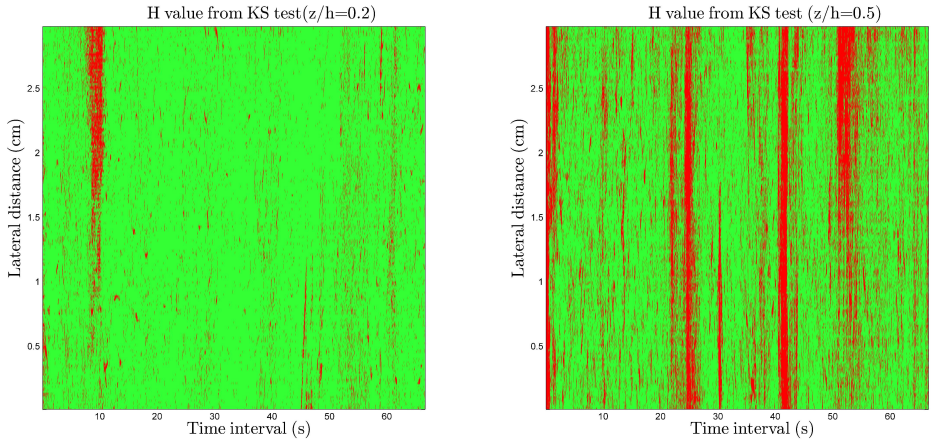

FIGURE 2.7: Binary result of the Kolmogorov-Smirnoff test comparing the distribution of each spatial series at each depth against the corresponding ensemble distribution. The H value is binary and is 0 (green color indicates that the null hypothesis cannot be rejected at the 95% confidence interval) or 1 (red color indicates that the null hypothesis can be rejected at the 95% confidence interval.

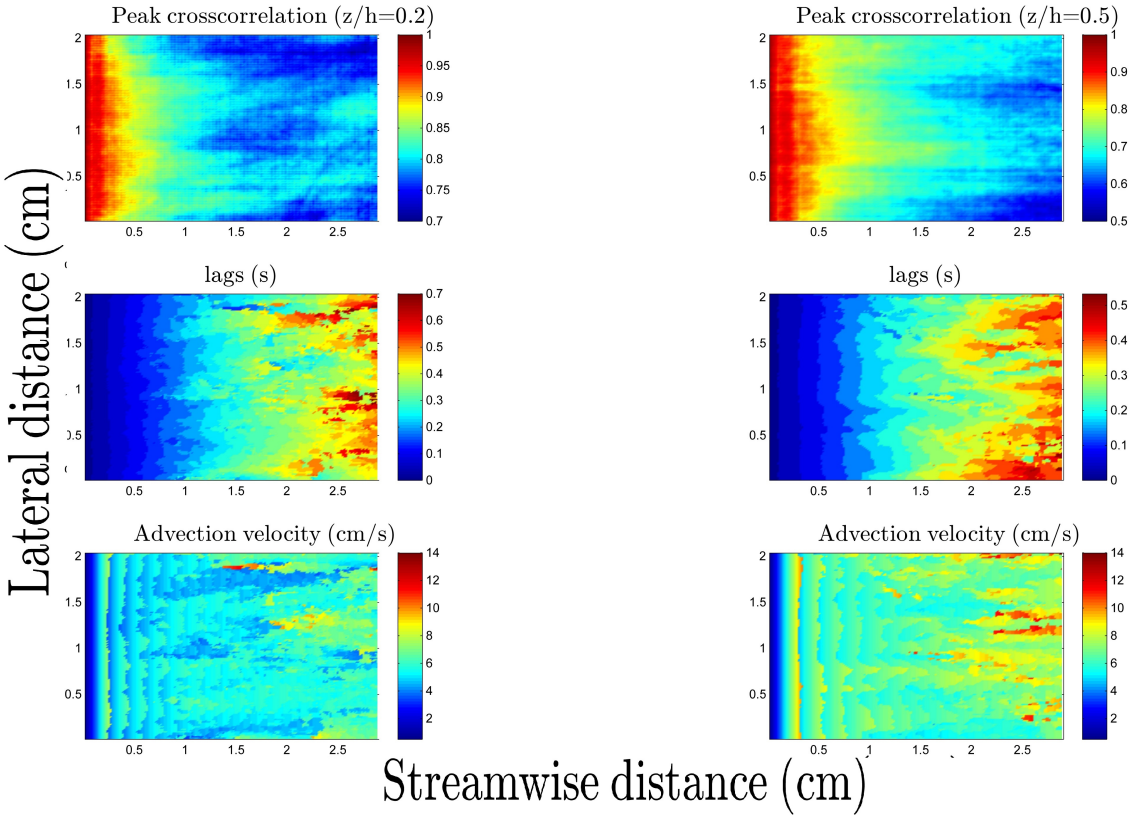

FIGURE 2.8: Lagged cross-correlation of time series in space. Top panel: Peak of the cross-correlation function between time series at the first point with all the downstream time series (170 downwind time series). Middle panel: time lag at which the peak in the cross-correlation function occurs. Bottom panel: Advection velocity calculated as the ratio of the distance between the first location and any downstream location to the corresponding lag in the peak of the cross-correlation function.

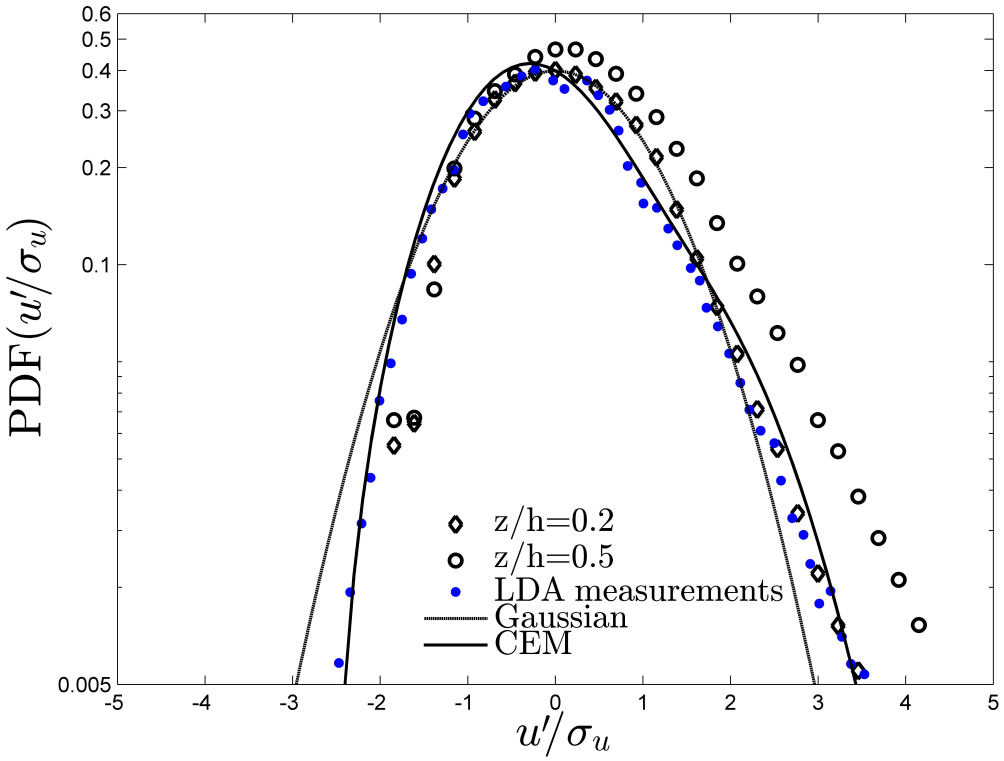

FIGURE 2.9: The pdf of the normalized advection velocity calculated from the lagged cross-correlations in Fig. 2.8 at $z/h = 0.2$ and $z/h = 0.5$. The reported pdf of LDA-measured velocity distribution in (Poggi et al., 2004c), a 3^{rd} order CEM (Cumulant expansion model) fit, and Gaussian distribution are also shown for comparisons.

3

Scaling and similarity of the anisotropic coherent eddies in near-surface atmospheric turbulence

3.1 Introduction

Besides their importance for predicting the exchange of matter and energy at the land-atmosphere interface, near-surface atmospheric flows offer a unique setting in the literature of wall-bounded turbulence due to the large separation between inertial/outer (e.g. $\delta \sim 1000$ m) and viscous ($\nu/u_* \sim 1$ mm) scales. It is no surprise that neutrally-stratified atmospheric surface-layer (ASL) flows are emblematic to high Reynolds number ($Re = u_*\delta/\nu$) experiments that are otherwise difficult to achieve in canonical turbulent boundary-layers (e.g. Metzger and Klewicki, 2001; Kunkel and Marusic, 2006; Marusic et al., 2010). Here[1], $u_* = \sqrt{\rho^{-1}\tau_s}$ is the friction velocity, δ is the atmospheric boundary-layer (ABL) height (pipe radius or channel half width in experimental fluids), $\tau_s \approx -\rho\,\overline{uw}$ is the shear stress at the surface, u and w are the turbulent fluctuations of the longitudinal (streamwise) and vertical (wall-normal) ve-

[1] Note that the terminology and nomenclature used by the atmospheric sciences community can be rather different from their experimental and theoretical fluid mechanics peers. Unless otherwise stated, meteorological notation and definitions are assumed here. Hutchins et al. (2012) provide a useful contrast on this issue that can extend substantially beyond a matter of notation.

locity components around their corresponding time-averaged values U and W, ν and ρ are the kinematic viscosity and density of the fluid, and over-line or capital letters denote Reynolds (or time) averaging. Nevertheless, at least from an observational perspective, mapping the scaling laws of velocity spectra and/or structure functions of wall turbulence to deep layers of ABL flows has encountered mixed and at times contradictory findings. The notion that, away from the viscous subrange, the distance from the wall $z \gg \nu/u_*$ and δ are the dominant similarity length scales for the intermediate (z-scaling) and outer regions is particularly challenged in near-surface atmospheric flows. This challenge will be the focus of the work here.

A relatively consistent and systematic theory of high Re wall-bounded turbulence seems to be currently endorsable, at least with regards to the mean flow and second-order turbulence statistics [recent reviews by Marusic et al. (2010) and Jiménez (2012)]. A central tenet of this theory is the existence of a self-similar inertial subrange (overlap or intermediate region) at distance z ($\nu/u_* \ll z \ll \delta$) normal to the wall/surface, in which the characteristic velocity and length scales are u_* and z (Townsend, 1961). Both experimental and theoretical studies have supported logarithmic scaling laws in this sublayer for the mean $U/u_* = \kappa^{-1} \ln(z) + C_s$ (Prandtl, 1925; von Kármán, 1930), variance $\sigma_u^2 = \overline{u^2} = A_1 - B_1 \ln(z/\delta)$ (Townsend, 1976; Marusic et al., 2013; Banerjee et al., 2015), and more recently all higher even-order moments $(\overline{u^{2p}})^{1/p} = A_p - B_p \ln(z/\delta)$ ($p \geqslant 1$) (Meneveau and Marusic, 2013; Katul et al., 2016) of the longitudinal velocity. The constant $B_1 \approx 1.25$ is thought to be universal (Stevens et al., 2014; de Silva et al., 2015), A_1 can depend on flow conditions, C_s is a wall/surface roughness constant, and $\kappa \approx 0.4$ is the von Kármán constant. Of particular interest here is the logarithmic scaling of σ_u^2 and the associated k^{-1} power law in the spectrum $E_{uu}(k)$ at low longitudinal wavenumbers k (typically in the range $1/\delta < k < 1/z$). The spectrum $E_{uu}(k)$ is defined such

that $\sigma_u^2 = \int_0^\infty E_{uu}(k)\,\mathrm{d}k$, and the wavenumber $k = 2\pi f/U$ corresponds to inverse longitudinal distance, usually inferred from frequency (f) (time) measurements of sonic or hot-wire anemometry using Taylor's frozen turbulence hypothesis (Taylor, 1938b). The two scaling laws follow from Townsend's model of attached eddies in the equilibrium/logarithmic region, where larger-than-inertial scale coherent eddies of size $z < s < \delta$ are attached to the wall/surface and sense its effects (Townsend, 1961, 1976). Integrating $E_{uu}(k) \propto k^{-1}$ in the range $1/\delta \leqslant k \leqslant 1/z$ (attached eddies) recovers the $\sigma_u^2 \sim \ln(z/\delta)$ scaling, and hence the two are equivalent (see also Banerjee and Katul, 2013). It is worth noting that the inner (ν/u_*), inertial (z), and outer (δ) length scales are used here as limits indicative of eddy sizes and transitions in spectral scaling laws, rather than exact cutoff length scales at which such transitions occur.

Perhaps the most popular explanation of the origin of the k^{-1} scaling in $E_{uu}(k)$ is the dimensional approach of Perry et al. (1986) based on Townsend's model of attached (active) eddies (Townsend, 1961, 1976), i.e. the existence of large separation between the scales of motion or equivalently a sufficiently high Re. This scaling emerges then as a transition/overlap range between the very large scale motion (VLSM)[2] [$E_{uu} \propto k^0$ for $k < 1/\delta$], and fine-scale isotropic eddies that follow Kolmogorov's theory (Kolmogorov, 1941, hereafter K41) [$E_{uu} \propto k^{-5/3}$ for $1/z \ll k \ll 1/\eta$; $\eta = (\nu^3/\epsilon)^{1/4}$ is the Kolmogorov microscale, and ϵ is the rate of viscous dissipation of turbulence kinetic energy (TKE) assumed equal to the mean rate of TKE transfer across scales]. Several other phenomenological (Nikora, 1999) and theoretical (Tchen, 1953; Katul et al., 2012) models also predicted or explained this k^{-1} scaling (Table 1 in each of Katul and Chu (1998) and Drobinski et al. (2007) provide a sur-

[2] VLSM is commonly referred to as inactive range/eddies because they do not contribute to stress and energy production. However, this range is part of energy transport and we simply use VLSM to represent it. Perry and Abell (1977) called these non-universal motion due to the lack of self-similarity.

vey of the literature). Physically, deep within the logarithmic layer, the preferential suppression of the vertical velocity fluctuations (w) distorts large scale coherent eddies of size $s > z$ in the streamwise direction, and turbulence becomes increasingly anisotropic as the wall/surface is approached (Davidson and Krogstad, 2014). These anisotropic/attached eddies are 'active' in the shear production ($P = -\overline{uw}\,\mathrm{d}U/\mathrm{d}z$) of TKE, where the interaction between the momentum flux ($-\overline{uw}$) and the mean flow vorticity ($\mathrm{d}U/\mathrm{d}z$) mostly occurs. Hence, very close to the wall/surface, the spectrum of the longitudinal velocity is expected to exhibit three distinct ranges at scales larger than η. In pre-multiplied form (i.e. $k\,E_{uu}(k)$), these are from small (high k) to large (low k) scales: (i) $k\,E_{uu}(k) \propto \epsilon^{2/3}\,k^{-2/3}$ for $1/z \ll k \ll 1/\eta$. These isotropic eddies are denoted as 'detached' here (no wall effects); (ii) $k\,E_{uu}(k) \propto k^{0}$ for $1/\delta < k < 1/z$ commensurate with the anisotropic production range. These are denoted as 'attached' eddies; and (iii) $k\,E_{uu}(k) \propto k^{+1}$ for $k < 1/\delta$ (VLSM), although this scaling of the very large scales is uncertain.

At the experimental front, several studies on ASL flows reported a low-wavenumber k^{-1} regime in $E_{uu}(k)$ (e.g. Katul and Chu, 1998; Högström et al., 2002; Drobinski et al., 2004). Both Högström et al. (2002) (their Fig. 5) and Drobinski et al. (2004) (their Figs. 6 and 7) show that the extent of the k^{-1} range decreases with increasing height above the surface, indicating that deep within the logarithmic layer, the emergence of the anisotropic (k^{-1}) range comes at the expense of a narrower isotropic ($k^{-5/3}$) extent (Davidson and Krogstad, 2014). Conversely, no k^{-1} scaling was detected in the Kansas (Kaimal et al., 1972) and some other ASL experiments (Busch and Panofsky, 1968). It is also noticeable that Drobinski et al. (2004) and Drobinski et al. (2007) observed an $E_{ww}(k) \propto k^{-1}$ scaling for the vertical velocity spectra around 30 m above the surface, but not in deeper layers of the near-neutral ASL. In turbulent boundary-layer and pipe experiments, these mixed findings have also received attention (e.g. Del Alamo et al., 2004; Vallikivi et al., 2015, and references

therein), mainly from a perspective of Re (scale separation) dependence.

The elusiveness of a clear k^{-1} scaling in $E_{uu}(k)$ has recently refocused the attention on its physical-space equivalent, the second-order structure function $D_{uu}(r) = \overline{[u(x+r) - u(x)]^2}$ (definition in section 3.2) (Davidson et al., 2006; Davidson and Krogstad, 2009, 2014; de Silva et al., 2015; Chung et al., 2015; Pan and Chamecki, 2016; Chamecki et al., 2017). Here, $r = \tau U$ is the longitudinal separation distance, and $\tau = 1/f$ is the time separation. The function $D_{uu}(r)$ is the Fourier transform pair of $E_{uu}(k)$, and hence the k^{-1} power law is equivalent to a $\ln(r)$ scaling in $D_{uu}(r)$ in the anisotropic range, while the $k^{-5/3}$ in the finer-scale locally isotropic range is equivalent to the $r^{2/3}$ law that appeared in K41. Davidson et al. (2006) argued that the one-dimensional spectrum $E_{uu}(k)$ may not be the ideal tool for investigating and detecting the k^{-1} scaling due to large scale (three-dimensional) contamination in the one-dimensional spectra, an effect called aliasing. Indeed, they were able to detect a logarithmic scaling in the structure function in both smooth- and rough-wall boundary layers in a wind tunnel experiment (Davidson and Krogstad, 2014). The structure function has also the advantage of boundedness at large scales ($r \sim \delta$ or the integral length scale of the flow), where it flattens at $2\sigma_u^2$ (section 3.2). Beyond the existence of this logarithmic scaling, the analysis and experiments by Davidson and Krogstad (2014) showed that normalizing r by the dissipation-based length scale $l_\epsilon = u_*^3/\epsilon$ collapses experimental data at different heights better than z, especially in the anisotropic range. They attributed this collapse to the imbalance between the local production (P) and dissipation (ϵ) of TKE, and proposed a $\ln(P/\epsilon)$ correction to the $\ln(r/z)$ scaling. The dimensional analysis and large eddy simulation (LES) experiments by Pan and Chamecki (2016), and later by Chamecki et al. (2017) also showed the superiority of l_ϵ over the z-scaling.

Although the k^{-1} or $\ln(r)$ scaling laws and the associated transition/similarity length scales are still a subject of debate in canonical turbulent boundary-layers, this

paper identifies two aspects frequently encountered in atmospheric contexts where such issues remain inconclusive. These are (i) the existence of vegetation canopies where the flow in the roughness sublayer (RSL; defined here to extend from the canopy top until two to five canopy heights (h)) deviates appreciably from its ASL counterpart, and (ii) nonlocal energy transport, i.e. imbalance between the local production and dissipation of TKE. While the two aspects may be related, where typically $P/\epsilon \neq 1$ in the RSL of canopy flows, this imbalance is also not uncommon in deep layers of the ASL (e.g. Högström et al., 2002). The work here uses several experiments to discuss the existence of this k^{-1} scaling in near-surface atmospheric flows, some of its phenomenological aspects, and the possible collapse of experimental data when plotted with inertial or some other similarity coordinates. The discussion also includes the scaling laws of the vertical velocity to characterize anisotropy. By using the notation 'near-surface' we intend to contrast deep layers of the neutral ASL above smooth/rough surfaces ($\approx$ 1-10 m above water bodies, short grass fields), denoted as the eddy surface layer (ESL) by Hunt and Carlotti (2001) and Drobinski et al. (2004), with flows in the immediate vicinity of tall roughness elements (directly above vegetation canopies) (Fig. 3.1).

Turbulent motion in the RSL above a dense canopy deviates from inertial layer turbulence, and is more analogous to mixing layers than to rough-wall boundary layers due to the strong shear at the canopy top (inflection point in the mean velocity U) (Raupach et al., 1996; Poggi et al., 2004b). This mixing-layer analogy introduces an additional characteristic shear length scale [$l_s = U\,(\mathrm{d}U/\mathrm{d}z)^{-1}$] dictated by Kelvin-Helmholtz (K-H) instabilities initiated at the canopy top (Fig. 3.1), besides the inertial length scale (z). For canopy flows, z is defined to be above the zero-plane displacement height d_0, where the latter is the height from the ground associated with the mean height of momentum absorption within the canopy. Hence, with the assumption that u_* sets the inner boundary condition for all scales of motion and is

indeed the characteristic velocity scale, the two aspects identified above reduce the discussion into an issue of length scales that challenge the classical z-scaling. Figure 3.1 shows the conceptual framework used here to distinguish RSL and ASL flows, where at some height $z \gg \nu/u_*$ above a smooth/rough-surface ASL, or above d_0 for canopies, eddies larger than z are attached to the surface (above the buffer layer) or to the displaced wall d_0. Detached eddies that are much smaller than z are isotropic and follow the $r^{2/3}$ law.

To this end, five datasets (section 3.3) are used here to address the points raised earlier, namely (i) the extent and height dependence of the $\ln(r)$ (or k^{-1}) scaling in the velocity structure functions (spectra), if any; (ii) some of its phenomenological aspects related to deviations from the characteristics of homogeneous and isotropic turbulence; and (iii) the collapse of experimental data at different heights using several dominant length scales. The experiments were conducted in the RSL of vegetation canopies (two experiments), deep within the ASL (two experiments), and one lower Re open channel experiment for comparison with atmospheric flows. The work is limited to neutrally-stratified flows, which are a common occurrence deep within the ABL above vegetation canopies or water bodies. As opposed to convective cases where the ABL is dominated by large-scale thermal plumes (Ghannam et al., 2017a; Salesky et al., 2017), near-neutral flows close to the land surface remain a challenge in Large Eddy Simulation studies due to the larger impact of the relatively smaller anisotropic eddies on subgrid-scale formulations.

3.2 Definitions and theoretical framework

The coordinate system is defined such that x, y, and z form the longitudinal (streamwise), lateral (spanwise), and vertical (wall-normal) directions, and the corresponding fluctuating velocity components are u, v, and w with Reynolds (time) averages U, V, and W. The flow is stationary $[\partial(.)/\partial t = 0]$, planar homogeneous

$[\partial(.)/\partial x = \partial(.)/\partial y = 0$ for averaged quantities], and x is aligned with the mean flow (U) with no mean subsidence such that $V = W = 0$. With these assumptions, the second-order structure function for a velocity component α ($\alpha = u$ or w here) at some height z is given by

$$\begin{aligned} D_{\alpha\alpha}(r) &= \overline{\Delta\alpha(r)\Delta\alpha(r)} \\ &= 2\sigma_\alpha^2 \left[1 - \rho_{\alpha\alpha}(r)\right], \end{aligned} \tag{3.1}$$

where $\Delta\alpha\left(r\right) = \alpha\left(\mathbf{x} + r\hat{\mathbf{e}}_x\right) - \alpha\left(\mathbf{x}\right)$, $\mathbf{x}$ is the position vector, $r = \tau U$ is the longitudinal spatial separation inferred from measured time separation (τ), and $\hat{\mathbf{e}}_x$ is the unit vector in the x direction. Since spatial statistics are inferred from time measurements here, stationarity implies homogeneity in the sense of K41, where all turbulence statistics, or otherwise distributions of velocity differences, are independent of the time/space origin and are only functions of r. Both this assumption or planar homogeneity require $\overline{[\alpha(x+r)]^2} = \overline{[\alpha(x)]^2} = \sigma_\alpha^2$, and $\rho_{\alpha\alpha}(r) = \overline{\alpha(x+r)\alpha(x)}/\sigma_\alpha^2$ is the correlation coefficient that is the Fourier pair of $E_{\alpha\alpha}(k)$. The second-order structure function is a monotonically increasing function, ranging from $D_{\alpha\alpha}(0) = 0$ at $r = 0$ [$\rho_{\alpha\alpha}(0) = 1$], to $D_{\alpha\alpha}(L_\alpha) = 2\sigma_\alpha^2$ at $r = L_\alpha$ [$\rho_{\alpha\alpha}(L_\alpha) = 0$], where L_α is the integral length scale of the velocity component α. $D_{\alpha\alpha}(r)$ is a measure of the cumulative contribution of eddies of size r or less to the energy (per unit mass) σ_α^2, and $r\,\mathrm{d}D_{\alpha\alpha}(r)/\mathrm{d}r$ is roughly the energy contained in eddies of size r (Townsend, 1976; Davidson and Krogstad, 2014). The interest here is in the scaling laws of $D_{\alpha\alpha}(r)$ at different heights z in the ASL and RSL, and the transition/similarity length scales associated with these laws. In light of the earlier discussion, the scaling laws (see Fig. 3.1) in the isotropic (detached eddies), active/production (attached eddies), and

VLSM ranges are, respectively

$$D_{uu}(r) = C\epsilon^{2/3} r^{2/3}, \qquad \eta \ll r \ll l \tag{3.2}$$

$$D_{uu}(r) = A + B \ln\left(\frac{r}{l}\right), \qquad l \ll r \ll \delta, \quad \text{and} \tag{3.3}$$

$$D_{uu}(r) = 2\sigma_u^2 = 2\left[A_1 - B_1 \ln\left(\frac{z}{\delta}\right)\right], \qquad r \sim L_u \leqslant \delta, \tag{3.4}$$

where $C \approx 2.2$ is the Kolmogorov constant, A and B are additional constants, and l is some characteristic length scale. Since the structure function is commonly plotted against $\ln(r)$, the constant B will be referred to as the slope in Eq. (3.3). The dimensional analysis by Davidson and Krogstad (2014), Pan and Chamecki (2016), and Chamecki et al. (2017) showed that $l = l_\epsilon$ in Eq. (3.3) is the correct similarity length scale for the anisotropic range. Eqs. (3.3) and (3.4) follow from each other at scales $r \sim L_u \sim \delta$ with $l \sim z$, and by matching the two scaling laws, one obtains $B = 2B_1 \approx 2.5$ (e.g. Chung et al., 2015; de Silva et al., 2015). The logarithmic scaling in $D_{uu}(r)$ also follows from the assumption that the kinetic energy of the space-filling attached eddies scales with the momentum flux, such that $r\,\mathrm{d}D_{uu}(r)/\mathrm{d}r \sim u_*^2$, from which Eq. (3.3) follows accordingly. Dividing Eq. (3.2) by u_*^2 yields

$$\frac{D_{uu}(r)}{u_*^2} = C\left(\frac{r}{l_\epsilon}\right)^{2/3}, \tag{3.5}$$

and by the universality of C, the dissipation length scale $l_\epsilon(z) = u_*^3/\epsilon(z)$ collapses the inertial subrange (isotropic detached eddies) of the normalized structure function at different heights in the constant flux region ($\mathrm{d}u_*/\mathrm{d}z \approx 0$). For a logarithmic $U(z)$, $P = -\overline{uw}\,\mathrm{d}U/\mathrm{d}z \approx u_*^3/\kappa z$, and a local balance between P and ϵ implies that $l_P \propto l_\epsilon \propto \kappa z$, where $l_P = u_*^3/P$ is the production length scale (Pan and Chamecki, 2016; Chamecki et al., 2017). The latter arguments are the basis for the classical z-scaling in the intermediate region of wall-bounded shear flows, and both are challenged here where turbulent flows in the RSL deviate from inertial-layer flows and

$P \neq \epsilon$. Nevertheless, if $\mathrm{d}U/\mathrm{d}z = u_*/\kappa z$ is a good approximation (more so for near-neutral ASL than RSL flows), then $l_P \approx \kappa z$, $l_\epsilon = (P/\epsilon)\,\kappa z$, and $l_s = (U/u_*)\kappa z$. Equation (3.3) can be written with $l = l_\epsilon$ or $l = l_s$ as

$$\begin{aligned} D_{uu}(r) &= A + B \ln\left(\frac{r}{l_\epsilon}\right) \\ &= A - B \ln\left(\frac{P}{\epsilon}\right) + B \ln\left(\frac{r}{\kappa z}\right), \end{aligned} \tag{3.6}$$

and,

$$\begin{aligned} D_{uu}(r) &= A + B \ln\left(\frac{r}{l_s}\right) \\ &= A + B \ln\left(\frac{u_*}{U}\right) + B \ln\left(\frac{r}{\kappa z}\right), \end{aligned} \tag{3.7}$$

respectively. In other words, besides the typical inertial scaling $\ln(r/\kappa z)$, l_ϵ accounts for the imbalance between P and ϵ with the term $\ln(P/\epsilon)$ [this correction appeared in Davidson and Krogstad (2009) and Davidson and Krogstad (2014)], while l_s accounts for the effects of drag (u_*/U) at the canopy top.

To connect these various length scales (κz, l_ϵ, l_P, l_s) to turbulent eddies and scaling laws of velocity structure functions, the phenomenology of the attached eddies (Eq. (3.3)) as a departure from the well-studied locally homogeneous and isotropic turbulence is also of interest here. The latter fine-scale eddies ($r \ll l$) belong to the stages of Richardson's cascade where energy is neither produced nor dissipated but simply transported from larger eddies ($r > l$) that extract energy from the mean flow down to the viscous scales ($r \sim \eta$). In this respect, the probability density functions $G[\Delta\alpha^+(r)]$ ($\alpha = u$ or w) of the velocity differences are examined in the locally isotropic ($r \ll l$) and anisotropic ($r > l$) ranges ('+' sign indicates velocity normalization by u_*). The skewness $Sk[\Delta\alpha^+(r)] = \overline{[\Delta\alpha^+]^3}/(\overline{[\Delta\alpha^+]^2})^{3/2}$ and excess flatness factors $F[\Delta\alpha^+(r)] = \overline{[\Delta\alpha^+]^4}/(\overline{[\Delta\alpha^+]^2})^2$ (excess $\equiv$ above the Gaussian value

of 3) of these distributions are functions of the longitudinal separation distance r, and hence are indicative of the transition between locally isotropic (non-Gaussian) and anisotropic (close to Gaussian) scales. Note that $Sk[\Delta u^+(r)]$ for the longitudinal velocity component is equivalent to the structure skewness $S(r)$ defined as (Obukhov, 1949; Monin and Yaglom, 1975)

$$S(r) = \frac{D_{uuu}(r)}{[D_{uu}(r)]^{3/2}}, \tag{3.8}$$

where $D_{uuu}(r) = \overline{[u(x+r) - u(x)]^3}$ is the third-order structure function. Obukhov (1949) hypothesized that $S(r)$ is constant in locally homogeneous and isotropic flows, and proposed this constant-skewness assumption as a closure to the Kármán-Howarth-Kolmogorov equation (von Kármán and Howarth, 1938; Kolmogorov, 1941)

$$D_{uuu}(r) - 6\nu \frac{\mathrm{d}D_{uu}(r)}{\mathrm{d}r} = -\frac{4}{5}\epsilon r, \tag{3.9}$$

that relates the second- and third-order structure functions in the universal (inertial and viscous) isotropic range. At scales $\eta \ll r \ll l$ within this range, the effects of viscosity [second term in Eq. (3.9)] are negligible and Kolmogorov's '4/5' law is recovered

$$D_{uuu}(r) = -\frac{4}{5}\epsilon r, \tag{3.10}$$

such that, using Eqs. (3.2), (3.8), and (3.10), the skewness $S(r)$ in the inertial/isotropic range is roughly constant (Katul et al., 1997b, 2015)

$$S(\eta \ll r \ll l) \approx -0.22, \tag{3.11}$$

subject to some experimental uncertainty and Re effects. Deviations from these relatively established results for the inertial subrange are used to examine the phenomenology of the anisotropic range. Experiments, data, and methods of estimating the TKE dissipation rate ϵ and the dominant length scales are now presented.

3.3 Data and methods

This section reviews the main features of the five experiments (published data sets) used in the analysis. Site characteristics and flow conditions are featured in Table 3.1, and length scale estimations are summarized here. The two canopy experiments have an order of magnitude difference in canopy height (h) and are intended to examine the effects of canopy morphology and distance-from-the-wall on the anisotropic range of the velocity structure functions. The work is limited to several heights above the canopy in the RSL. The ASL experiments were conducted above a lake and a short grass field within 10 m above the surfaces, whereas the open channel flow is used as a reference canonical turbulent boundary-layer. In RSL and ASL cases, the flow is near-neutral with atmospheric stability parameter $|z/L_o| < 0.05$, where L_o is the Obukhov length.

3.3.1 Experiments

- Amazonian canopy (**AMA**): the experiment was part of the GoAmazon (Observations and Modeling of the Green Ocean Amazon) project, and its details are documented in Fuentes et al. (2016), Freire et al. (2017), and Gerken et al. (2017). The data were collected during a field campaign at the Cuieiras Biological Reserve, located 60 km north-northwest of the city of Manaus, Amazonas, Brazil, between March 2014 and January 2015 at a 50 m tall tower surrounded by a dense primary forest. The average canopy height at the measurement site is $h \approx 35$ m, with leaf area index estimated to be between 5.7 and 7.3 m^2 m^{-2}. High-frequency time series of the three wind velocity components within and immediately above the canopy were continuously measured by 9 triaxial sonic anemometers (model CSAT3, Campbell Scientific Inc, Logan, UT) between March 2014 and January 2015. Measurement frequency is 20 Hz, and approximate measurement heights are

$z/h =$ 0.2, 0.39, 0.52, 0.63, 0.7, 0.9, 1, 1.15, and 1.38. Measurements within the canopy are used here only for estimating the displacement height (d_0), while the structure function analysis is restricted to heights $z/h =$ 1, 1.15, and 1.38 within the RSL. A total of 24 data runs/blocks (30-min. each) were analyzed (see Table 3.1).

- Maize canopy (**MAI**): this experiment was conducted in a large flat field planted with maize near Mahomet, Illinois, between June and July 2011 (Gleicher et al., 2014; Duman et al., 2016; Pan et al., 2016). The average canopy height is $h \approx 2.1$ m, and the leaf area index during the measurement period is ≈ 3.3 m^2 m^{-2}. The three wind velocity components were sampled using 5 triaxial sonic anemometers (model CSAT3, Campbell Scientific Inc, Logan, UT) at a 20 Hz frequency. The approximate measurement heights are $z/h =$ 0.33, 0.67, 1, 1.33, and 1.67, and similar to the **AMA** canopy, the analysis is restricted to $z/h \geqslant 1$. Pan and Chamecki (2016) used a 7.5-hr stationary turbulence time series ($u_* = 0.51$ m s^{-1}) from measurements at this site and noted that the use of Taylor's hypothesis was problematic. Here, this 7.5-hr data block is split into 15 runs (30-min. each) to minimize non-stationarity. These runs are used as replicate realizations (see Table 3.1).

- Lake Geneva (**LAKE**): the measurements were part of the Lake-Atmosphere Turbulent EXchange (LATEX) field campaign over Lake Geneva, Switzerland (Vercauteren et al., 2008; Bou-Zeid et al., 2008; Li et al., 2016), and were collected on a 10-m high tower, 100 m away from the shore of the lake. The campaign lasted from mid August until late October 2006. Four sonic anemometers (Campbell Scientific CSAT3) were deployed at heights 1.65, 2.30, 2.95, and 3.60 m above the water surface to sample the three-component wind field at 20 Hz. The four measurement heights are used here and a total of 63 runs (30-min. each) are analyzed

(Table 3.1).

- Advection horizontal array turbulence study (**AHATS**): the experiment took place near Kettleman City, California, during the period from 25 July to 16 August 2008 (UCAR/NCAR Earth Observing Laboratory, 1990; Salesky and Chamecki, 2012). The field site was surrounded by short grass stubble and was predominantly horizontally homogeneous and level. Data from the AHATS profile tower, consisting of six CSAT-3 sonic anemometers (Campbell Scientific Inc.) mounted at heights $z \approx 1.5$, 3.30, 4.2, 5.5, 7, and 8 m are used here. The sampling frequency was 60 Hz and a total of 15 runs (36.4 min. each) are analyzed (Table 3.1).

- Open channel (**OC**): the details of this experiment are documented in Katul and Chu (1998) and Katul et al. (2012). Briefly, the experiment was conducted at Cornell University in a 20-m long, 1.0-m wide, and 0.8-m deep open channel tilting flume with a smooth stainless steel bed. The channel slope was set at 0.0001 mm^{-1} resulting in $h_w = 10.3$ cm of water depth. The longitudinal and vertical velocity components were measured using a two-dimensional split film boundary layer probe (TSI 1287W model). The sampling frequency was 100 Hz and the measurement period lasted for 1.365 min. at measurement heights $z = 0.1$, 0.2, 0.3, 0.4, 0.6, and 1 cm. Only the highest measurement levels $z = 0.6$ and 1 cm corresponding to $z^+ \approx 55$ and 92 are used here, where $z^+ = zu_*/\nu$ and $u_* = 0.9$ cm s^{-1}. The mean velocity is $U \approx 0.2$ m s^{-1} and only one run is available.

The multiple runs for each experiment were selected on the basis that (i) the friction velocity u_* was relatively constant with height (to within 15%), and hence it is assumed that the analysis is within the constant flux region, and (ii) the corresponding turbulence intensity $I_u = \sigma_u/U$ is less than 0.25 across these runs, a common practice to minimize the effects of using Taylor's frozen turbulence hypothesis. By assuming that all wavenumbers (eddies) are convected with the same velocity U, the

longitudinal spatial separation $r = \tau U$ and wavenumber $k = 2\pi f/U$ are then inferred from the time separation τ (or f) and U. The corrections to the use of Taylor's hypothesis suggested by Wyngaard and Clifford (1977) and Hsieh and Katul (1997) in the inertial subrange are also implemented (discussed in the next sub-section).

In what follows, for presentation and brevity purposes, we show results only from one individual run at each site (with multiple heights each), and statistics across all runs are presented whenever applicable. The profiles of the mean flow statistics (normalized by appropriate powers of u_*) for this sample run are shown in Fig. 3.2. The height z is normalized by canopy height h in the upper panel of Fig. 3.2 for canopy experiments, and by z_h for the ASL and open channel experiments (lower panel), where z_h is the highest measurement location ($z_h = 3.6$ m for **LAKE**, 8 m for **AHATS**, and 1 cm for **OC**; Table 3.1). A distinctive feature of canopy flows is the strong shear at the canopy top, manifesting itself by a much smaller U/u_* (or equivalently higher turbulence intensity) in the RSL (Fig. 3.2a) compared to the ASL (Fig. 3.2e). All higher-order moments in the RSL (Fig. 3.2b, 3.2c, 3.2d) follow typical profiles of plant canopies (see a review by e.g. Finnigan, 2000b), and approach their ASL counterpart as z/h increases. The mixed third-order moments $\overline{wuu}$ and $\overline{wwu}$ in Fig. 3.2d and 3.2e, or more precisely their gradients, are responsible for nonlocal transport of TKE and velocity variances. These are significant deep within the RSL and the ASL, and decrease with increasing height z, indicating that $P/\epsilon \neq 1$ very close to the wall/surface.

3.3.2 Dissipation and length scale estimation

From Wyngaard and Clifford (1977) and Hsieh and Katul (1997), the structure functions inferred from Taylor's hypothesis are corrected in the inertial subrange for finite I_u, such that Eq. (3.2) becomes $D_{uu}(r) = C[F_u(I_u)]\epsilon^{2/3}r^{2/3}$, where $F_u(I_u) = 1 + (11/9)I_u^2$, and $I_u = \sigma_u/U$ is the turbulence intensity. A similar correction for

$D_{ww}(r)$ with $F_w(I_u) = 1 + (11/36)I_u^2$ is also used. Since $I_u < 0.25$ for all experiments, $F_u(I_u)$ across all sites and runs is less than 1.08 and hence the corrections are reasonably small, well within the uncertainty in the value of $C \approx 2.2$. The inertial subrange is identified from the compensated second-order structure function $r^{-2/3} D_{uu}(r)$, which exhibits a relatively flat/constant range equal to $C\epsilon^{2/3}$ [see Eq. (3.2)], typically for 0.3 m $< r <$ 2 m in the experiments here (depending on the measurement height and sampling frequency). After Chamecki and Dias (2004) and Chamecki et al. (2017), the TKE dissipation rate ϵ is then estimated by averaging over this range, which extended for less than half a decade deep within the ASL and RSL to one/two decades at higher z. Estimating ϵ from the vertical velocity structure function $D_{ww}(r)$ in a similar manner did not result in any significant differences. However, estimates from $D_{uuu}(r) = -(4/5)\epsilon r$ in the inertial subrange were unreliable due to the noisy nature of high-order moments computed from measurements. Chamecki et al. (2017), who also used the **AHATS** data, showed that ϵ estimates from $D_{uuu}(r)$ were approximately 40% smaller (on average) than the ones from $D_{uu}(r)$. In the rest of the paper, ϵ values determined from the inertial subrange of $D_{uu}(r)$ are used.

To estimate the displacement height d_0 for the **AMA** and **MAI** canopies, the momentum flux ($\overline{uw}$) within the canopy ($0 < z \leqslant h$) was fitted to a fourth-order polynomial in z, and the drag force $F_d(z) = \mathrm{d}\overline{uw}/\mathrm{d}z$ is determined (the estimate is not sensitive to third- or fifth-order polynomial fits). The height d_0 is then calculated from

$$d_0 = \frac{\int_0^h z\, F_d(z)\, \mathrm{d}z}{\int_0^h F_d(z)\, \mathrm{d}z}, \tag{3.12}$$

as the mean height associated with momentum absorption. The range for the **AMA**

canopy is $0.73h \leqslant d_0 \leqslant 0.79h$ ($h \approx 35$ m) across the 24 runs, and for the **MAI** canopy is $0.69h \leqslant d_0 \leqslant 0.74h$ ($h \approx 2.1$ m) across the 15 runs. This indicates that the distance from the displaced wall (d_0) for the **AMA** canopy is between ≈ 10 and 24 m at the three measurement heights (see Table 3.1), while the range is ≈ 0.6 to 2 m for the **MAI** canopy. Similarly, the mean velocity (U) profile was fitted to a second-order polynomial in $\ln(z)$ for all experiments, from which the production and shear (only for canopies) length scales are calculated as $l_P = u_*^3/P$ and $l_s = U/(\mathrm{d}U/\mathrm{d}z)$, where $P = -\overline{uw}\,\mathrm{d}U/\mathrm{d}z$ is used. For canopies, the mean velocity log-polynomial fits are limited to $z/h \geqslant 0.9$, where three data points are available in this range (see Table 3.1). The dissipation length scale $l_\epsilon = u_*^3/\epsilon$ is calculated using the ϵ estimates from $D_{uu}(r)$ as discussed earlier. These z-dependent length scales, normalized by the inertial length scale κz, are shown in Fig. 3.3 for the data run presented above (Fig. 3.2). The ratio $l_P/\kappa z$ (filled-triangle symbols) is indicative of deviations from a logarithmic mean velocity profile, and except for the **OC** (Fig. 3.3e), where the highest measurement height is $z^+ \approx 99$, this ratio is close to unity at all heights for the other experiments (Figs. 3.3a-d). In contrast, $l_\epsilon/\kappa z$, which is then approximately $l_\epsilon/l_P = P/\epsilon$, deviates appreciably from unity deep within the RSL (less so for the ASL), and approaches κz at higher heights, with the exception of the **LAKE** data where all measurement heights are within only 4 m from the surface. The shear length scale l_s follows l_ϵ closely in the RSL. This finding was also noted in the LES runs of Pan and Chamecki (2016) for the **MAI** canopy, although l_s estimated from the data here exceeded l_ϵ at the canopy top. These length scales are used in subsequent sections to explore the phenomenology and the collapse of the large anisotropic scales.

Before presenting the results, it is noted that when l_ϵ is estimated from the inertial subrange of the longitudinal velocity structure function, it is bound to collapse $D_{uu}(r)$ at small r. This collapse of data is not necessarily the case for larger scales in $D_{uu}(r)$

and/or $D_{ww}(r)$ that are of interest here.

3.4 Results and discussion

3.4.1 Scaling laws of velocity structure functions and spectra

Since the $\ln(r)$ and/or k^{-1} (k^0 in premultiplied form) scaling laws can be elusive when using experimental data, Fig. 3.4 shows both the normalized structure function D_{uu}/u_*^2 and premultiplied spectra kE_{uu}/u_*^2 at the highest measurement location from each experiment (height dependence is discussed later). These are plotted against $r/\kappa z$ and kz on a log-log scale and multiplied by an arbitrary constant (vertical shift) for clarity. The $r^{2/3}$ (Fig. 3.4a) and $k^{-2/3}$ (Fig. 3.4b) power laws expected in the isotropic range are shown as solid gray lines to depict the extent of this subrange and deviations therefrom. Note that these are not data fits and are only used here to indicate the commencement of the logarithmic (or k^{-1}) scaling laws. Nevertheless, the logarithmic fits in Fig. 3.4a (dashed gray lines) are not forced to start at these scales (i.e where D_{uu} deviates from the $r^{2/3}$ scaling), but rather fitted within a range at larger r and the resulting linear [in $\ln(r/\kappa z)$] fits are extended over a wider range. The slope B [Eq. (3.3)] of the fits to the anisotropic range in the measured structure function (Fig. 3.4a) compares well with the values ($B \approx 2.5$) estimated from matching arguments (e.g. de Silva et al., 2015), as introduced earlier in section 3.2. Both Fig. 3.4a and 3.4b show that this anisotropic range commences at scales larger than z (around $1.2z$ to $5z$ depending on the experiment), as opposed to the classical z-scaling that typically assumes $kz = 1$ (shown as vertical black line in Fig. 3.4b) sets such a transition (e.g. the experiments by Katul and Chu, 1998). These are inferred from the approximate start of this range, roughly $3 < r/\kappa z < 8$ (Fig. 3.4a) and $0.2 < kz < 0.3$ (Fig. 3.4b), with no significant differences between RSL and ASL experiments. However, canopy cases (**AMA** and **MAI**) show a shorter

k^0 range, extending for less than half a decade in both E_{uu} and D_{uu}. This is due to the fact that the integral length scale of the longitudinal velocity component L_u is much smaller in the RSL than in the ASL, typically within $h < L_u < 3h$ in the former and $L_u \sim \delta$ in the latter.

Conversely, similar analysis for the vertical velocity (D_{ww} and E_{ww}) at the same measurement height shows a much smaller scale separation (Fig. 3.5). Although the pre-multiplied spectra for the **AMA**, **LAKE**, and **AHATS** experiments exhibit a short (less than a decade) k^0 range, the slope of the logarithmic fits to the structure function D_{ww} (Fig. 3.5) is smaller ($B < 1$), indicating that D_{ww} attains $2\sigma_w^2$ rapidly with increasing scale. For these sites, $kz \approx 1$ seems to set the end of the $k^{-2/3}$ scaling, while this isotropic range extends to larger scales than z ($kz < 1$) in the **MAI** and **OC** experiments. Overall, after repeating such an exercise by examining $D_{\alpha\alpha}$ and $E_{\alpha\alpha}$ ($\alpha = u$ and w) for all data runs and all experimental sites, we note that using either approach (from an experimental view) to hunt for the $\ln(r)$ or k^{-1} scaling laws is elusive, and here we contrast both means in pursuit of that. In particular, the structure function is commonly plotted against $\ln(r)$, and hence fitting a linear trend [Eq. (3.3)] over a short range of scales to find the $\ln(r)$ law can be misleading. Theoretically, the separation of scales between the integral length scales L_α and the upper limit of the inertial subrange, be it $\approx z$ or some other limit/range l, is indicative of the cross-over between the $r^{2/3}$ and $2\sigma_\alpha^2$ regimes. This scale separation is height-dependent, and increases with increasing z (always deep within the RSL or ASL). Figure 3.6 depicts this argument, where both D_{uu} (red lines) and D_{ww} (blue lines) are plotted at all available measurement heights for each experiment, with the lowest height at the bottom. In canopy cases (Fig. 3.6a and 3.6b), deviations from the $r^{2/3}$ (gray lines) power law in both D_{uu} and D_{ww} have a short extent before reaching the integral length scales L_u and L_w (shown as short vertical lines). On the other hand, the ASL and channel experiments (Figs. 3.6c-3.6e) show an extensive

overlap region for D_{uu} but not D_{ww}. Both integral length scales exhibit a minor change with height deep within the RSL and ASL. These were calculated empirically from the correlation coefficient $\rho_{\alpha\alpha}(r)$ introduced in section 3.2.

In addition to the existence and height dependence of the logarithmic scaling in D_{uu}, the universality (or lack thereof) of the slope B in Eq. (3.3) is also of interest. This slope has dimensions of energy density, where $r\,\mathrm{d}D_{uu}(r)/\mathrm{d}r = B$ in the production range. The arguments set forth by Townsend's attached-eddy model predict a height dependence of TKE$= (1/2)(\sigma_u^2 + \sigma_v^2 + \sigma_w^2)$ by virtue of the $\ln(z/\delta)$ scaling in σ_u^2, while the classical view that the kinetic energy scales with u_*^2 (constant with height) implies otherwise. To track the consequence of this argument, we match the energy density in the inertial subrange, $r\,\mathrm{d}D_{uu}(r)/\mathrm{d}r = (2/3)C\epsilon^{2/3}r^{2/3}$ [see Eq. (3.2)], with its counterpart B in the production range at some limit $r \approx l$. For $l \approx z$, $B \propto \epsilon^{2/3}z^{2/3}$ and is therefore height dependent, while $l \approx l_\epsilon$ yields $B \propto \epsilon^{2/3}l_\epsilon^{2/3} \propto u_*^2$. Figure 3.7 shows a comparison between the slope B obtained from data fits (blue circles) and from these matching arguments, with $B \propto \epsilon^{2/3}z^{2/3}$ in black color and $B \propto u_*^2$ in red color. These are shown as function of the friction velocity u_* for all the runs available in each experiment, and at the highest height only for illustration. There is a clear tendency for B to increase with increasing momentum flux (u_*) in all experiments, indicating lack of universality, despite B being always of order unity as noted by Davidson and Krogstad (2014). Figure 3.7 depicts that the $\epsilon^{2/3}z^{2/3}$ argument captures the variability in B from the data fits across all u_* values better than the $B \propto u_*^2$ counterpart, in support of Townsend's arguments of energy dependence on z. This is particularly the case in the RSL of canopies (Fig. 3.7a and 3.7b), where $P/\epsilon \neq 1$ and hence the $\epsilon^{2/3}z^{2/3}$ dependence accounts for such an imbalance. To disentangle the origins of this scale separation and transitions between isotropic and anisotropic scales, some phenomenological aspects of the turbulence scales are discussed next.

3.4.2 Phenomenology of the anisotropic range

The age (or extent) of the anisotropic coherent structures that follow the logarithmic scaling explored earlier is the main theme of this section. As such, the probability density functions (*pdf*) of the velocity differences $\Delta u^+(r)$ and $\Delta w^+(r)$ are shown in Fig. 3.8 at two separation scales, $r \ll l_\epsilon$ indicative of the detached isotropic eddies, and $r \gg l_\epsilon$ to sample anisotropic eddies. These are for the highest measurement location at each site as earlier. Both $\Delta u^+(r)$ and $\Delta w^+(r)$ have a zero mean and the separation scales are chosen for illustration, where the length scale l_ϵ is used since it is typically larger than z ($P/\epsilon > 1$), hence $r \gg l_\epsilon$ is in the production range. At small scales, the *pdfs* $G[\Delta u^+(r \ll l_\epsilon)]$ and $G[\Delta w^+(r \ll l_\epsilon)]$ (Fig. 3.8a and 3.8c) exhibit heavier tails than at larger scales (Fig. 3.8b and 3.8d) for all sites. The tails of small-scale turbulence are known to decay much slower than Gaussian (Anselmet et al., 1984; Sreenivasan and Antonia, 1997), and approach a Gaussian distribution at larger scales. While the excursions/tails of Δu^+ and Δw^+ appear smaller for canopies at $r \ll l_\epsilon$ (Fig. 3.8a and 3.8c), these are simply due to a higher u_*, i.e. canopy flows in fact experience larger excursions in velocity differences at small scales, especially in the longitudinal velocity component u. The importance of these individual *pdfs* here is that they encode the statistical moments of turbulence in $\Delta u^+(r)$ and $\Delta w^+(r)$. For instance, the second-moment (variance) of each of these distributions is the value of the structure functions D_{uu} and D_{ww} at the scale r, which was explored earlier in Figs. 3.4 and 3.5, such that the variances $\overline{[\Delta u^+(r)]^2}$ and $\overline{[\Delta w^+(r)]^2}$ at some large r are the cumulative contribution from all the corresponding distributions at smaller separation distances. To examine how fast the *pdfs* approach a Gaussian distribution, the skewness $Sk[\Delta\alpha^+(r)]$ and excess flatness factors $F[\Delta\alpha^+(r)]$ ($\alpha = u$ and w) of these distributions are plotted against $r/\kappa z$ in Fig. 3.9. Both Sk and F have a decreasing trend with increasing scale r, indicating that the *pdf* of velocity differences

approaches a Gaussian-like distribution at large r. Also, these moments generally decay slower (with r) for the longitudinal $[\Delta u^+(r)]$ than the vertical $[\Delta w^+(r)]$ velocity differences, due to the larger scale separation in u compared to w. It is interesting to note that the flatness factors F for both velocity components collapse with κz in all experiments, and approach zero (equivalent to the Gaussian value 3) around $10\kappa z$. The **AMA** and **AHATS** experiments have the largest scale separation between l_ϵ (vertical lines in Fig. 3.9) or κz and the scale r at which the moments approach their Gaussian counterpart. These experiments have the largest distance from the wall ($z = 24$ m above d_0 for **AMA** and $z = 8$ m for **AHATS**; Table 3.1) compared to the other experiments, and note that both exhibited a k^{-1} scaling in E_{ww} (Fig. 3.5). In such contexts, no significant differences on scale separation between the RSL and ASL seem noticeable, but rather the distance from the wall emerges as a more important factor.

Besides the individual *pdfs* that characterize the scale-wise contribution to the diagonal elements (σ_u^2 and σ_w^2) of the stress tensor through D_{uu} and D_{ww}, another important attribute is the stress/energy production by the scales of motion. The anisotropic coherent eddies are known to be the scales where turbulence (momentum flux $-\overline{uw} = u_*^2$) interacts with the mean flow ($\mathrm{d}U/\mathrm{d}z$) to produce energy/variances. As such, the mixed second-order structure function $D_{uw}/u_*^2 = \overline{\Delta u^+(x+r)\Delta w^+(x)}$ that involves lagged (in r) cross-correlations between the velocity components is now explored. Upon expansion, this normalized structure function can be written as

$$\begin{aligned}\frac{D_{uw}(r)}{u_*^2} &= 2 - \frac{\overline{u(x)w(x+r)}}{u_*^2} - \frac{\overline{u(x+r)w(x)}}{u_*^2} \\ &\approx 2 - 2\frac{\overline{u(x)w(x+r)}}{u_*^2},\end{aligned} \tag{3.13}$$

where it is assumed that $\overline{u(x+r)\,w(x+r)} = \overline{u(x)\,w(x)}$ by planar homogeneity, and

the first term on the right hand side is $2\overline{u(x)\,w(x)}/u_*^2 = 2$. Also, after examination of the data from all experiments and at all available heights, the assumption $\overline{u(x)w(x+r)} \approx \overline{u(x+r)w(x)}$ appears reasonable here (data not shown). Hence, at very small scales (e.g. $r \ll l_\epsilon$ or z; isotropic range), the velocity components u and w are well correlated and $\overline{u(x)w(x+r)} \approx u_*^2$, indicating no contribution to the momentum flux $\overline{u(x)\,w(x)}$ from these small eddies. As r increases and the velocity components decorrelate, i.e. the second term in Eq. (3.13) decreases to zero, the larger-scale eddies cumulatively contribute to the momentum flux. This argument is investigated here by sampling the isotropic and anisotropic eddies in an analogous manner to the usual quadrant analysis of (u,w) fluctuations, typically used for characterizing ejection-sweep events. Fig. 3.10 shows such a scale-wise analysis for $\Delta u^+(r)$ and $\Delta w^+(r)$. The scatter plots of these quantities against each other in the isotropic ($r \ll l_\epsilon$; Fig. 3.10b) and anisotropic ($r \gg l_\epsilon$; Fig. 3.10c) scales suggest that at small separation distances r, the contributions from the four quadrants in Fig. 3.10b to the product $\overline{\Delta u^+ \Delta w^+}$ cancel each other, while at $r \gg l_\epsilon$, the second ($\Delta u^+ < 0$, $\Delta w^+ > 0$) and fourth ($\Delta u^+ > 0$, $\Delta w^+ < 0$) quadrants dominate the contribution to the negative momentum flux. This picture is consistent across all experiments. Figure 3.10a shows the joint *pdfs* of (Δu^+, Δw^+) for the scatter plots in Figs. 3.10b and 3.10c, with the filled/colored contours representing the isotropic scales in Fig. 3.10b, and the gray line contours corresponding with the energy-producing eddies in Fig. 3.10c. The analysis in Fig. 3.10c (or gray contours in Fig. 3.10a) shows that within the large-scale coherent eddies, it is the simultaneous occurrence of strong excursions/gradients in Δu^+, be these positive or negative, accompanied with strong excursions in Δw^+ of the opposite sign, that lead to shear production. By examining the second ($\Delta u^+ < 0$, $\Delta w^+ > 0$) and fourth ($\Delta u^+ > 0$, $\Delta w^+ < 0$) quadrants in Fig. 3.10c, it appears that the two mechanisms, namely large negative Δu^+ excursions accompanied by large positive Δw^+ ones (second quadrant; analogous to

ejection events), or the opposite (fourth quadrant; analogous to sweeping events), are equally likely to produce momentum. As opposed to the usual quadrant analysis of the ejection-sweep cycle that does not account for scale-wise contributions, the analysis here samples all eddy sizes and reflects on their role in shear/energy production. For instance, the lagged cross-correlation $-\overline{u(x)w(x+r)}/u_*^2$ (second term in Eq. (3.13)) is shown in Fig. 3.11 for all experiments and at all heights. The **OC** experiment behaves similar to ASL experiments and is no longer included in the analysis here for brevity. At small scales ($\approx r < \kappa z$ in Fig. 3.11), the velocity components $u(x)$ and $w(x+r)$ are well correlated and $\overline{u(x)w(x+r)} \approx \overline{u(x)w(x)} = u_*^2$, while as r increases, larger eddies accumulate momentum until $r \sim L_u$ (shown as vertical dashed lines in Fig. 3.11). Within the anisotropic range, it is evident that shear production is stronger at the larger-scale coherent motion and decreases as eddies cascade to smaller scales until isotropy is attained and no more shear is produced. It is worth noting that these shear-producing eddies extend to a wider range ($\approx$ two decades) in the ASL (Figs. 3.11c and 3.11d) than in the RSL ($\approx$ one decade) (Figs. 3.11a and 3.11b), where L_u is smaller in the latter.

The last two components of the phenomenology of the anisotropic range relate the structure function $D_{uu}(r)$ to its third-order counterpart $D_{uuu}(r)$ through the structure skewness $S(r)$ [Eq. (3.8)], and to the vertical velocity structure function $D_{ww}(r)$. Both are well-studied in the isotropic range where $S(r) \approx -0.22$ and $D_{uu}/D_{ww} \approx 3/4$ (ratio of the Kolmogorov constants for D_{uu} and D_{ww} in the universal isotropic range). Figure 3.12 shows the negative of the skewness $S(r)$ plotted against $r/\kappa z$ for all the experiments here. The length scales l_ϵ, l_s, and L_u for the highest measurement location are also shown. The value $S(r) \approx -0.22$ seems a satisfactory approximation at small scales, particularly for the ASL experiments (Figs. 3.12c and 3.12d), while it slightly lower in the RSL (Figs. 3.12a and 3.12b). Deviations from this value occur at or before $r \approx \kappa z$, and decay faster in the RSL than in the ASL. There is no strong

height dependence in $S(r)$, although it is noticeable that the inertial length scale κz collapses $S(r)$ at different heights in the ASL but not in the RSL. The negative values of $S(r)$ in both the isotropic (≈ -0.22) and anisotropic ranges indicate that $D_{uuu}(r) = \overline{[u(x+r) - u(x)]^3} < 0$, and hence at these scales, both negative and positive excursions in the longitudinal velocity fluctuations tend to decrease. Similar analysis for D_{uu}/D_{ww} (Fig. 3.13) shows that this ratio is close to the expected '3/4' constant in the isotropic range, and departs fast from this constant around $r \approx \kappa z$. At those larger scales, if D_{uu} exhibits a logarithmic scaling while D_{ww} attains $2\sigma_w^2$, the ratio D_{uu}/D_{ww} should also show a logarithmic scaling in r. This seems to be the case for all experiments except for **AMA**, which exhibits a logarithmic scaling in D_{ww}. The ratio D_{uu}/D_{ww} approaches the constant $(\sigma_u/\sigma_w)^2$ (calculated from the data and plotted as dashed horizontal lines in Fig. 3.13) at the very large scales, indicating a reasonable convergence of the scale-wise fluctuations to bulk turbulence statistics.

3.4.3 Similarity length scales

Figure 3.14 addresses the collapse of D_{uu}/u_*^2 at different heights for each experiment. In Figs. 3.14a and 3.14b, D_{uu}/u_*^2 at different heights within the RSL (Fig. 3.14a) and the ASL (Fig. 3.14b) are plotted against $r/\kappa z$ to assess whether the inertial length scale κz can collapse the experimental data. This is clearly the case for the ASL experiments in Fig. 3.14b (six heights for **AHATS** and four heights for **LAKE**), where all structure functions fall into one curve at all scales r, while in the RSL shown in Fig. 3.14a (three heights for each of **AMA** and **MAI**), there is clear discrepancy at different heights. In contrast, the length scale l_ϵ performs much better in collapsing the height-dependent D_{uu}/u_*^2 in the RSL (compare Fig. 3.14a and 3.14c), albeit there are small departures at large r. In the ASL, l_ϵ performs equally well to κz (compare Fig. 3.14b and 3.14d), where the structure functions at all heights again collapse into

a single curve. The large imbalance between P and ϵ in the RSL (see the inset in Fig. 3.14a) explains why l_ϵ may be the correct similarity length scale in such contexts, while a smaller imbalance in the ASL (inset in Fig. 3.14b) maintains κz (or l_ϵ) as the similarity length scale. A similar and perhaps stronger conclusion can be made for the vertical velocity structure function D_{ww}/u_*^2 (shown in Fig. 3.15), where by comparing Figs. 3.15a and 3.15c for the RSL, a remarkable collapse of the data can be seen when normalizing r by l_ϵ, while in the ASL (Figs. 3.15b and 3.15d), both κz and l_ϵ are comparable in bringing D_{ww} at different heights to a single curve. To this end, Fig. 3.16 compares the performance of l_ϵ with l_s in collapsing D_{uu}/u_*^2 for the canopy experiments only. While l_ϵ performed better than κz in the RSL (see Fig. 3.14), there were still some discrepancies at the large scales. In Fig. 3.16b, the shear length scale l_s commensurate with the Kelvin-Helmoholtz instabilities can remove such discrepancies.

3.5 Conclusions

This paper examined the scaling laws, phenomenology, and similarity of the large-scale coherent eddies in the roughness sub-layer (RSL) of dense canopies and in the atmospheric surface layer (ASL). The focus was on the flow field in near-neutral conditions, which is a logical first step before exploring the role of thermal stratification and scaling laws for scalar transport. The sparse canopy case where l_s may not be the prevalent vorticity thickness was not considered given the expected role of dispersive stresses in the roughness sublayer. The scaling laws of D_{uu} and D_{ww} inside canopies is retained for a future study given the additional length scales (such as von Karman streets and wake effects) involved and the need to by-pass the use of Taylor's frozen turbulence hypothesis in such conditions.

The large anisotropic scales of motion are known to exhibit a k^{-1} power law in the spectrum of the longitudinal velocity $E_{uu}(k)$ at low wavenumbers k, typically at

$kz < 1$, where z is the distance from the wall, or otherwise a logarithmic scaling in the corresponding structure function $D_{uu}(r) \sim \ln(r)$ at large separation distances $r > z$. It was shown in prior studies that the cross-over from the aforementioned large scales to inertial subrange scales is rather narrow and reasonably delineated by z. This z-scaling is examined here in the RSL and ASL when production and dissipation of turbulence kinetic energy are not in local balance, leading to additional length scales such as the dissipation ($l_\epsilon = u_*^3/\epsilon$) and mixing/shear ($l_s = U(\mathrm{d}U/\mathrm{d}z)^{-1}$) length scales. Five experiments (four atmospheric flows and one open channel experiment), with multiple heights and multiple realizations/runs each, are used here to explore these aspects. The findings indicate that both the k^{-1} in E_{uu} and/or $\ln(r)$ in D_{uu} exist within the RSL, ASL, and canonical turbulent boundary layers, although the extent of this anisotropic range varies across experiments, with the RSL exhibiting shorter extent due to the small separation of scales (the integral length scale is smaller than its ASL counterpart). Conversely, these scaling laws are absent in E_{ww} or D_{ww} for the vertical velocity components, except at large distances from the wall where a short extent of anisotropy emerges. Phenomenological aspects of the coherent eddies reveal that the statistics of velocity increments Δu and Δw approach a Gaussian-like behavior at large r. These findings are in broad agreement with the accepted picture of canonical turbulent boundary layers. Eddies associated with these large anisotropic r are further responsible for momentum/energy production corroborated by large positive (negative) excursions in Δu accompanied by negative (positive) ones in Δw. In terms of similarity, normalizing the separation distance r by the inertial length scale κz or l_ϵ shows comparable performance in collapsing the structure functions D_{uu} and D_{ww} at different heights in the ASL, where the ratio P/ϵ does not deviate appreciably from unity. In contrast, l_ϵ collapses these structure functions in the RSL better than z, albeit with some discrepancies at the larger scales. These discrepancies are mediated when the shear length scale l_s is used.

While the work here supports the use of l_ϵ for RSL and ASL flows in normalizing D_{uu} and D_{ww} at large scales instead of z, it appears to be insufficient and may be complemented by l_s for the RSL.

Table 3.1: Site and experimental characteristics. Note that the columns correspond to z: approximate measurement height (m), h: average canopy height (m), f: sampling frequency (Hz), time: run/block time length (min), Runs: number of blocks analyzed, and the ranges of u_* and U across the runs. Key: **AMA** ≡ Amazonian canopy; **MAI** ≡ maize canopy; **LAKE** ≡ Lake Geneva; **AHATS** ≡ Advection horizontal array turbulence study; and **OC** ≡ open channel experiments. See section 3.3 for further details.

Experiment	z (m)	h (m)	f (Hz)	time (min)	Runs -	${u_*}^1$ (m s^{-1})	U^1 (m s^{-1})
AMA	35, 40.25, 48.3	35	20	30	24	0.2-0.7	1-2.6
MAI	2.1, 2.8, 3.5	2.1	20	30	15	0.43-0.51	1.56-1.95
LAKE	1.7, 2.3, 3, 3.6	-	20	30	63	0.12-0.57	1.2-10.6
AHATS	1.5, 3.3, 4.2, 5.5, 7, 8	-	60	36.4	15	0.2-0.4	2.42-5
OC	0.006, 0.01	-	100	1.365	1	0.009	0.2

[1] Range of values of u_* and U across all the runs calculated from the lowest measurement height ($z/h \approx 1$ for canopies).

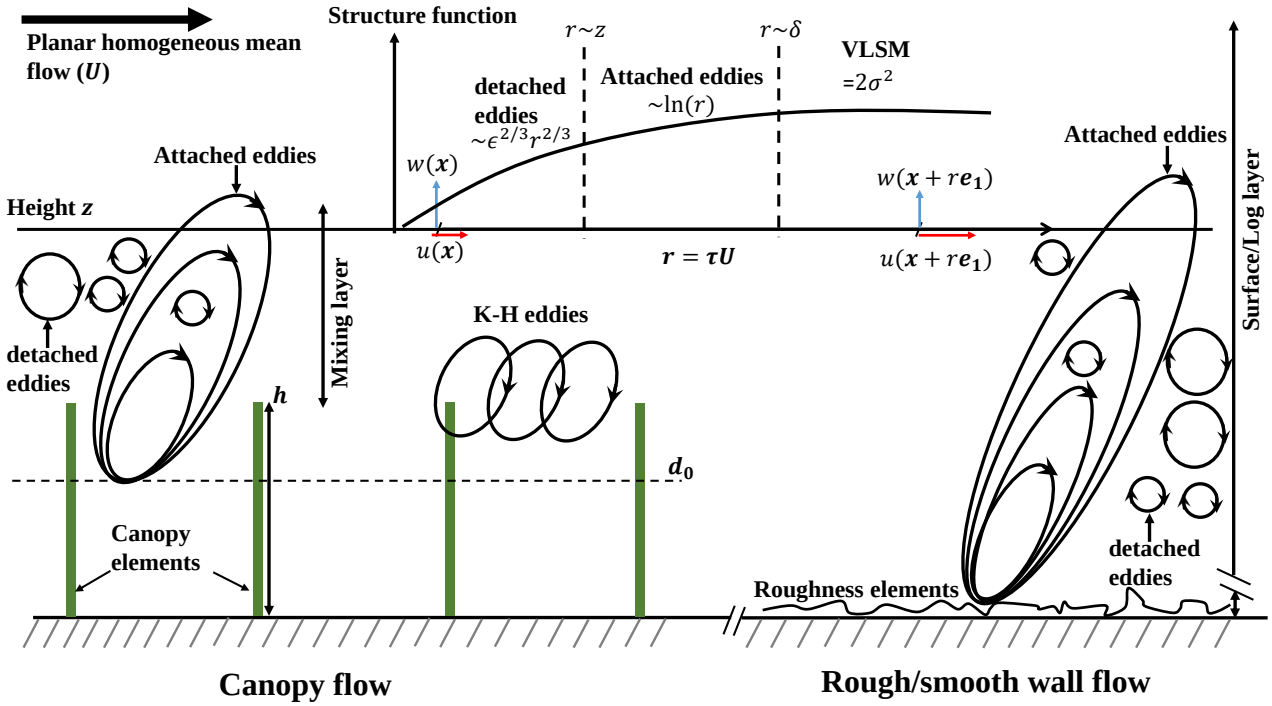

FIGURE 3.1: Conceptual framework used to distinguish some features of canopy (roughness sublayer; left) and wall-bounded (e.g. surface layer; right) flows. The flow in both cases is planar homogeneous with mean longitudinal velocity U. At some height z above the canopy (left) or surface (right), eddies of size larger than z are considered attached to a displaced wall (d_0) or surface, while typically much smaller eddies are detached (isotropic here) and follow K41 theory. For canopy flows, the analysis is restricted to the mixing layer where Kelvin-Helmholtz (K-H) eddies are active. The velocity (u and w) structure functions are interpreted as functions of the longitudinal separation distance $r = \tau U$, where τ is time separation. Dimensions are not-to-scale and h denotes canopy height. The height z and the direction and magnitude of the velocity components (red and blue arrows) are chosen arbitrarily for illustration.

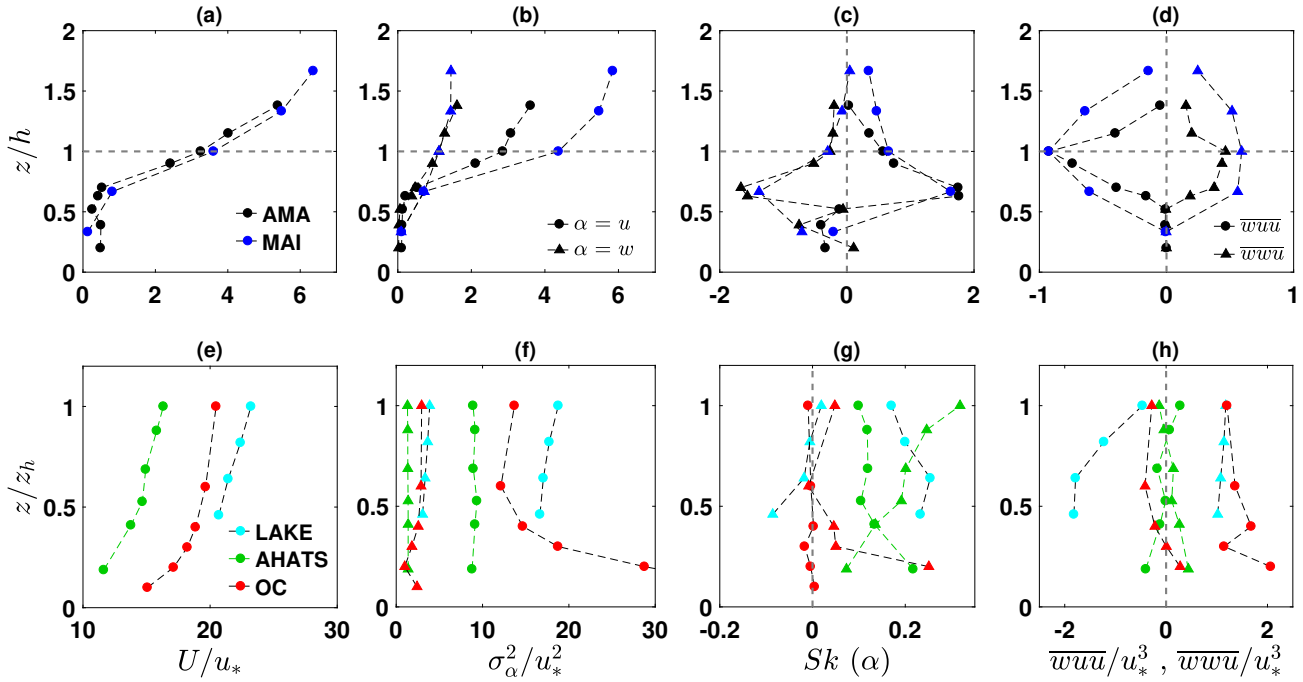

FIGURE 3.2: Dimensionless profiles of mean flow statistics for a select experimental run at each site/experiment (see Table 3.1) for (a)-(e): mean longitudinal velocity component; (b)-(f): velocity variances; (c)-(g): velocity skewness; and (d)-(h): mixed third-order velocity moments. The normalizing scales are the friction velocity (u_*), canopy height (h), and highest measurement location (z_h). Top panel [(a),(b),(c),(d)]: Amazonian (**AMA**; black; $h = 35$ m) and maize (**MAI**; blue; $h = 2.1$ m) canopy experiments. Bottom panel [(e),(f),(g),(h)]: smooth/rough wall experiments for open channel (**OC**; red; $z_h = 1$ cm), AHATS experiment (**AHATS**; green; $z_h = 8$ m), and Lake Geneva (**LAKE**; cyan; $z_h = 3.6$ m). The velocity components u and w are represented by the circle and triangle symbols respectively. Note that full profiles are shown for canopy experiments but subsequent analysis is restricted to flow above the canopy ($z/h \geqslant 1$).

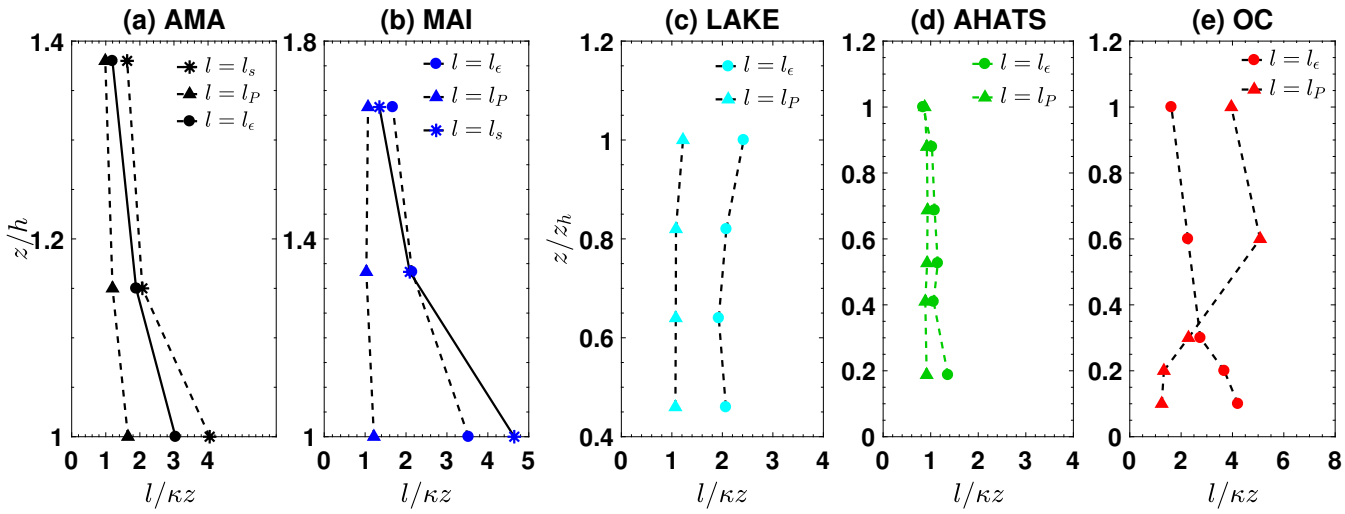

FIGURE 3.3: Profiles of the ratio $(l/\kappa z)$ of several length scales (l) to the inertial length scale (κz) against (a)-(b): z/h and (c)-(d)-(e): z/z_h for the experimental run in Fig. 3.2. For canopies [(a),(b)], κz is to be interpreted as the height above the zero-plane displacement.

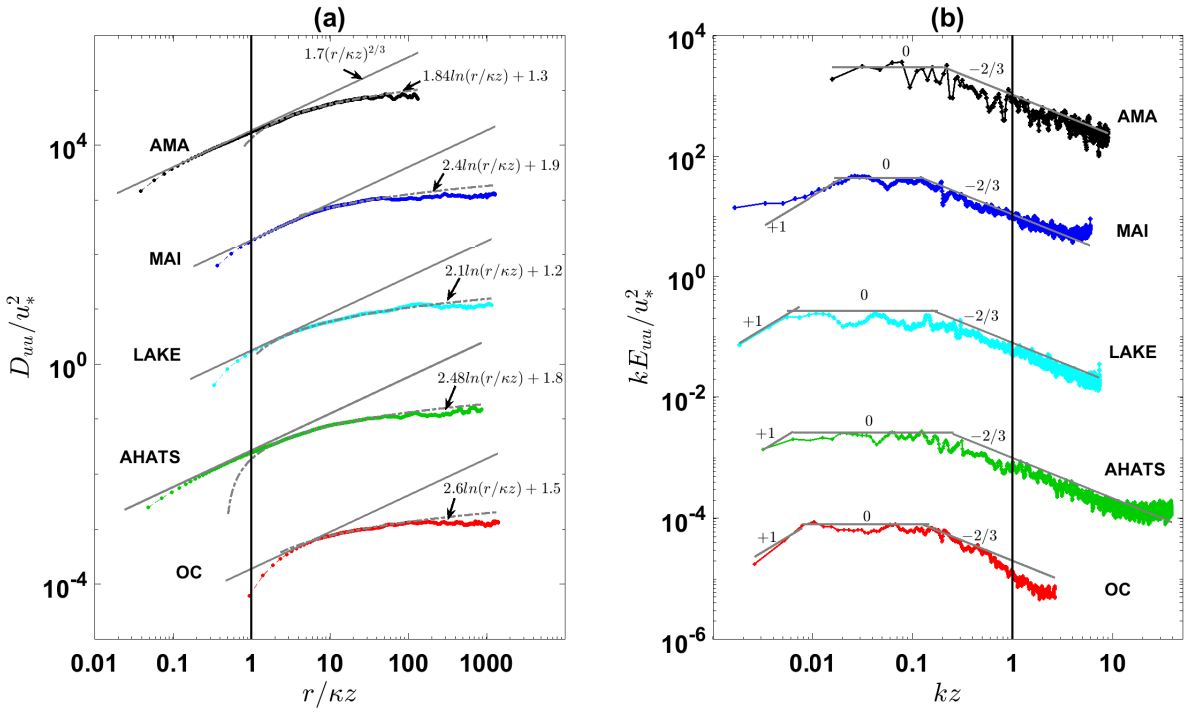

FIGURE 3.4: (a): Normalized structure function (D_{uu}/u_*^2) of the longitudinal velocity component against $r/\kappa z$ at each site/experiment (for highest measurement height only; see Table 3.1). Here, r is the longitudinal separation distance inferred from Taylor's frozen turbulence hypothesis and z is the distance from the surface/wall (or zero-plane displacement for canopies). The solid and dashed gray lines denote the $r^{2/3}$ (inertial range) and logarithmic law/fits (production range) respectively. (b): The corresponding normalized and pre-multiplied spectra (kE_{uu}/u_*^2) of the longitudinal velocity component plotted against kz, where $k = 2\pi/r = 2\pi f/U$ is the longitudinal wavenumber, f is the frequency and U is the mean longitudinal velocity. The solid gray lines denote the k^{+1} (nonuniversal/VLSM range), k^0 (production range), and $k^{-2/3}$ (inertial range) power laws respectively. All plots are shifted vertically for clarity.

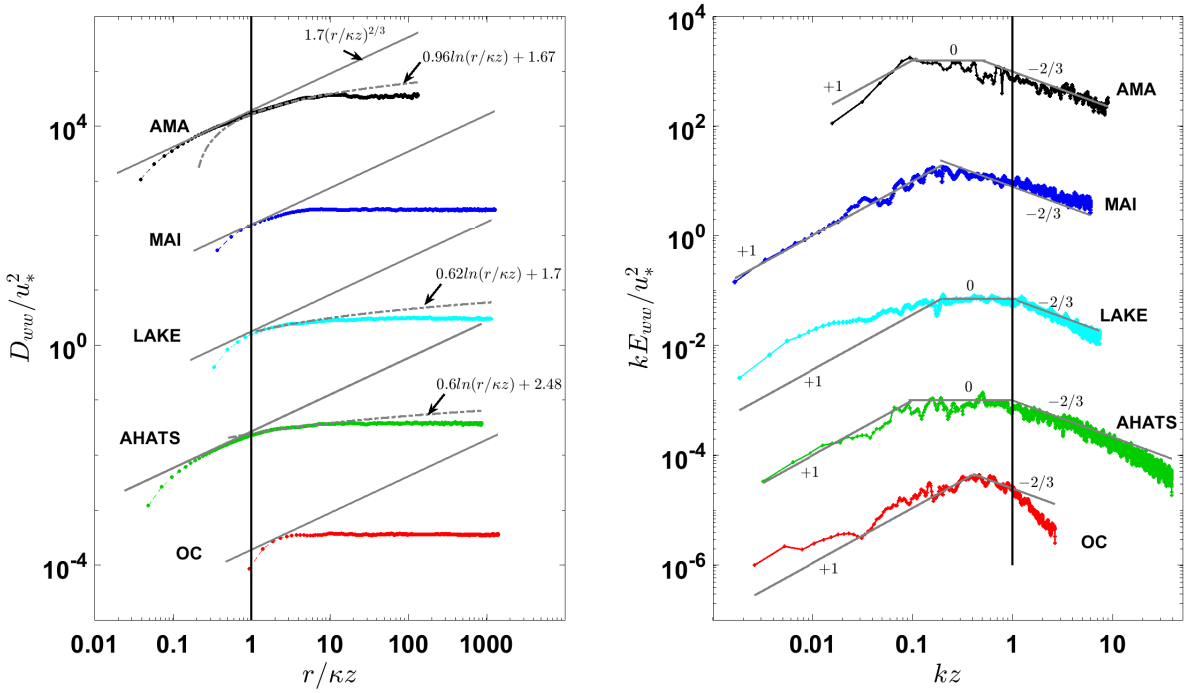

FIGURE 3.5: Same as Fig. 3.4 for the vertical velocity component.

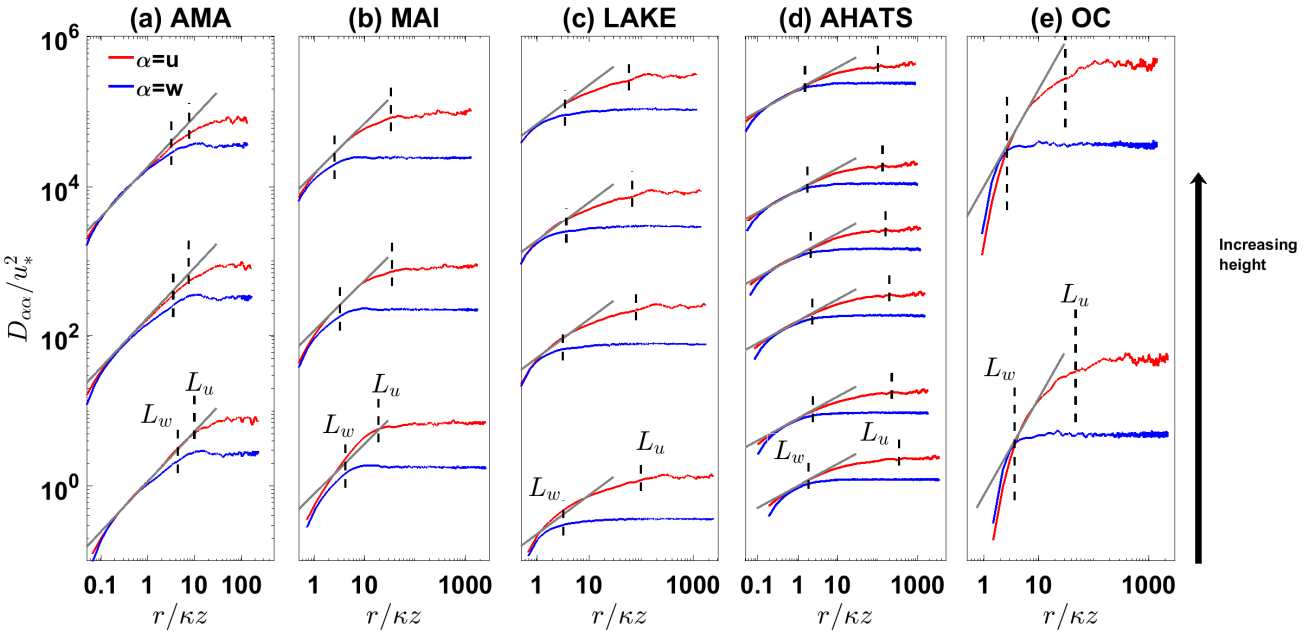

FIGURE 3.6: Normalized structure functions ($D_{\alpha\alpha}/u_*^2$) with $\alpha = u$ (red) and $\alpha = w$ (blue) plotted against $r/\kappa z$ at all measurement heights for (a): **AMA** canopy (three heights), (b): **MAI** canopy (three heights), (c): **LAKE** (four heights), (d): **AHATS** (six heights), and (e): **OC** (two heights). The separation distances $r = L_u$ and $r = L_w$ are shown at each height with a vertical dashed black line. The solid gray lines denote the $r^{2/3}$ (inertial range) power law. All plots are shifted vertically with the lowest measurement height at the bottom.

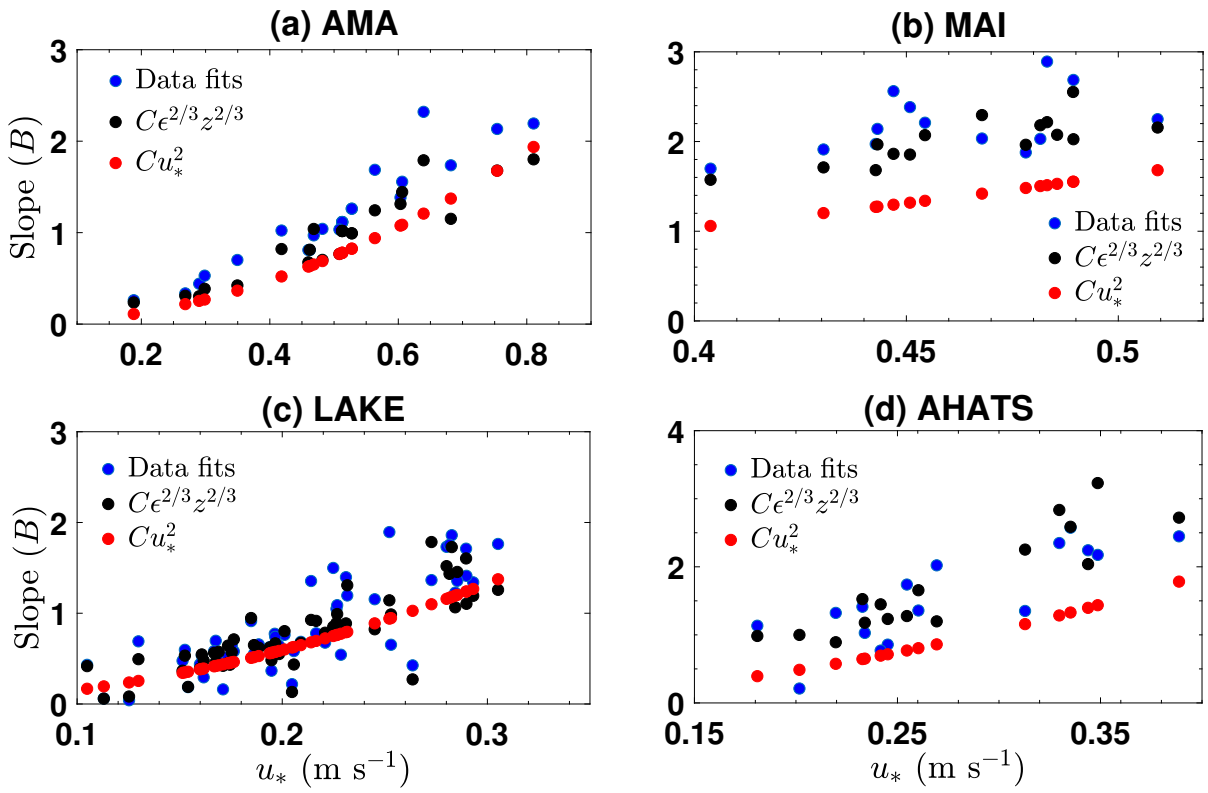

FIGURE 3.7: Slope (B) in the logarithmic scaling of the production range in D_{uu} plotted against u_* at each site. Data fits are indicated by blue color and energy density matching, $B \propto z^{2/3}$ and $B \propto u_*^2$ discussed in section 3.4 are shown in black and red colors respectively.

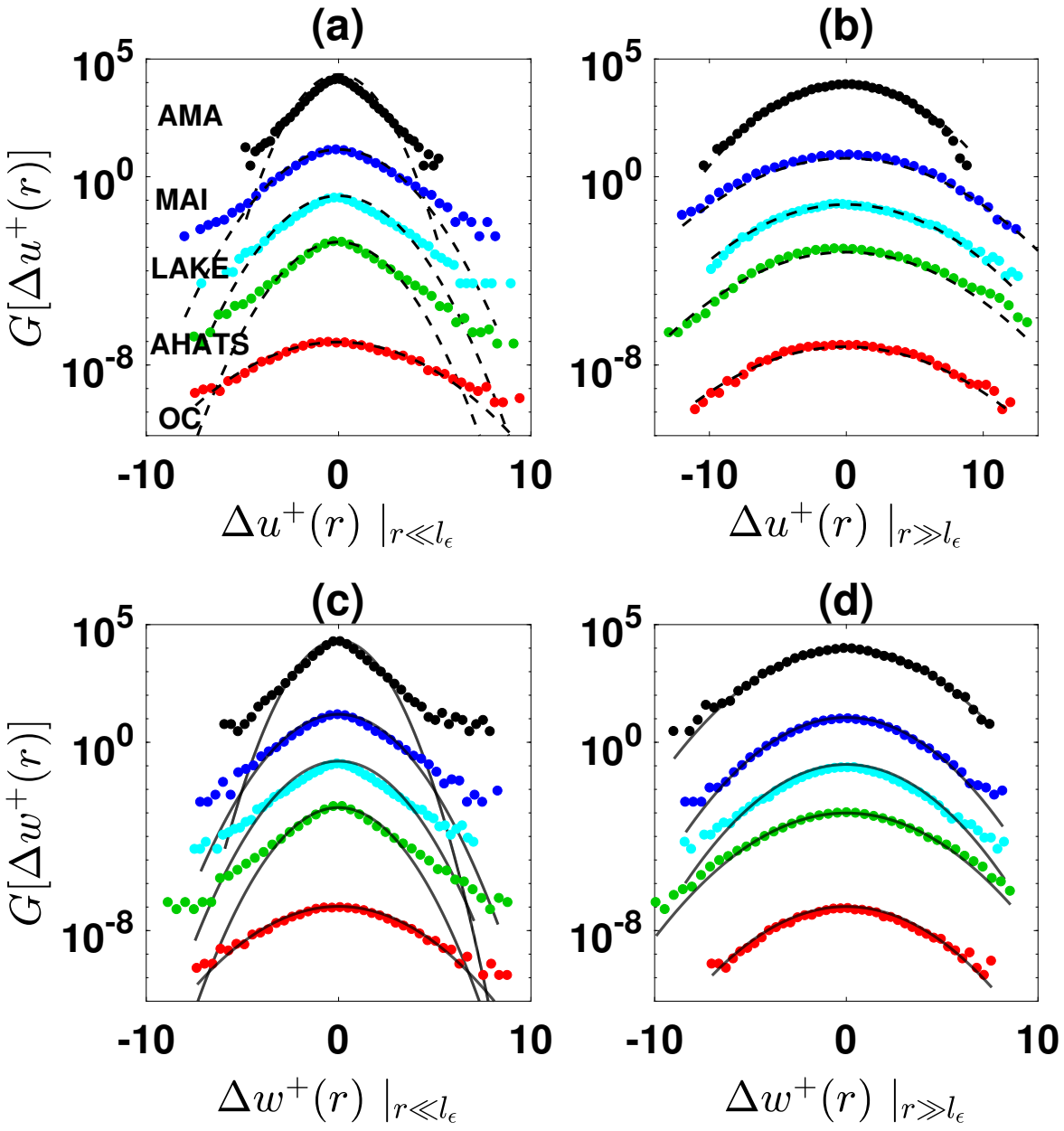

FIGURE 3.8: Probability density functions (*pdf*) of the normalized (by u_*) velocity differences. (a)-(b): $\Delta u^+(r)$ and (c)-(d): $\Delta w^+(r)$ at two selected separation distances. In (a)-(c), the separation distance is $r \ll l_\epsilon$ (isotropic range) and in (b)-(d) $r \gg l_\epsilon$ (anisotropic range). A Gaussian *pdf* with zero mean and a variance equal to that of the data is shown by black lines. Only the highest measurement height at each site is presented and all plots are shifted vertically for clarity.

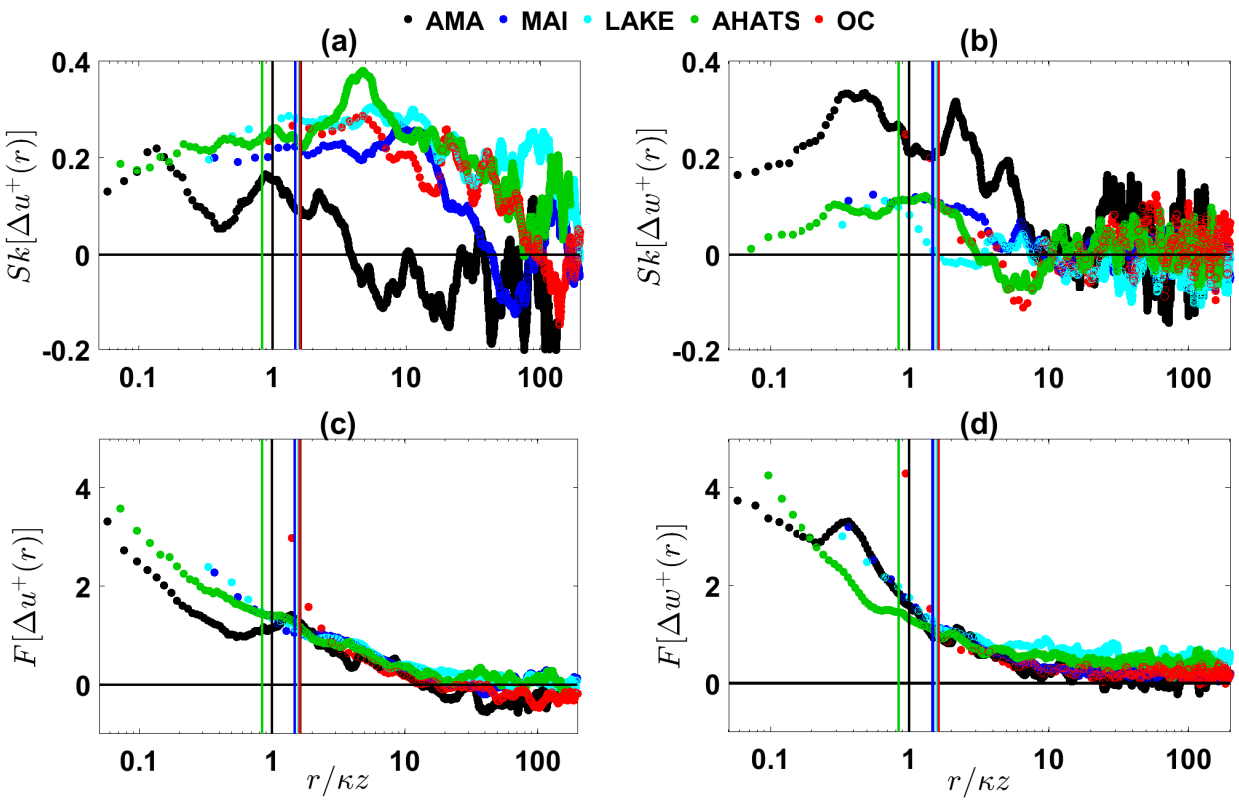

FIGURE 3.9: (a)-(b) Skewness (Sk) and (c)-(d) excess (above Gaussian value of 3) flatness factor (F) of the distributions of velocity differences as a function of $r/\kappa z$. Different sites are represented by colors consistent with Fig. 3.8. The vertical lines correspond to $r = l_\epsilon$ at each site.

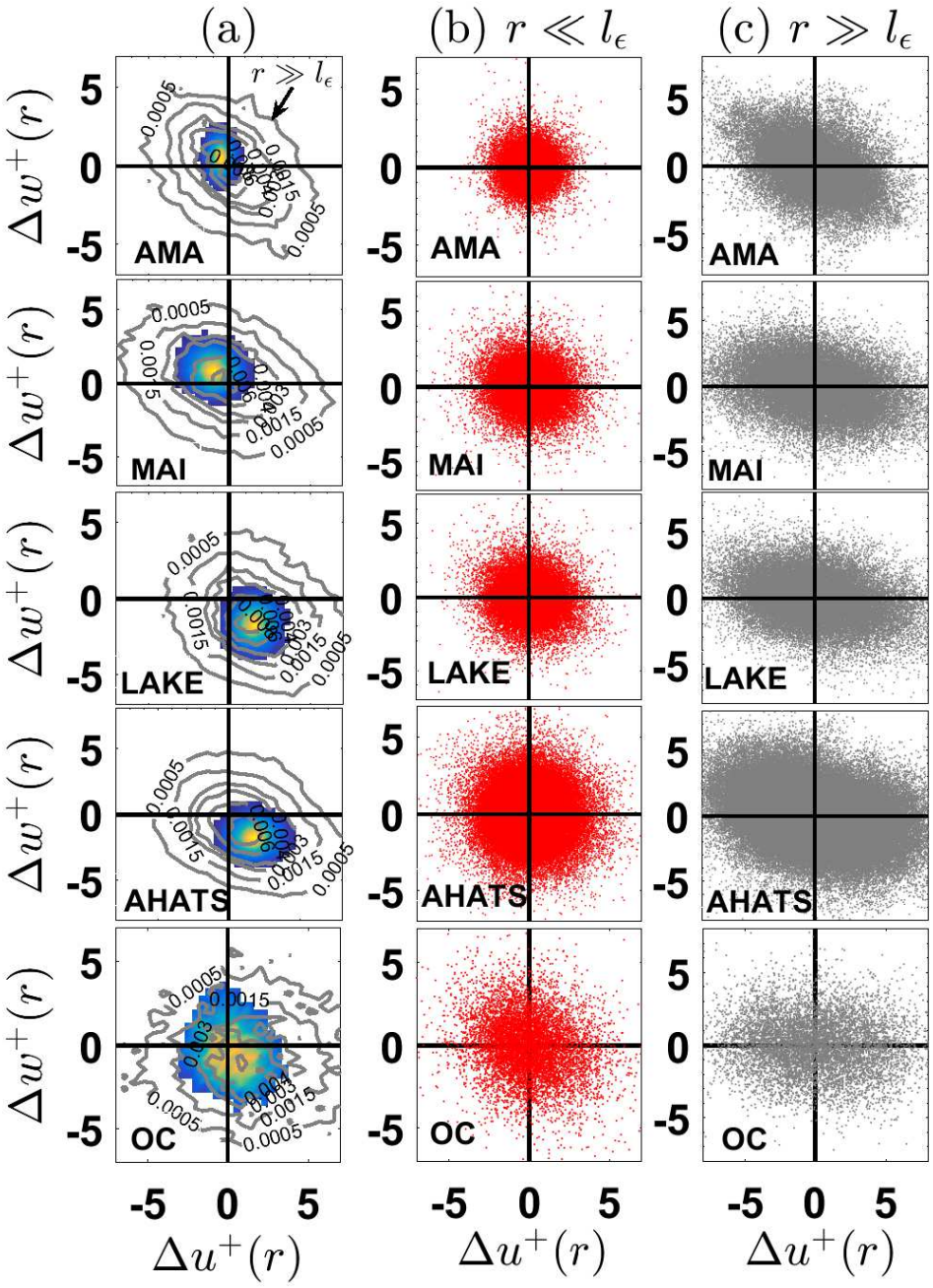

FIGURE 3.10: (a): Joint probability density functions (*pdf*) of $\Delta u^+(r)$ and $\Delta w^+(r)$ in the isotropic ($r \ll l_\epsilon$ indicated by colored contours) and anisotropic ($r \gg l_\epsilon$ indicated by gray contours) eddies. The joint *pdf* in (a) are calculated based on the scatter plot of $\Delta u^+(r)$ and $\Delta w^+(r)$ in (b) isotropic ($r \ll l_\epsilon$) and (c) anisotropic ($r \gg l_\epsilon$) range.

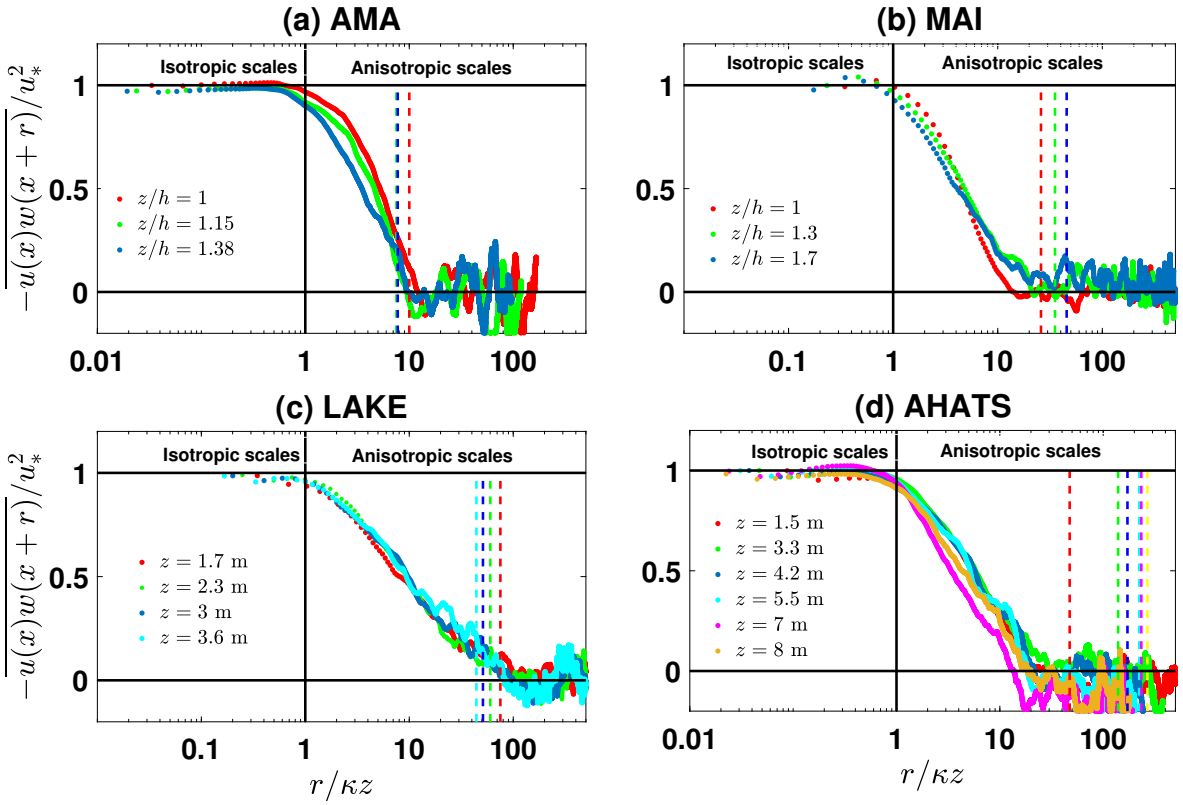

FIGURE 3.11: Lagged cross-correlation $\overline{u(x)w(x+r)}$ (note the negative sign) in Eq. (3.13) normalized by u_*^2 at all heights for each experiment. The dashed vertical lines correspond to the integral length scale L_u at each height, with their colors matching the legend for heights.

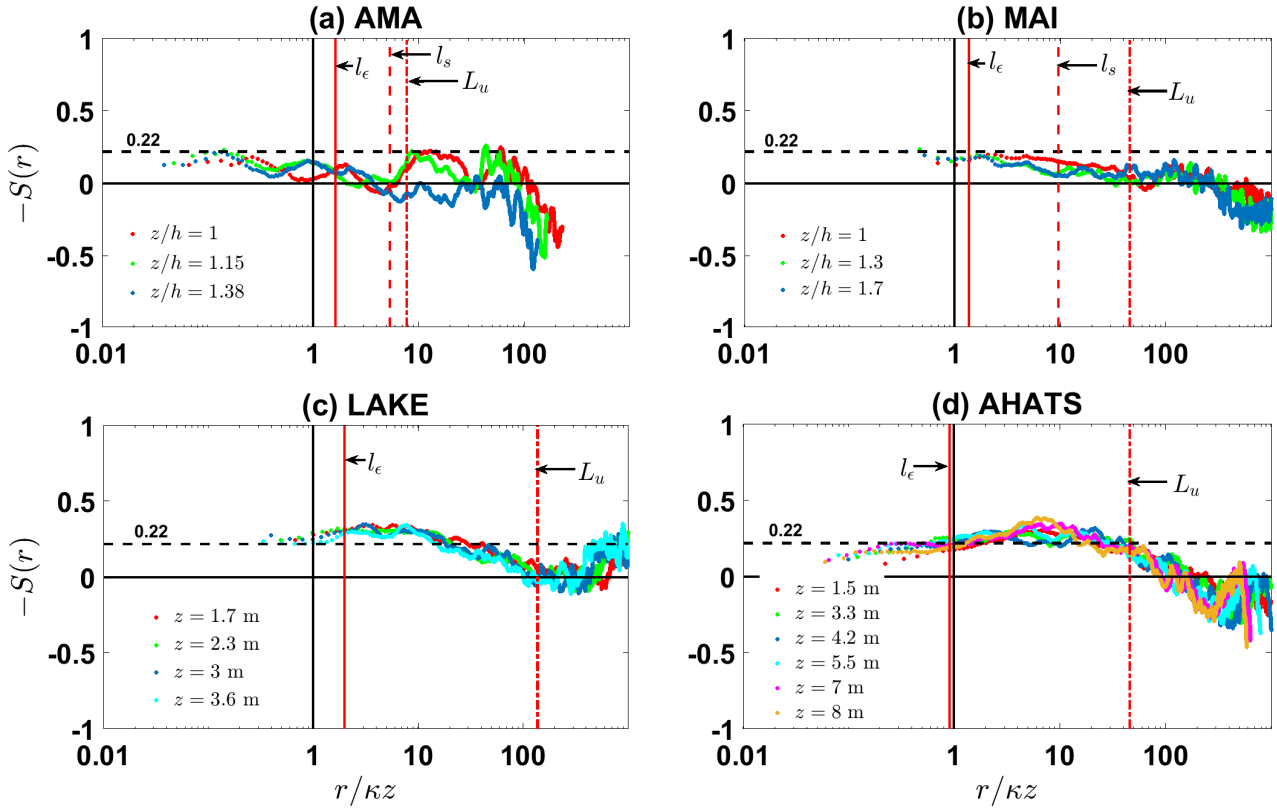

FIGURE 3.12: The negative of the structure skewness in Eq. (3.8) for the atmospheric experiments plotted against $r/\kappa z$ at each measurement height on a log-linear scale. The length scales l_ϵ, l_s, and L_u are shown as solid, dashed, and dash-dotted red lines respectively. These are from the highest measurement height in each experiment for illustration. The value $S(r) \approx -0.22$ [see Eq. (3.11)] expected in the isotropic range is shown as black dashed horizontal lines.

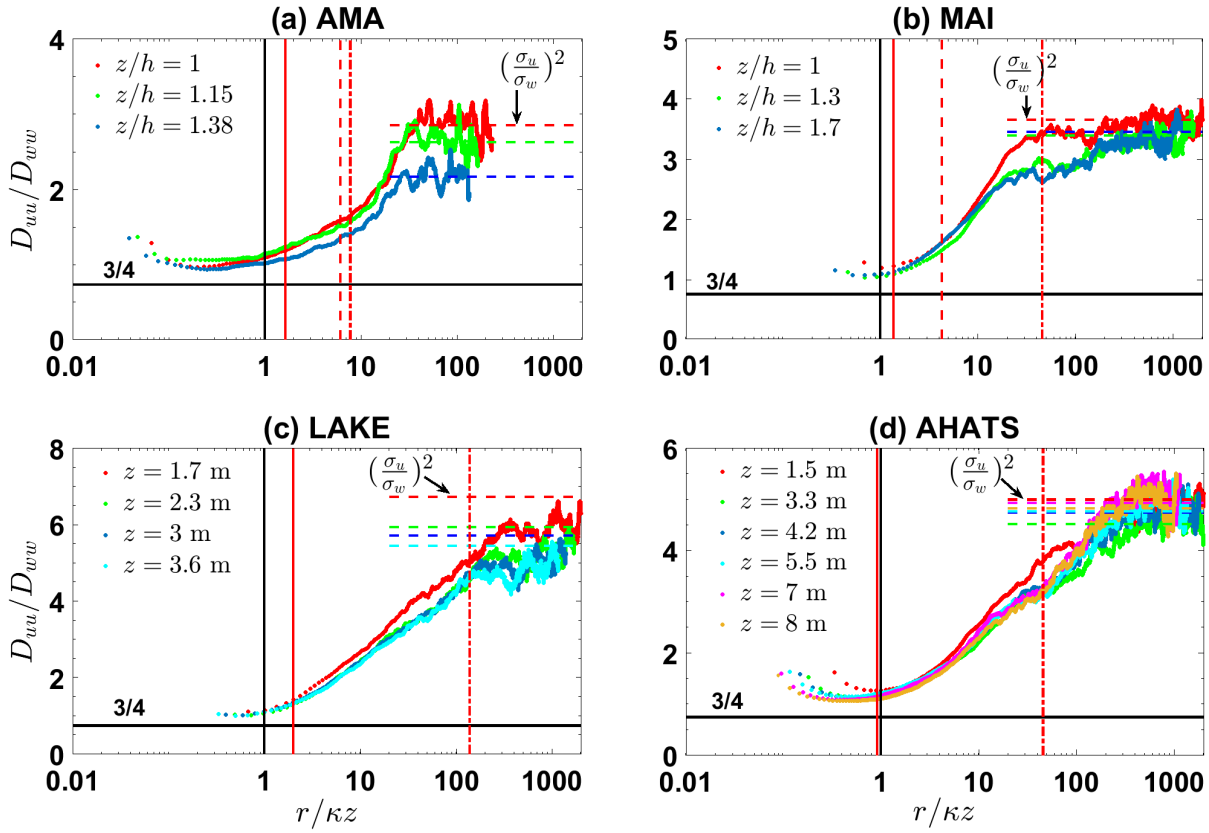

FIGURE 3.13: Ratio of the structure functions D_{uu}/D_{ww} plotted against $r/\kappa z$ at each measurement height on a log-linear scale. Similar to Fig. 3.12, the length scales l_ϵ, l_s, and L_u are shown as solid, dashed, and dash-dotted red lines respectively. The horizontal dashed lines represent the ratio $D_{uu}/D_{ww} = (\sigma_u/\sigma_w)^2$ (calculated from the data) expected at the very large scales, while black horizontal lines correspond to $D_{uu}/D_{ww} = 3/4$ in the isotropic range.

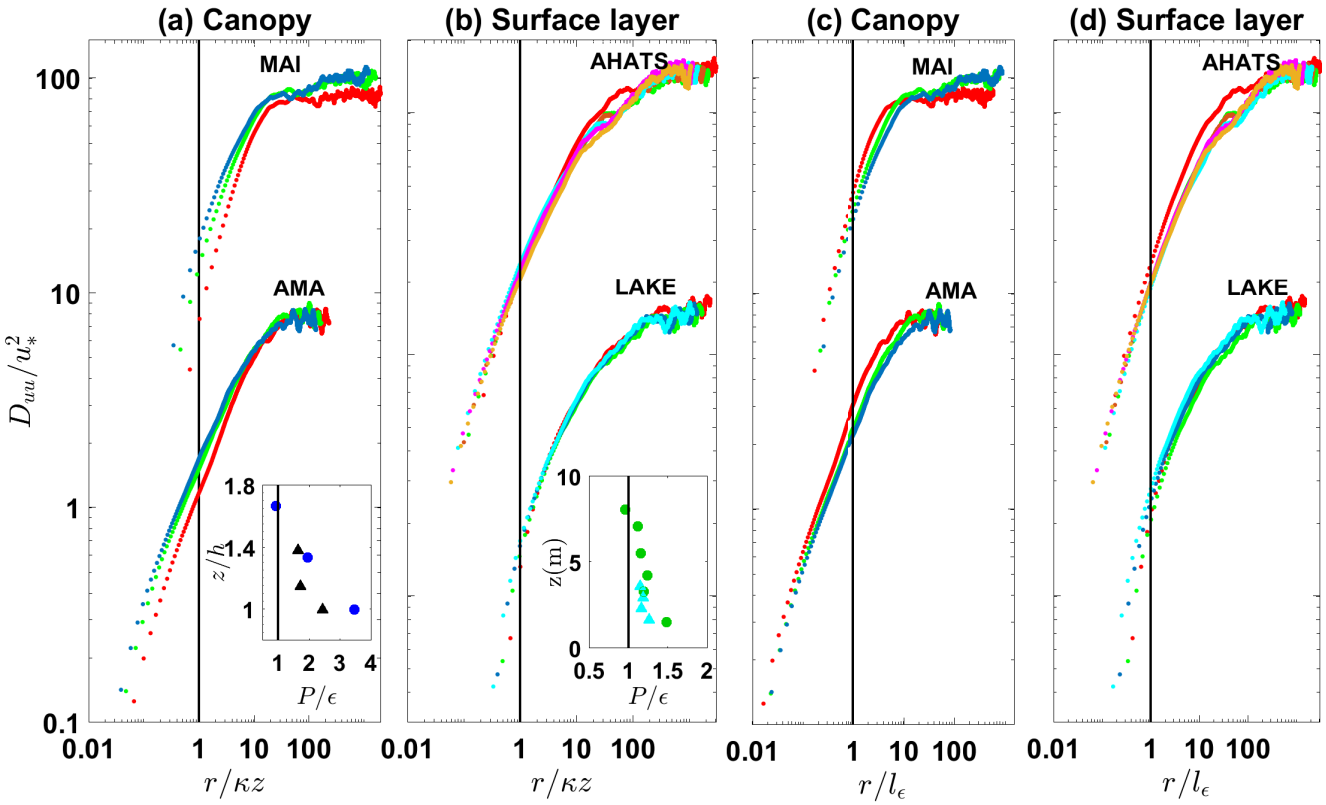

FIGURE 3.14: log-log plots of the normalized structure functions D_{uu}/u_*2 at all available measurement heights plotted against (a)-(b): $r/\kappa z$ and (c)-(d): r/l_ϵ. The canopy experiments **AMA** and **MAI** are plotted in (a) and (c), while the ASL experiments are shown in (b) and (d). Different colors correspond to different heights in each experiment. Plots are shifted vertically (same multiplication factor for each experiment) for clarity. The inset plots in (a) and (b) are the vertical profiles of the ratio P/ϵ, with circle symbols in the insets within (a) and (b) being for the **MAI** canopy and **AHATS** experiments respectively, and triangle symbols (insets in (a) and (b)) for the **AMA** canopy and **LAKE** experiments respectively.

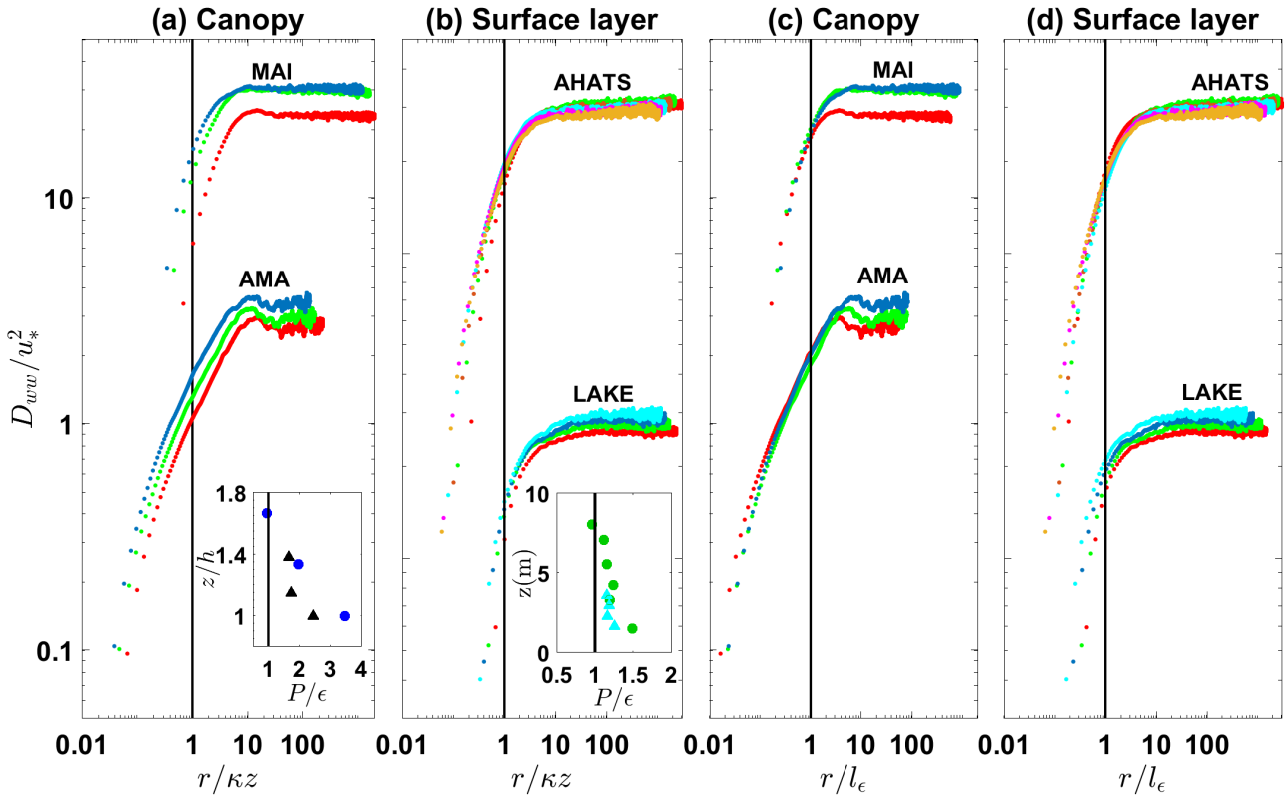

FIGURE 3.15: Same as Fig. 3.14 for D_{ww}/u_*^2.

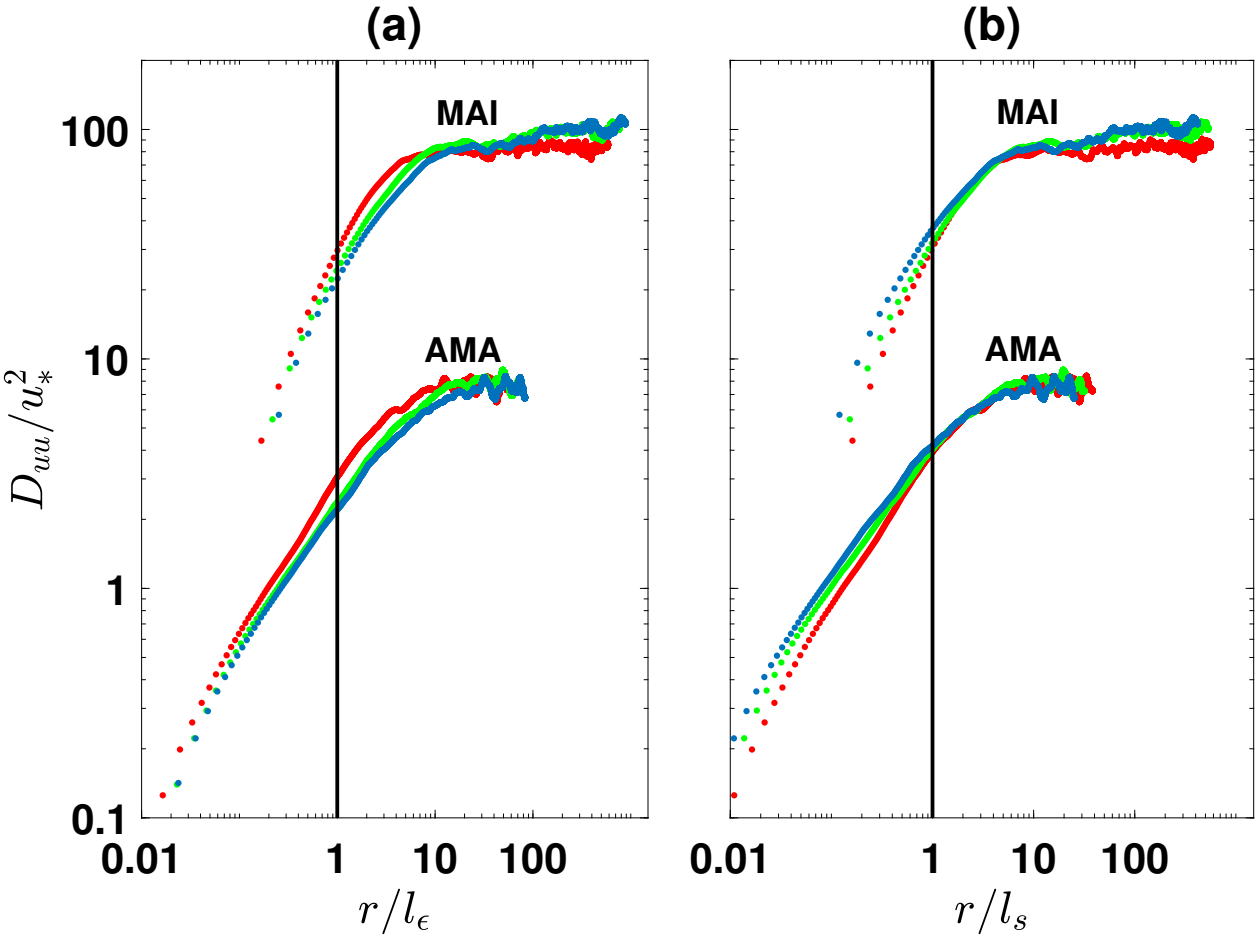

FIGURE 3.16: log-log plots of the normalized structure functions D_{uu}/u_*2 at all available measurement heights for the canopy experiments only, plotted against (a): $r/_\epsilon$, and (b): r/l_s.

4

The nonlocal character of turbulence asymmetry in the convective atmospheric boundary layer

4.1 Introduction

Despite their introduction some 140 years ago by Boussinesq, eddy diffusivity and eddy viscosity (or simply K-theory) models remain key concepts in turbulence research. According to McComb (2004), they qualify as the first successful application of renormalization group (RNG) methods, well before RNG's formal development in quantum field theory. The use of K-theory has made it possible to estimate and model turbulent fluxes in natural systems operating at Reynolds numbers that are simply too large to resolve in direct numerical simulations. However, the failure of K-theory in the convective atmospheric boundary layer (CABL) continues to draw research interest for an alternative that retains their simplicity. The CABL is a common daytime occurrence over the land surface, and is primarily characterized by ascending buoyant plumes that originate at the heated surface and evolve to a length scale comparable to the boundary layer depth h. These semi-organized eddies are accompanied by weaker subsiding (descending) plumes associated with entrain-

ment fluxes at the boundary layer top, leading to an asymmetry in the turbulence structure and hence in the vertical transport of scalars (e.g. heat, humidity) within the CABL. This perspective of a global boundary layer consisting of large-scale updrafts (bottom-up) and downdrafts (top-down) is now known to be the principal flux transport mechanism of heat in the well-mixed layer. Often referred to as nonlocal transport, as opposed to local mean gradient-diffusion closures (K-theory) driven by mean scalar gradients, a variety of modeling approaches has emerged over the past decades to explain and model the effects of these nonlocal large-eddies on turbulent fluxes. The tenets of such models descend from different schools of thought in the atmospheric boundary layer literature, and apart from minor advantages to each model over the others in certain situations, they involve some commonalities and invariably have comparable performance. This begs the question as to whether there is a unifying "umbrella" framework that encodes the mechanisms of vertical transport of scalars in the CABL, attributes the differences among the available models to derivatives of some parent process, and lends itself to a wider variety of applications that require more efficient parametrization of boundary layer processes.

In that respect, the vertical transport of heat in the clear-air (dry), horizontally homogeneous, quasi-stationary, convective atmospheric boundary layer is considered here. This setting has a long history in the pedagogy of atmospheric boundary layer turbulence and was considered in the early works of Ertel (1942), Priestley and Swinbank (1947), Deardorff (1966), and Zeman and Lumley (1976) on failures of K-theory. It was evident that in the well-mixed portion of convective boundary layers, finite heat fluxes coexist with negligible vertical gradients in the corresponding mean potential temperature (often referred to as 'zero-gradient' flow). The local eddy-diffusivity approach was therefore insufficient to explain such fluxes in sign and magnitude. The latter model assumes that the vertical flux of a turbulent scalar quantity, such as the potential temperature θ, is proportional to the gradient in its

local mean value (Θ) using a turbulent heat diffusivity K_H, such that (e.g. Stull, 1988)

$$\overline{w\theta} = -K_H \frac{\mathrm{d}\Theta}{\mathrm{d}z}, \tag{4.1}$$

where w is the turbulent fluctuation in the vertical velocity component and z is the vertical coordinate. Henceforth, small letters represent instantaneous turbulent fluctuations in a variable, capital letters are reserved for mean quantities, and overbars represent averaging over coordinates of statistical homogeneity (time and planar space here). Figure 4.1 is a sample result from a Large Eddy Simulation (LES) run described in later sections that illustrates the limitation of K-theory in CABL, where $\mathrm{d}\Theta/\mathrm{d}z = 0$, yet $\overline{w\theta} > 0$. In fact, the upper part of the CABL experiences both positive gradients and fluxes, which reflects the ability of buoyancy-driven plumes to transport warm air from the surface to the top of the boundary layer and hence ascend counter to the gradient in the mean potential temperature (e.g. Deardorff, 1972; Wyngaard and Weil, 1991). This observation initiated interest in nonlocal large-eddy flux transport as means to correct for K-theory and improve the parametrization of the CABL in regional and general circulation models.

While there is a significant body of literature and reviews on this topic (e.g. Zilitinkevich et al. (1999) and van Dop and Verver (2001)), a brief summary of the common modeling approaches correcting for nonlocal effects is presented here:

(i) Eddy Diffusivity-Counter Gradient (EDCG): The premise of this approach is the addition of a counter-gradient term (γ) to Eq. (4.1) (Deardorff, 1972; Troen and Mahrt, 1986; Holtslag and Moeng, 1991; Holtslag and Boville, 1993)

$$\overline{w\theta} = -K_H \left(\frac{\mathrm{d}\Theta}{\mathrm{d}z} - \gamma \right), \tag{4.2}$$

such that the term $K_H\gamma = \overline{w\theta}_{(NL)}$ represents the nonlocal (NL) component of the

heat flux. Deardorff (1972) initially suggested

$$\gamma = \beta \frac{\sigma_\theta^2}{\sigma_w^2}, \tag{4.3}$$

where $\beta = g/T_0$ is the buoyancy parameter, g is the gravitational acceleration, T_0 is a reference absolute temperature, and $\sigma_\theta^2 = \overline{\theta^2}$ and $\sigma_w^2 = \overline{w^2}$ are the variances in potential temperature and vertical velocity respectively. A limitation to Eq. (4.3) is the fact that σ_θ^2 and σ_w^2 can be large and even comparable to the gradient-diffusion term in the atmospheric surface layer where K-theory is expected to hold. Improved parametrization appeared in the works of Troen and Mahrt (1986) and Holtslag and Moeng (1991), where the former proposed an expression for γ to be compatible with the surface layer similarity theory resulting in:

$$\gamma = C \frac{\overline{w\theta}_0}{w_s h}, \tag{4.4}$$

where C is a proportionality constant, $\overline{w\theta}_0$ is the kinematic surface heat flux, h is the boundary layer height, $w_s \simeq 0.65 w_*$ (convective limit) is a mixed-layer velocity scale, and $w_* = (\beta \overline{w\theta}_0 h)^{1/3}$ is known as Deardorff's convective velocity scale (Deardorff, 1970). With a simple parametrization of the gradient in the third-order moment ($\overline{ww\theta}$), based on the LES results of Moeng and Wyngaard (1989), Holtslag and Moeng (1991) expressed the countergradient correction as

$$\gamma \propto w_* \frac{\overline{w\theta}_0}{\sigma_w^2 h}, \tag{4.5}$$

thereby accounting for the effects of the bulk parameters (w_*, h, and $\overline{w\theta}_0$) of the CABL in the heat flux profile. In this EDCG framework, the height-dependent turbulent heat diffusivity is considered proportional to the vertical velocity variance and an appropriate timescale ($K_H \propto \tau \sigma_w^2$) analogous to a Taylor diffusion (**?**).

Nevertheless, rather than a Lagrangian timescale as in Taylor's original work (**?**), τ here is associated with Rotta's return-to-isotropy timescale (Deardorff, 1972) or the mean turbulence kinetic energy (TKE) dissipation rate (Holtslag and Moeng, 1991).

(ii) Transport Asymmetry (TA): In a remarkable series of papers, Wyngaard and Brost (1984), Moeng and Wyngaard (1984), Moeng and Wyngaard (1989), Wyngaard and Weil (1991), and Wyngaard and Moeng (1992) introduced and formulated the concept of asymmetry in the vertical diffusion of scalars in the CABL. In particular, they distinguished bottom-up (driven mostly by surface flux) from top-down diffusion (driven by entrainment flux), noting that these mechanisms have different profiles of eddy diffusivity. This concept incorporated the skewness of the vertical velocity into the nonlocal heat flux representation, where $\overline{w\theta}_{(NL)}$, with the assumption of a linear flux profile (finite gradient), reads (Eq. (43) in Wyngaard and Weil, 1991)

$$\overline{w\theta}_{(NL)} = -\frac{S_w \sigma_w T_L}{2} \frac{\mathrm{d}\overline{w\theta}}{\mathrm{d}z}, \tag{4.6}$$

where $S_w = \overline{w^3}/\sigma_w^3$ is the skewness of w and T_L is a Lagrangian timescale. While Cuijpers and Holtslag (1998) argued that little improvement is gained by including S_w and that the vertical velocity variance remains more significant for the nonlocal flux, we note that Wyngaard and Weil (1991) assumed a skewed but homogeneous turbulence in most of the CABL, i.e. $\mathrm{d}S_w/\mathrm{d}z = 0$ for $0.1h < z < 0.9h$. Another feature of Eq. (4.6) is that it implies a zero nonlocal flux ($\overline{w\theta}_{(NL)} = 0$) in the surface layer where $\mathrm{d}\overline{w\theta}/\mathrm{d}z = 0$ (see Figure 4.1), as opposed to Eqs (4.4) and (4.5).

(iii) Third-order Moment parametrization (TOMP): This approach is directly related to second-order closure models of the heat flux and temperature variance bud-

gets. The fact that the mixed third-order moments (TOM), namely the flux of potential temperature flux ($\overline{ww\theta}$) and flux of potential temperature variance ($\overline{w\theta\theta}$) are responsible for nonlocal transport in the CABL called attention for their parametrization. The TOM are often obtained by solving the corresponding budget equations that involve fourth-order moments (FOM) with the quasi-normal approximation (Canuto et al., 1994), or mass-flux decomposition of the higher-order terms (e.g. Abdella and McFarlane, 1997; Gryanik and Hartmann, 2002). Examples of such parametrization are (Abdella and McFarlane, 1997)

$$\overline{ww\theta} = S_w \sigma_w \overline{w\theta}, \tag{4.7}$$

$$\overline{w\theta\theta} = S_w \sigma_\theta \overline{w\theta}. \tag{4.8}$$

Mironov et al. (1999) proposed that the skewness of potential temperature ($S_\theta = \overline{\theta^3}/\sigma_\theta^3$) should replace S_w in Eq. (4.8).

(iv) Eddy Diffusivity-Mass Flux (EDMF): This model parametrizes the turbulent flux in the CABL on the basis of separating the boundary layer into strong and narrow updrafts and a surrounding turbulent environment. The formulation of this method was initially developed for convective transport in cumulus clouds and was later extended to the full boundary layer (Siebesma and Cuijpers, 1995; Siebesma and Teixeira, 2000; Siebesma et al., 2007). The total turbulent flux of potential temperature is then due to the contributions from the updrafts, the surrounding environment, and a mass-flux term:

$$\begin{aligned}\overline{w\theta} = a_u \overline{w\theta}^u + (1 - a_u)\overline{w\theta}^e \\ + a_u(w_u - \overline{w})(\Theta_u - \Theta_e),\end{aligned} \tag{4.9}$$

where the sub- or superscripts u and e denote the strong updrafts and the surrounding environment respectively, a_u is the fractional area occupied by the up-

drafts, w_u and $\overline{w}$ are the mean vertical velocity components in the updraft and the complementary environment, and Θ_u and Θ_e are the corresponding mean potential temperatures. Neglecting the first term in Eq. (4.9) ($a_u \ll 1$), and with the approximation $\Theta_e = \Theta$, the EDMF model is usually reduced to

$$\overline{w\theta} = -K_H \frac{\mathrm{d}\Theta}{\mathrm{d}z} + M(\Theta_u - \Theta), \tag{4.10}$$

where $\overline{w\theta}^e = -K_H \mathrm{d}\Theta/\mathrm{d}z$ represents the eddy-diffusivity term and $M = a_u(w_u - \overline{w})$ defines the convective mass flux. The second term in Eq. (4.10) is equivalent to the nonlocal heat flux $\overline{w\theta}_{(NL)}$, and requires parametrization of the mass flux M, an updraft model for w_u and Θ_u, besides the eddy-diffusivity K_H.

Notwithstanding the differences across the models described above, it is evident in all cases that the large-eddy coherent motion in the CABL primarily dictates the vertical diffusion of scalars. It is also apparent that the nonlocal fluxes are a manifestation of the inherent asymmetry in vertical transport, which is in turn associated with the TOM (S_w, S_θ, $\overline{ww\theta}$, and $\overline{w\theta\theta}$) and their vertical gradients. This hints at the importance of the non-Gaussian nature of the turbulence structure in the CABL as means to explain the nonlocal transport, where such asymmetry must exhibit itself in the joint probability density function (JPDF) of vertical velocity and potential temperature. While the latter argument is only intuitive, this JPDF received little attention in the context of nonlocal scalar flux literature, except for the work of Wyngaard and Moeng (1992) and **?** that provided a reasonable starting point for the work here.

The second-moment budget of the sensible heat flux in the weakly-to-strongly convective atmospheric boundary layer is considered here to explore the role and relative importance of the TOM on nonlocal flux transport. The premise is that the non-Gaussian JPDF of vertical velocity and potential temperature encodes all

the properties of these TOM and hence provides a unifying framework to explain all the underlying physical mechanisms of nonlocal flux corrections to K-theory. Since the essence of second-order closure modeling is the proper parametrization of the TOM, the aforementioned models (EDCG, TA, TOMP, and EDMF) seem to be a natural extension to the characteristics of this JPDF. Although the intent here is not to provide a fully prognostic closure replacing earlier models for flux parametrization, we build on the works of Nakagawa and Nezu (1977) and Raupach (1981) on conditional sampling (quadrant analysis) and the cumulant-discard expansion of the Gram-Charlier JPDF of w and θ to unfold dynamically interesting connections between EDCG, TA, TOMP, and EDMF models and the ejection-sweep events in the flow field. While the aforestated work examined the fractional contributions of each quadrant to the Reynolds stresses (momentum fluxes), the analysis can be extended to scalar fluxes ($\overline{w\theta}$) (Katul et al., 1997a; Cava et al., 2006; Poggi and Katul, 2007). It is to be noted, however, that the use of the terms ejections and sweeps here is not a simple mapping of what is commonly understood in the context of momentum fluxes in the surface layer (i.e. ejection-sweep cycle). Rather, an analogy of the notation used by Raupach (1981) is made to quadrant analysis of the heat flux for convenience of notation, and ejection/sweep 'events' is used throughout in lieu of 'cycle'. This point is revisited in subsection 4.2.3 when introducing the nomenclature for the quadrant analysis. Most importantly, conditional sampling of the (w,θ) JPDF quantifies the fractional contributions of each quadrant to the total heat flux, and ties these contributions to physical characteristics of the flow field, namely the ejections, sweeps, inward and outward interactions. Connections between these flow mechanisms and the TOM then provides a gateway to explain their relative roles in nonlocal transport and their representation in models such as EDCG, TA, TOMP, and EDMF. The analysis uses a suite of LES experiments to provide the required profiles of all moments up to third-order to complement the work, and in the in-

terest of completeness, the paper also examines the performance of various closure time/length scales and turbulent diffusivity profiles.

4.2 Theory

As noted earlier, the CABL considered here is a clear-air, stationary ($\partial(.)/\partial t = 0$), planar homogeneous ($\partial(.)/\partial x = \partial(.)/\partial y = 0$), high Reynolds and Peclet numbers (negligible molecular viscosity), and with negligible Coriolis force. The coordinate system is defined such that x, y, and z form the longitudinal, lateral, and vertical directions, respectively. The usual Reynolds decomposition notation is employed throughout, where all variables are decomposed into stationary mean (capital letters) and fluctuating (small letters) quantities. In this section, the characteristics of the heat flux budget with various simplifying closure assumptions is presented. These assumptions are then tested and discussed in section 4.4.

4.2.1 The heat flux budget

Using the aforementioned simplifying conditions and adopting the Boussinesq approximation, the heat flux budget in the convective boundary layer reduces to

$$\frac{\partial \overline{w\theta}}{\partial t} = 0 = \underbrace{-\sigma_w^2 \frac{\mathrm{d}\Theta}{\mathrm{d}z}}_{\underline{M}} \underbrace{-\frac{\mathrm{d}\overline{ww\theta}}{\mathrm{d}z}}_{\underline{T}} \underbrace{-\frac{1}{\rho_0}\theta\frac{\overline{\mathrm{d}p}}{\mathrm{d}z}}_{\underline{P}} \underbrace{+\beta\overline{\theta^2}}_{\underline{B}}, \tag{4.11}$$

where ρ_0 is a reference-state air density and p is the pressure fluctuation referenced to the hydrostatic state and its finite value is attributed to turbulence. The flux production/destruction terms on the right hand side (rhs) of Eq. (4.11) are, respectively, the mean-gradient production ($\underline{\mathrm{M}}$), the turbulent flux transport ($\underline{\mathrm{T}}$), the pressure gradient-potential temperature covariance ($\underline{\mathrm{P}}$), and the buoyancy production ($\underline{\mathrm{B}}$). The term $\underline{\mathrm{P}}$ acts as a destruction/sink term for the heat flux $\overline{w\theta}$, and

following Rotta (1951), who initially proposed the return-to-isotropy parametrization to the pressure-velocity gradient covariance in turbulent shear flows, numerous studies have extended this parametrization to incorporate the contributions from the mean-gradient, buoyancy, and Coriolis effects (Jones and Musonge, 1984; Moeng and Wyngaard, 1986; Andrén and Moeng, 1993; Mironov, 2001). Since the Coriolis force is neglected here, the general form of the parametrization of $\underline{\mathrm{P}}$ is

$$P = -\frac{1}{\rho_0}\theta\overline{\frac{\mathrm{d}p}{\mathrm{d}z}} = -C_1\frac{\overline{w\theta}}{\tau_1} - C_2\beta\overline{\theta^2} + C_3\sigma_w^2\frac{\mathrm{d}\Theta}{\mathrm{d}z}, \tag{4.12}$$

where the first term on the rhs represents Rotta's return-to-isotropy (slow) part and is inversely proportional to a relaxation timescale τ_1, and the last two terms are referred to as the rapid part. Typical values of the constants are $C_1 = 3$, $C_2 = 1/3$-$1/2$, and $C_3 = 2/5$. The performance of the parametrization in Eq. (4.12) with different relaxation timescales will be evaluated with LES simulations in section 4.4. Using Eq. (4.12) and maintaining the constants for the time being, the flux budget Eq. (4.11) can be written as

$$\overline{w\theta} = \frac{C_3 - 1}{C_1}\tau_1\sigma_w^2\left[\frac{\mathrm{d}\Theta}{\mathrm{d}z} - \frac{1}{(C_3-1)\sigma_w^2}\frac{\mathrm{d}\overline{ww\theta}}{\mathrm{d}z} + \frac{1-C_2}{(C_3-1)\sigma_w^2}\beta\overline{\theta^2}\right], \tag{4.13}$$

where, again, $C_3 < 1$ and has been predicted to be 2/5 for isotropic turbulence using Rapid Distortion Theory as discussed in **?**. Equation (4.13) defines a general framework for the heat flux within the convective boundary layer and is analogous to the form of Eq. (4.2) that corrects for countergradient fluxes, with a diffusivity $K_H \propto \tau_1\sigma_w^2$.

The first term on the rhs of Eq. (4.13) is responsible for the local flux and the last two terms are the origin of nonlocal fluxes. The ratio of variances term

($\propto\sigma_\theta^2/\sigma_w^2$) resulting from buoyant production is the countergradient correction obtained by Deardorff (1972) after ignoring the flux transport term, while Holtslag and Moeng (1991) parametrized the latter with w_*, h, and $\overline{w\theta}_0$ and assumed that the pressure gradient-temperature covariance cancels the buoyancy effects. The implicit assumption that the same diffusivity is applicable to the local and nonlocal terms is debatable (e.g. Frech and Mahrt, 1995), and render the choice of the return-to-isotropy timescale (τ_1) elusive. A local timescale such as $\tau_1\propto TKE/\epsilon$, where ϵ is the TKE disspiation rate, may not be characteristic of nonlocal fluxes, whereas a large-eddy turnover timescale such as $\tau_1\propto h/w_*$ is not adequate for localized eddies. By analogy to Eq. (4.2), the countergradient term reads

$$\gamma = \frac{1}{(C_3-1)\sigma_w^2}\frac{\mathrm{d}\overline{www\theta}}{\mathrm{d}z} - \frac{1-C_2}{(C_3-1)\sigma_w^2}\beta\overline{\theta^2}. \tag{4.14}$$

The contribution of each of these two terms, both in their magnitude and sign (source/sink) will be discussed later. Equation (4.14) highlights the importance and the requirement of closure assumptions for the turbulent flux transport term in the context of nonlocal fluxes.

4.2.2 Local closure to the turbulent flux transport

The most common closure for the turbulent transport of scalar fluxes is again down-gradient diffusion. The rationale is that, while the gradient in first-order moments is small in the well-mixed layer and hence Eq. (4.1) is insufficient, the approach can be valid for the non-vanishing gradients in turbulent second-order moments. This can be attributed to the fact that the equilibration between such turbulent quantities and their gradient is attained much faster than the equilibration between mean gradient and turbulent quantities. This closure results in the conventional form

$$\frac{\mathrm{d}\overline{www\theta}}{\mathrm{d}z} = -\frac{\mathrm{d}}{\mathrm{d}z}\left(\tau_2 q^2\frac{\mathrm{d}\overline{w\theta}}{\mathrm{d}z}\right), \tag{4.15}$$

where τ_2 and q are time and velocity scales respectively. The diffusivity here ($K_T = \tau_2 q^2$) is not necessarily identical to $K_H = \tau_1 \sigma_w^2$, and using Eq. (4.15), the heat flux budget in Eq. (4.13) can be written as a second-order ordinary differential equation

$$K_T \frac{\mathrm{d}^2 \overline{w\theta}}{\mathrm{d}z^2} + \left(\frac{\mathrm{d}K_T}{\mathrm{d}z}\right) \frac{\mathrm{d}\overline{w\theta}}{\mathrm{d}z} - \frac{C_1}{\tau_1} \overline{w\theta} + (C_3 - 1)\sigma_w^2 \frac{\mathrm{d}\Theta}{\mathrm{d}z} + (1 - C_2)\beta \overline{\theta^2} = 0. \tag{4.16}$$

For a turbulent heat flux that is linear in z, a negligible mean gradient term ($\propto \mathrm{d}\Theta/\mathrm{d}z$), and a constant K_T, Eq. (4.16) reduces to

$$\overline{w\theta} = \frac{1 - C_2}{C_1} \tau_1 \beta \overline{\theta^2}, \tag{4.17}$$

which implies that $\tau_1 < 0$ near the top of the CABL (where $\overline{w\theta} < 0$). It also requires that the quantity $\tau_1 \overline{\theta^2}$ be linear in z. Including the mean gradient term retrieves the model by Deardorff (1972) shown earlier in Eq. (4.3), and hence it follows that K_T must not be constant.

4.2.3 Conditional sampling and the ejection-sweep events

To characterize the total heat flux $\overline{w\theta}$ at a given height z in the CABL as the sum of contributions from different physical mechanisms, the JPDF of vertical velocity and potential temperature fluctuations, denoted by $J(w, \theta)$, and the conditional sampling of its four quadrants are considered. Such sampling methods were reviewed in **?**, Antonia (1981), and Bogard and Tiederman (1987). In analogy with momentum transport, four quadrants defined by the Cartesian axes of the scatter plot of w and θ are shown in Figure 4.2. Quadrants **I** ($w > 0$, $\theta > 0$) and **III** ($w < 0$, $\theta < 0$) contribute to positive heat fluxes but due to different physical mechanisms, namely warm air parcels moving upward and cold air parcels sinking, respectively. When the total heat flux $\overline{w\theta}$ is positive, which is the case for roughly the lower 80% of

the CABL (see Figure 4.1), quadrants **I** and **III** have a dominant contribution and are defined here as ejections and sweeps. While the terms ejections and sweeps are usually reserved for momentum fluxes, we adopt them here for heat fluxes with proper handling of the sign of the flux itself. Quadrants **II** ($w < 0$, $\theta > 0$) and **IV** ($w > 0$, $\theta < 0$) both contribute to negative fluxes associated with sinking warm air and rising cold air, respectively. The latter quadrants dominate in the top $\approx 20\%$ of the CABL when the total heat flux is negative due to entrainment from the free troposphere, and therefore events in these two quadrants are labeled as ejections and sweeps in this context. Additionally, ejections/sweeps as defined here are not analogous to updrafts/downdrafts used in the context of mass flux models. The latter are defined by conditioning on the vertical velocity fluctuations only, i.e. updrafts correspond to w being positive (or larger than some threshold), and downdrafts correspond to $w < 0$. In the quadrant analysis here, updrafts would then be reflected in quadrants **I** and **IV** (both with $w > 0$), and hence can contribute to positive heat fluxes (quadrant **I**) by carrying positive temperature fluctuations upward and negative heat fluxes (quadrant **IV**) by carrying negative temperature fluctuations upward. A similar picture follows for downdrafts being reflected in quadrants **II** and **III**. On the other hand, ejection and sweep events are hereafter limited to quadrants **I** and **III** respectively (or quadrants **II** and **IV** in the entrainment zone where the net heat flux is negative). This is the main physical difference between ejections and updrafts, or sweeps and downdrafts.

For the stationary flow in the CABL, the contribution to the total heat flux from quadrant i can be written as (Raupach, 1981)

$$\langle w\theta \rangle_i = \frac{1}{T_p} \int_0^{T_p} w(t)\theta(t) I_i \mathrm{d}t, \tag{4.18}$$

where the angle brackets denote conditional averaging, T_p is the averaging time

period, and the indicator function I_i is defined such that

$$I_i = \begin{cases} 1; & \text{if the events } (w,\theta) \text{ both occur in quadrant } i, \\ 0; & \text{otherwise,} \\ & \text{where } i = \text{I, II, III, IV.} \end{cases} \tag{4.19}$$

The fraction of heat flux contributed by quadrant i is then given by

$$F_i = \frac{\langle w\theta \rangle_i}{\overline{w\theta}}, \tag{4.20}$$

implying that, in the upward (positive) heat flux portion of the CABL, $F_i > 0$ when i is odd (ejections and sweeps) and $F_i < 0$ otherwise, with $F_1 + F_2 + F_3 + F_4 = 1$. The opposite occurs close to the entrainment zone where the heat flux is downward, i.e. $F_i > 0$ when i is even. It also follows that these fractional contributions are related to the JPDF by

$$F_i = \frac{1}{\overline{w\theta}} \int_{-\infty}^{\infty} \int_{-\infty}^{\infty} w\theta J(w,\theta) I_i \, \mathrm{d}w\mathrm{d}\theta, \tag{4.21}$$

and since $J(w,\theta)$ can be specified in terms of its moments (ideally infinite set), Eq. (4.21) provides a link between the fractional contributions (F_i) of each quadrant to the heat flux and the moments or cumulants of $J(w,\theta)$. For such a quadrant representation, the interest here is in the imbalance between the contributions of the rising warm air (quadrant **I**≡ ejections) and sinking cold air (quadrant **III** ≡ sweeps) to the positive heat flux, or otherwise the imbalance between quadrants **II** and **IV** in contributing to the negative heat flux. This imbalance reflects the relative importance of each of these mechanisms and can be quantified as

$$\begin{aligned} \Delta F &= \frac{\langle w\theta \rangle_{\text{sweeps}} - \langle w\theta \rangle_{\text{ejections}}}{\overline{w\theta}} \\ &= \begin{cases} F_{\text{III}} - F_{\text{I}}; & \text{when } \overline{w\theta} > 0, \\ F_{\text{IV}} - F_{\text{II}}; & \text{when } \overline{w\theta} < 0. \end{cases} \end{aligned} \tag{4.22}$$

The importance of the quantity ΔF lies in the fact that it can be represented in terms of the TOM by a cumulant-discard method (Nakagawa and Nezu, 1977). If the Gram-Charlier expansion of $J(w,\theta)$ is truncated at third-order, which is the minimum necessary to account for its non-Gaussian nature, ΔF can be written as (Raupach, 1981)

$$\Delta F = \frac{1}{R\sqrt{2\pi}}\left[\frac{R}{6}(M_{03} - M_{30}) + \frac{1}{2}(M_{21} - M_{12})\right], \tag{4.23}$$

where $R = \overline{w\theta}/\sigma_w\sigma_\theta$ is the correlation coefficient, and the moments M_{jk} are defined by

$$M_{jk} = \frac{\overline{w^k\theta^j}}{\sigma_w^k\sigma_\theta^j}, \tag{4.24}$$

and hence $M_{03} = \overline{w^3}/\sigma_w^3$ and $M_{30} = \overline{\theta^3}/\sigma_\theta^3$ define the skewness of the vertical velocity component and potential temperature respectively, while $M_{21} = \overline{w\theta\theta}/\sigma_w\sigma_\theta^2$ and $M_{12} = \overline{ww\theta}/\sigma_w^2\sigma_\theta$ are the central mixed-moment representation of the flux of potential temperature variance and flux of flux respectively. Equation (4.23) was derived for momentum transport in the atmospheric boundary layer, where $\overline{uw} < 0$, and hence it similarly applies to $\Delta F = F_{\mathrm{IV}} - F_{\mathrm{II}}$ in the context of heat flux transport. Nonetheless, it can be adapted to the positive heat flux case ($\Delta F = F_{\mathrm{III}} - F_{\mathrm{I}}$) by simply switching the sign of w in the terms where it occurs an odd number of times. While the various models introduced above incorporate some TOM in representing the nonlocal heat flux, Eq. (4.23) encompasses the role of each TOM in shaping the asymmetry in $J(w,\theta)$ and connects this role to the imbalance between different flow features in contributing to the total heat flux in the CABL.

4.3 LES runs

The LES code used here solves the three-dimensional filtered equations for momentum and temperature written in rotational form. Spatial derivatives are discretized through second-order centered finite differences in the vertical and pseudospectral differentiation in the horizontal directions. The second-order Adams-Bashforth method is used for time advancement. The details of the LES code, the numerical scheme used, the grid generation and subgrid scale (SGS) modeling, and post-processing of LES output can be found in Kumar et al. (2006) and **?**. The SGS model used is the Lagrangian-averaged scale-dependent dynamic model (Bou-Zeid et al., 2005), which applies the dynamic procedure (Germano et al., 1991) by averaging over Lagrangian trajectories to determine the Smagorinsky coefficient. The upper boundary condition is stress-free, zero temperature gradient, and no flow through the boundary, and periodic boundary conditions are employed in the horizontal. A damping layer is also used near the top of the domain to prevent the reflection of gravity waves from the upper boundary. The wall model is based on imposing Monin-Obukhov similarity in a local sense.

A total of ten LES runs spanning a range of $-h/L$ from 7.2 to 48.9 was conducted, where $L = -u_*^3 T_0/\kappa g \overline{w\theta}_0$ is the Obukhov length, κ is the von Kármán constant, and u_* is the friction velocity. The LES domain was set to $12 \times 12 \times 2$ km with a grid resolution of $160 \times 160 \times 160$ ($75 \times 75 \times 12.5$ m in the x, y, and z directions respectively) and a time step of $\Delta t = 0.05$ s. The initial depth of the boundary layer was set to $h = 1000$ m, and the simulations were forced by a constant pressure gradient expressed in terms of the geostrophic velocity U_g using the geostrophic approximation, and a constant surface heat flux was imposed. The range of $-h/L$ was obtained by systematically changing U_g between 9 and 15 m s^{-1} and $\overline{w\theta}_0$ between 0.1 and 0.24 K m s^{-1}. Table 4.1 summarizes the properties of the ten simulations

including the forcing, characteristic length ($-L$ and h) and velocity (u_* and w_*) scales. These parameters are based on averages from hours 4 to 5 of the simulations. Examination of hourly averages of mean profiles showed that the moments are well converged after 4 hours physical time, i.e. approximately 20 large eddy turnover times (h/w_*). The height of the CABL h is defined as the location where the sensible heat flux is minimum ($\approx -0.2\overline{w\theta}_0$).

Figure 4.3 shows the LES-resolved profiles of the variances and third-order moments of w and θ for the ten simulations, normalized by a combination of (w_*, θ_*). Figure 4.4 is the same as Figure 4.3 but the profiles are normalized by a $(\sigma_w, \sigma_\theta)$ combination to show the moments M_{jk}. It is clear that the TOM are not simply related by constants as noted by the wind tunnel experiment of Raupach (1981). While the moments M_{21} and M_{12} have fairly similar profiles, their gradients change sign at different heights in the mixed layer. This also applies for any one moment across the ten simulations, where the inflection point occurs at higher locations with increasing w_*/u_*. The skewness of vertical velocity, M_{03} is not height-independent in the mixed layer as assumed by Wyngaard and Weil (1991) leading to their parametrization in Eq. (4.6). The terms in the heat flux budget (Eq. (4.11)) are now shown in Figure 4.5 for cases S1 and S10 for illustration. These cases are the end-members of the LES simulations here with S1 ($w_*/u_* = 4.93$) and S10 ($w_*/u_* = 2.61$) representing strongly and weakly convective simulations (see Table 4.1). These are directly obtained from the LES and the pressure term is calculated as a residual for the heat flux budget. All the terms are comparable in the middle of the CABL (around $z/h = 0.5$), and the turbulent transport (T) becomes a source for heat flux comparable to the buoyancy term in this region.

4.4 Results and Discussion

Using the overall statistics from the LES, a modified Rotta closure for the pressure gradient-potential temperature covariance term (P) (Eq. (4.12)), and the singularity in the timescale (and hence in K_H) that was also noted by Wyngaard and Weil (1991) are first examined. The contribution of the local and nonlocal terms to the total heat flux in Eq. (4.13) is then presented, followed by an evaluation of the down-gradient diffusion closure to the flux transport term with various turbulent diffusivity profiles. Finally, the asymmetry in the (w, θ) scatter plot quantified by the quantity ΔF is investigated with the relative roles of the TOM in contributing to this asymmetry. The EDCG, TA, TOMP, and EDMF model parametrization are compared throughout.

4.4.1 The modified Rotta closure

Figure 4.6 shows a comparison between the LES output and the modeled pressure term (P). The latter uses the modified Rotta closure (MRC) in Eq. (4.12) with h/σ_w, $h/\sqrt{TKE}$, or h/w_* as relaxation timescales. The constants $C_1 = 3$, $C_2 = 1/2$, and $C_3 = 2/5$ are used. It is noticeable from Figure 4.6 that these timescales do not result in significant differences in the modeled profile of P, due to the fact that the Rotta term in Eq. (4.12) is small relative to the buoyancy and mean gradient counterparts. Figure 4.6 also shows that in both cases S1 and S10, the MRC reasonably reproduces the shape of the profile of P obtained from the LES. The return to isotropy timescale τ_1 obtained by rearranging Eq. (4.12) reads

$$\tau_1 = \frac{-C_1\overline{w\theta}}{P + C_2\beta\overline{\theta^2} - C_3\sigma_w^2(\mathrm{d}\Theta/\mathrm{d}z)}, \tag{4.25}$$

which shows that for $C_2 = C_3 = 0$, i.e. for a simple Rotta closure for the term P, τ_1 becomes negative in the regime of $\overline{w\theta} < 0$. This remains the case even when

including the buoyancy effects with $C_2 = 0.38$ (Deardorff, 1974) or $C_2 = 1/2$ (Moeng and Wyngaard, 1986), and the mean-gradient term with $C_3 = 2/5$. The fact that the numerator and denominator in Eq. (4.25) change sign at different heights and in opposite directions leads to an apparent singularity in τ_1 that was noted by Moeng and Wyngaard (1986) and Wyngaard and Weil (1991). This singularity was explained on the basis that bottom-up and top-down diffusion have different eddy-diffusivity profiles. However, these differences can be accommodated by adapting Eq. (4.25) to the negative flux portion of the CABL. Since the pressure term acts to decorrelate the vertical velocity and temperature, a change of sign of all the terms is required in the negative heat flux regime. This is equivalent to a downward-looking (top-down) perspective of the entrainment zone with a boundary condition $\overline{w\theta}_i \sim -0.2\overline{w\theta}_0$. Figure 4.7 shows the profiles of τ_1 calculated from the LES and Eq. (4.25). Acceptable agreement with the corresponding profiles obtained by Moeng and Wyngaard (1986) for the heat flux is noted here, but Eq. (4.25) avoids separating the boundary layer into top-down and bottom-up mechanisms. Further, it is noticeable from Eq. (4.25) that $\tau_1 \sim 0$ when $\overline{w\theta} \sim 0$, unless the denominator is identically zero at the same height and then τ_1 becomes indeterminate but still finite. The latter is the case in our LES runs, where the numerator and denominator approach zero at approximately the same height, i.e. with a difference less than $\Delta z/2$, where $\Delta z = 12.5$ m is the vertical resolution. Such difference can be attributed to numerical artifacts, especially that the term P is obtained here as a residual to the heat flux budget and thus incorporates all the uncertainties.

4.4.2 Local closure approach for the flux-transport term

As mentioned earlier, the model in Eq. (4.13) can be used to evaluate the local (first term) and nonlocal (last two terms) contributions to the total heat flux. First, the performance of this model in reproducing the heat flux obtained from the LES is

shown in the top panel of Figure 4.8. The vertical profile of the modeled flux (black line) is obtained using Eq. (4.13) with a relaxation timescale $\tau_1 = h/\sigma_w$, but other timescales such as $h/\sqrt{TKE}$, or h/w_* show comparable performance as noted in section 4.4.1. Since all the terms in Eq. (4.13) are obtained from the LES, except τ_1 and the constants, the deviations between modeled and LES fluxes are mostly due to the performance of the MRC (relaxation timescale τ_1). While this remains beyond the scope of this paper, it is important to consider height-dependent rather than constant values of C_2 and C_3 in Eq. (4.12) (see a recent paper by Heinze et al., 2016). The bottom panel of Figure 4.8 shows the contribution of each term in Eq. (4.13) to the total heat flux. The gradient diffusion term ($\propto \mathrm{d}\Theta/\mathrm{d}z$) becomes negative in the middle of the CABL, emphasizing the countergradient transport. It is noticeable that the sum of the nonlocal contributions to the heat flux, $\overline{w\theta}_{(NL)} = K_H\gamma$, exceeds their local counterpart in almost all of the CABL, and that the buoyancy and flux transport terms are comparable to each other.

The solution of Eq. (4.16) is shown in Figure 4.9 for simulations S1 and S10. Several profiles of the eddy diffusivity $K_T = \tau_2 q^2$ are tested. With $q^2 \propto \sigma_w^2$, the profiles of τ_2 are L_B/σ_w, $L_B/\sqrt{TKE}$, h/σ_w, and $h/\sqrt{TKE}$, where L_B is the Blackadar lengthscale defined by (Blackadar, 1962)

$$L_B = \frac{kz}{1 + kz/L_0}, \tag{4.26}$$

where $k \sim 0.4$ is the von Kármán constant and L_0 is an asymptotic value given by

$$L_0 = \frac{\alpha_b \int_0^h qz\mathrm{d}z}{\int_0^h q\mathrm{d}z}, \tag{4.27}$$

with $\alpha_b = 0.1$ (Mellor and Yamada, 1974), and $q = \sigma_w$ here. Figure 4.9 shows that the CABL height h performs relatively better than L_B as a lengthscale for the

profile of K_T, particularly in the strongly convective case S1. An eddy-diffusivity with the Blackadar lengthscale underestimates the heat flux in the bottom of the CABL, but performs comparably well to that with h as a lengthscale in the upper half as L_B approaches L_0. The timescale $\tau_2 = h/\sigma_w$, which is equivalent to the Lagrangian timescale T_L used by Wyngaard and Weil (1991), seems to perform best with $q^2 = \sigma_w^2$. Using $q^2 = TKE$ did not result in significant differences (not shown).

4.4.3 Transport asymmetry and the ejection-sweep events

The results of the quadrant analysis of the (w, θ) events are shown in Figure 4.10 for the end-member cases S1 and S10. This conditional sampling technique represents the average number of events of (w, θ) jointly occurring in a quadrant i. The averaging time here is 4 hours and the sampling is conducted at each height (layer) of the CABL. Note that the quantity F_i in Eq. (4.20) has a singularity when $\overline{w\theta} \sim 0$, and hence the top panel of Figure 4.10 shows the contribution $\langle w\theta \rangle_i = F_i \overline{w\theta}$ of each quadrant to the total heat flux. Quadrant **I** is associated with rising warm air (ejections) due to positive buoyancy and clearly has the largest contribution to the positive heat flux. Nevertheless, the contribution of subsiding cold air parcels in quadrant **III** (sweeps) to this positive flux is not negligible. Near the top of the boundary layer, quadrants **II** (entrained warm air) and **IV** (rising cold air) have more pronounced contributions to the heat flux. An important perspective that this analysis emphasizes is the fact that the updrafts in EDMF models and/or bottom-up diffusion in TA models can carry negative temperature fluctuations upward (quadrant **IV**), and that downdrafts (top-down) can transport positive temperature fluctuations downward (quadrant **II**). It is also noticeable that in the lower part of the CABL, where $\overline{w\theta} > 0$, quadrants **II** and **IV** still contribute to the heat flux, and hence account for the effects of top-down diffusion over the entire depth of the boundary layer. The same applies for quadrants **I** and **III** in the negative heat flux portion (upper 20% of

the CABL) , which indicates that the updrafts/downdrafts and bottom-up/top-down mechanisms are not decoupled in their contribution to the net heat flux. Quadrant analysis can then be perceived as a more general framework for examining these individual mechanisms. The bottom panel of Figure 4.10 shows the imbalance between the contributions of ejections and sweeps to the heat flux, i.e. quadrants **I** and **III** when $\overline{w\theta} > 0$ and quadrants **II** and **IV** when $\overline{w\theta} < 0$. Note that the quantity ΔF in Eq. (4.22) does not have a singularity when $\overline{w\theta} \sim 0$, since sweeps and ejections balance at the same height and hence the numerator becomes zero. For illustration purposes, the quantity plotted in Figure 4.10 is $\Delta F_0 = R\Delta F$, where R is the correlation coefficient. This quantity is negative in most of the CABL, indicating that ejections are dominant over sweeping events for the positive heat flux regime. When ΔF_0 becomes positive near the top, R switches sign and quadrant **II** contributes more to the downward heat flux than quadrant **IV**. This asymmetry in heat transport between the different quadrants becomes stronger with increasing w_*/u_*, where case S1 shows the highest absolute value of ΔF_0.

Connections between the asymmetry and the TOM can be achieved through Eq. (4.23). This truncation at third-order of $J(w, \theta)$ appears sufficient to capture the asymmetry quantified by quadrant analysis of ΔF_0 (Figure 4.11). While the expansion in Eq. (4.23) slightly underestimates the magnitude of ΔF_0 (Figure 4.11), it reproduces the overall profile reasonably, and although this asymmetry increases with stronger convection (red lines in Figure 4.11), ΔF_0 seems to attain a 'self-similar' shape with increasing w_*/u_*. Note that ΔF (and ΔF_0) are bounded between -1 (pure ejection flow) and $+1$ (pure sweeping flow). Nevertheless, despite being comprehensive, Eq. (4.23) remains taxing since it involves the correlation coefficient R and the four TOM (M_{jk}) that require parametrization. Katul et al. (1997a) and later Cava et al. (2006) noted that the first term in this cumulant expansion [$\propto(M_{03} - M_{30})$] may be small compared to the contribution of the mixed moments.

The same analysis is repeated here in Figure 4.12, which indicates that the ejection-sweep events and the transport asymmetry are mostly due to the fact that the turbulence transports heat flux and air temperature variance differently. The right panel of Figure 4.12 shows a comparison of the quantity ΔF_0 calculated from the full expansion in Eq. (4.23) and from the mixed moment term $[(1/2\sqrt{2\pi})(M_{21} - M_{12})]$ only. Furthermore, it is interesting to note that this latter result would appear in its exact form if the TOM parametrization in Eqs (4.7) and (4.8) by Abdella and McFarlane (1997) (with the correction by Mironov et al. (1999)), namely $M_{03} = S_w = \overline{ww\theta}/(\sigma_w\overline{w\theta})$ and $M_{30} = S_\theta = \overline{w\theta\theta}/(\sigma_\theta\overline{w\theta})$, are substituted in Eq. (4.23). After some rearrangement, and ignoring the contribution of the difference in skewness term ($\propto M_{03} - M_{30}$), Eq. (4.23) can be written as

$$\overline{ww\theta} = \frac{\sigma_w}{\sigma_\theta}\overline{w\theta\theta} - 2\sqrt{2\pi}\sigma_w\Delta F\overline{w\theta}, \tag{4.28}$$

and using Eq. (4.8), the flux transport term then reads

$$\frac{\mathrm{d}\overline{ww\theta}}{\mathrm{d}z} = \frac{\mathrm{d}}{\mathrm{d}z}(S_{(w,\theta)}\sigma_w\overline{w\theta}) - 2\sqrt{2\pi}\frac{\mathrm{d}}{\mathrm{d}z}(\sigma_w\Delta F\overline{w\theta}), \tag{4.29}$$

where $S_{(w,\theta)}$ can be S_w as originally suggested by Abdella and McFarlane (1997) in Eq. (4.8), or S_θ after Mironov et al. (1999). Recall that the first term on the rhs of Eq. (4.29), if S_w is used for $S_{(w,\theta)}$, is equal to $\mathrm{d}\overline{ww\theta}/\mathrm{d}z$ from Eq. (4.7), and hence the model by Abdella and McFarlane (1997) is equivalent to an approximation for the JPDF such that $\Delta F = 0$ when $\overline{w\theta} \neq 0$. An equally important note is a comparison with the model of nonlocal flux ($\overline{w\theta}_{(NL)}$) by Wyngaard and Weil (1991) in Eq. (4.6). This model can be recovered from Eq. (4.29) by setting $\Delta F = 0$, and S_w and σ_w as constants which was assumed by Wyngaard and Weil (1991). The flux transport term appears in the flux budget as $(C_3 - 1)\tau_1/C_1\mathrm{d}\overline{ww\theta}/\mathrm{d}z$, and hence $\tau_1 = T_L = h/\sigma_w$ here. Next, we consider the relation between the mixed TOM,

$\overline{w\theta\theta} = C(z)\overline{ww\theta}$, where $C(z)$ is not constant. For instance, $C(z) = \sigma_\theta/\sigma_w$ in the parametrization of Abdella and McFarlane (1997), which would lead to $\Delta F = 0$ in Eq. (4.28), and $C(z) = S_\theta\sigma_\theta/S_w\sigma_w$ with the correction of Mironov et al. (1999). Introducing $B(z) = 1 - C(z)\sigma_w/\sigma_\theta$, Eq. (4.28) can now be written as

$$\overline{ww\theta} = -\frac{2\sqrt{2\pi}}{B(z)}\sigma_w \Delta F \overline{w\theta}, \tag{4.30}$$

which defines an alternative parametrization for the turbulent flux of heat flux that explicitly encodes the role of ejections and sweeps in the heat flux budget. While Eq. (4.30) serves no prognostic purpose since the profile of ΔF is not known a priori (but is not zero), it remains useful in diagnosing the failure of the conventional gradient-diffusion model and in incorporating the role of large-scale motion in contributing to the sensible heat flux. If the representation of $\overline{ww\theta}$ in Eq. (4.30) and its downgradient-diffusion counterpart in Eq. (4.15) are compared, the quantity ΔF can be expressed as

$$\Delta F = \frac{h(\mathrm{d}\overline{w\theta}/\mathrm{d}z)B(z)}{2(\sqrt{2\pi})\overline{w\theta}}, \tag{4.31}$$

where $\tau_2 = h/\sigma_w$ and $q^2 = \sigma_w^2$ are used as noted earlier. By analogy with Eq. (4.22), and since h and $\mathrm{d}\overline{w\theta}/\mathrm{d}z$ are constant, Eq. (4.31) shows that the imbalance $\langle w\theta\rangle_{\text{sweeps}} - \langle w\theta\rangle_{\text{ejections}}$ scales with $B(z)$, i.e. the asymmetry in temperature variance and flux transport mechanisms. While this conclusion has been alluded to earlier by ignoring the skewness term and retaining the term $\propto(M_{21} - M_{12})$ (see Eq. (4.28)), the latter comparison in Eq. (4.31) represents an independent confirmation of this result. With the parametrization in Eq. (4.30), the heat flux budget in Eq. (4.13) can be written as a first-order differential equation of the form

$$A_1(z)\frac{\mathrm{d}\overline{w\theta}}{\mathrm{d}z} + A_2(z)\overline{w\theta} = A_3(z), \tag{4.32}$$

where

$$A_1(z) = \frac{2\sqrt{2\pi}}{C_1}\frac{\sigma_w}{B(z)}\Delta F,$$

$$A_2(z) = \frac{2\sqrt{2\pi}}{C_1}\frac{\mathrm{d}}{\mathrm{d}z}\left(\frac{\sigma_w \Delta F}{B(z)}\right) - \frac{1}{\tau_1},$$

$$A_3(z) = \frac{C_3 - 1}{C_1}\sigma_w^2\frac{\mathrm{d}\Theta}{\mathrm{d}z} + \frac{1 - C_2}{C_1}\beta\overline{\theta^2},$$

which has the general solution

$$\overline{w\theta} = \frac{\displaystyle\int_0^z \frac{A_3(z)}{A_1(z)} \exp\left(\int_0^z \frac{A_2(z)}{A_1(z)}\mathrm{d}z\right)\mathrm{d}z}{\displaystyle\exp\left(\int_0^z \frac{A_2(z)}{A_1(z)}\mathrm{d}z\right)} + C_I, \tag{4.33}$$

where C_I is an integration constant set by the boundary condition $(\overline{w\theta})_{z=0} = \overline{w\theta}_0$. To explore the characteristics of this solution, consider the case where A_2/A_1 and A_3/A_1 are nonzero constants, which also implies that A_2 and A_3 are related by a constant. This is equivalent to assuming that the quantity $\overline{ww\theta}/\overline{w\theta} \sim \sigma_w \Delta F/B(z)$ and its gradient that appears in A_2 scale with the mean gradient (M) and the buoyancy (B) terms in A_3, which can be seen in the flux budget Eq. (4.11) with the MRC for the pressure term. The general solution in Eq. (4.33) then becomes

$$\overline{w\theta} = \frac{A_3}{A_2}\left(1 - \exp\left(-\frac{A_2}{A_1}z\right)\right) + C_I, \tag{4.34}$$

such that as $z \to \infty$ (e.g. $z \to h$), $\overline{w\theta} \to A_3/A_2 + \overline{w\theta}_0$, and hence the ratio A_3/A_2 dictates the boundary condition at ∞ (entrainment flux). If we expand the exponential term in a Taylor series and rearrange Eq. (4.34), the solution is given by

$$\overline{w\theta} = (\frac{A_3}{A_1}z - \frac{A_2 A_3}{A_1^2}\frac{z^2}{2} + \dots) + \overline{w\theta}_0, \tag{4.35}$$

and hence for a linear flux profile, i.e. truncating the expansion at first-order, the ratio $A_3/A_1 < 0$ sets the slope of $\overline{w\theta}$. Recall that we initially assumed that A_3/A_1 is a nonzero constant. Since $(\overline{w\theta})_{z=h} = \overline{w\theta}_i$, it also follows that

$$\frac{A_3}{A_1} = \frac{\overline{w\theta}_i - \overline{w\theta}_0}{h}, \tag{4.36}$$

which shows that the entrainment flux is related to the asymmetry between ejections and sweeps. Explicit connections between EDMF models and the JPDF are considered next.

4.4.4 Analogy between EDMF models and the relaxed eddy accumulation method

The convective mass flux term in EDMF models, equivalent to $\overline{w\theta}_{(NL)} = M(\Theta_u - \Theta)$ in Eq. (4.10), where $M = a_u(w_u - \overline{w})$, appears to bear some similarity with the relaxed eddy accumulation (REA) method used in scalar flux measurements near the surface (e.g. Businger and Oncley, 1990; Katul, 1994). The REA relies on conditional sampling of updrafts (rising air parcels) and downdrafts (subsiding parcels) to estimate a scalar flux as

$$\overline{w\theta} = b\sigma_w \left(\Theta_+ - \Theta_-\right), \tag{4.37}$$

where the potential temperature fluctuations are used as the scalar of interest here, $b \sim$ 0.52-0.62 (Katul et al., 1996) is a proportionality constant, and Θ_+ (equivalent to Θ_u) and Θ_- (equivalent to Θ_e) are the mean temperatures in the updrafts and downdrafts respectively. Recall that $\Theta = \Theta_e$ and $\overline{w} = w_e$ in the EDMF are only approximations to the fact that the updrafts occupy a narrow area and are surrounded by a slowly subsiding environment, and hence by analogy the mass flux $M \sim b\sigma_w$. This was also noted by Wyngaard and Moeng (1992), and in another context, Siebesma et al. (2007) used the approximation $b \approx 0.3$. Starting with a

Gaussian JPDF of θ/σ_θ and w/σ_w, with the normalized temperature and vertical velocity plotted on the y- and x-axis respectively (see Figure 4.2), then the correlation coefficient can be approximated by

$$R = \frac{(\Theta_+ - \Theta_-)/\sigma_\theta}{(w_+ - w_-)/\sigma_w}, \tag{4.38}$$

where $w_+ = w_u$ and $w_- = w_e$ are the mean vertical velocity components in the updrafts and downdrafts respectively. Using $\overline{w\theta} = R\sigma_w\sigma_\theta$, the heat flux is given by

$$\overline{w\theta} = \frac{\sigma_w}{w_+ - w_-}\sigma_w \left(\Theta_+ - \Theta_-\right), \tag{4.39}$$

and by analogy to Eq. (4.37), the coefficient b is given as

$$b = \frac{\sigma_w}{w_+ - w_-}. \tag{4.40}$$

These relations originally developed by Baker et al. (1992) are used in many contexts. With this assumption, the mass flux is

$$M = a_u \left(w_+ - w_-\right) = \frac{\sigma_w}{w_+ - w_-}\sigma_w, \tag{4.41}$$

and hence the fractional area occupied by the updrafts scales as $a_u \sim b^2$. This area is 0.09 for the value $b = 0.3$ used by Siebesma et al. (2007) and ranges between 0.27-0.38 for the usual values of b ($\sim$ 0.52-0.62). Hence, it can be surmised that the EDMF models are based on a quasi-Gaussian approximation to the JPDF for the normalized θ/σ_θ and w/σ_w or equivalently, setting $\Delta F_0 = 0$.

4.5 Conclusions

Various models that correct downgradient-diffusion approximations in the convective atmospheric boundary layer (CABL) employ a countergradient (EDCG), transport asymmetry (TA), third-order moment parametrization (TOMP), or a mass flux

(EDMF) approach. Reconciling such models and unfolding their similarities has resisted complete theoretical treatment. Using LES runs for the CABL, the role of the turbulent flux transport term and its contribution to the sensible heat flux budget was examined, which revealed that the third-order moments do shape such nonlocal effects. First, a modified Rotta closure for the pressure gradient-potential temperature term and a downgradient-diffusion approach for closing the flux transport term were evaluated with a variety of closure time- and length- scales. The analysis indicates that the height of the CABL and the vertical velocity variance are acceptable closure length and velocity scales. Second, a diagnostic framework that reveals the role of the third-order moments in shaping the asymmetry in vertical diffusion of scalars in the CABL was developed and characterized. This framework relies on conditional sampling and quadrant analysis of the JPDF of vertical velocity and potential temperature, which is indicative of the contributions of each quadrant and physical flow mechanism to the total heat flux. The imbalance between these quadrants is tied to ejections and sweeps in the flow field and was expanded in terms of the third-order moments of the Gram-Charlier expansion of the JPDF. The EDCG, TA, TOMP, and EDMF models were linked to different approximations of the JPDF, particularly to assumptions on the asymmetry and imbalance between ejections and sweeps. This imbalance is mostly due to the mixed moments rather than the skewness. For instance, the EDCG model that parametrizes the third moments in terms of bulk properties of the CABL can be viewed as an integrated approach of such asymmetry. Both TA and TOMP models were retrieved by neglecting the quantity ΔF_0, the imbalance between ejections and sweeps, and assuming height-independent vertical profiles of the skewness and variance of vertical velocity. The EDMF model was shown to follow from a Gaussian approximation for the JPDF in line with REA methods. An interesting connection between the coefficient b in REA and the fractional area a_u occupied by the updrafts suggested that the latter is not necessarily

negligible as assumed by EDMF models. This may indicate that the neglected term $a_u\overline{w\theta}^u$ may still be important, and together with the term $(1-a_u)\overline{w\theta}^e$, they are responsible for local fluxes in the updrafts and the surrounding environment respectively, with eddy diffusivities weighted by the fractional area a_u. Finally, the LES runs suggest that the ΔF_0 profiles appear to reach a self-similar shape (depends only on z/h) offering a possibility for a novel closure model for the heat flux budget in the CABL.

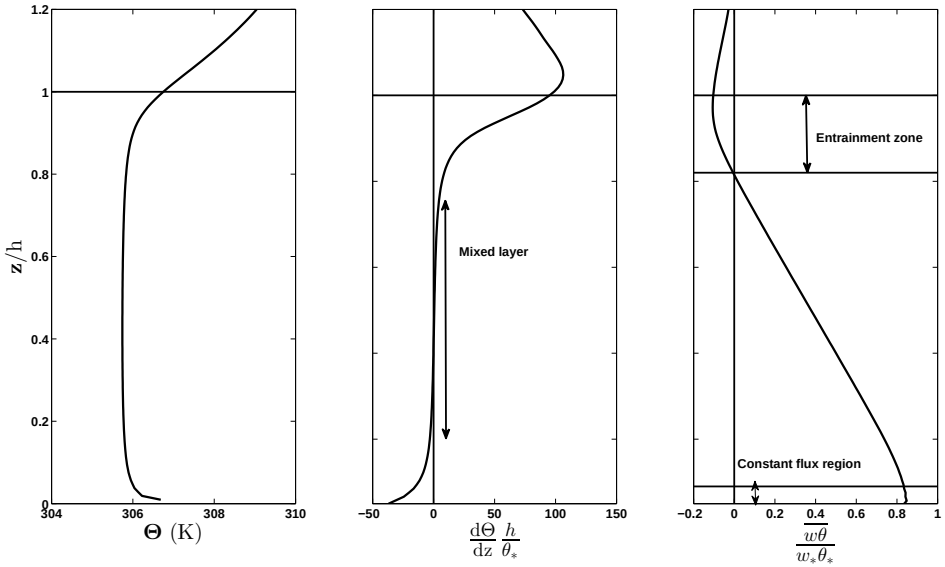

FIGURE 4.1: Typical profiles of mean potential temperature Θ (K) (left), its vertical gradient ($\mathrm{d}\Theta/\mathrm{d}z$) normalized by θ_*/h (middle), and the heat flux normalized by $w_*\theta_*$ (right). The scaling constants h, $w_* = (\beta\overline{w\theta}_0 h)^{1/3}$ and $\theta_* = \overline{w\theta}_0/w_*$ are the boundary layer height, Deardorff convective velocity and temperature scales respectively. Note the zero-gradient heat flux in the mixed layer that cannot be explained by gradient-diffusion. The surface layer with constant flux ($\mathrm{d}\overline{w\theta}/\mathrm{d}z \approx 0$) and the entrainment zone ($\overline{w\theta} < 0$) are also shown.

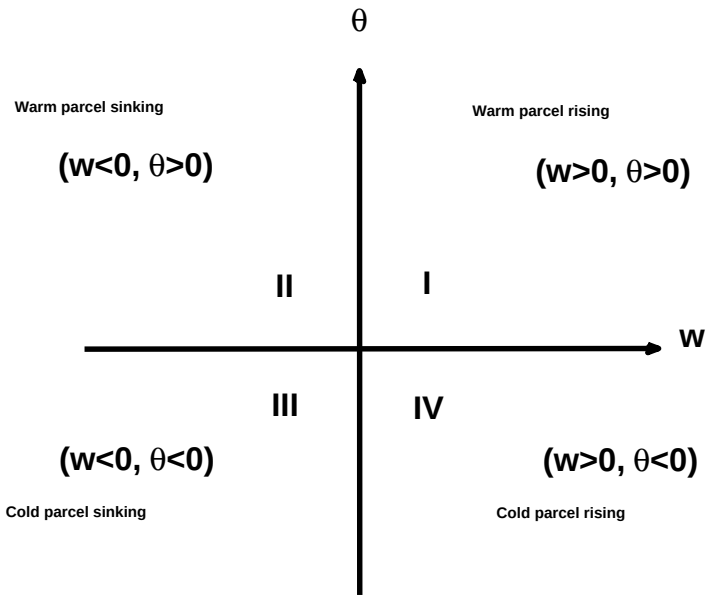

FIGURE 4.2: Nomenclature for conditional sampling of the w-θ events. Quadrants **I** and **III** contribute to positive (upward) heat fluxes while quadrants **II** and **IV** contribute to negative (downward) fluxes. In the region where the net heat flux is positive (lower $\approx$ 80% of the CABL), quadrants **I** and **III** are defined here as ejection and sweep events respectively. Quadrants **II** and **IV** correspond to ejection and sweep events in the negative net heat flux region (upper $\approx$ 20% of the CABL).

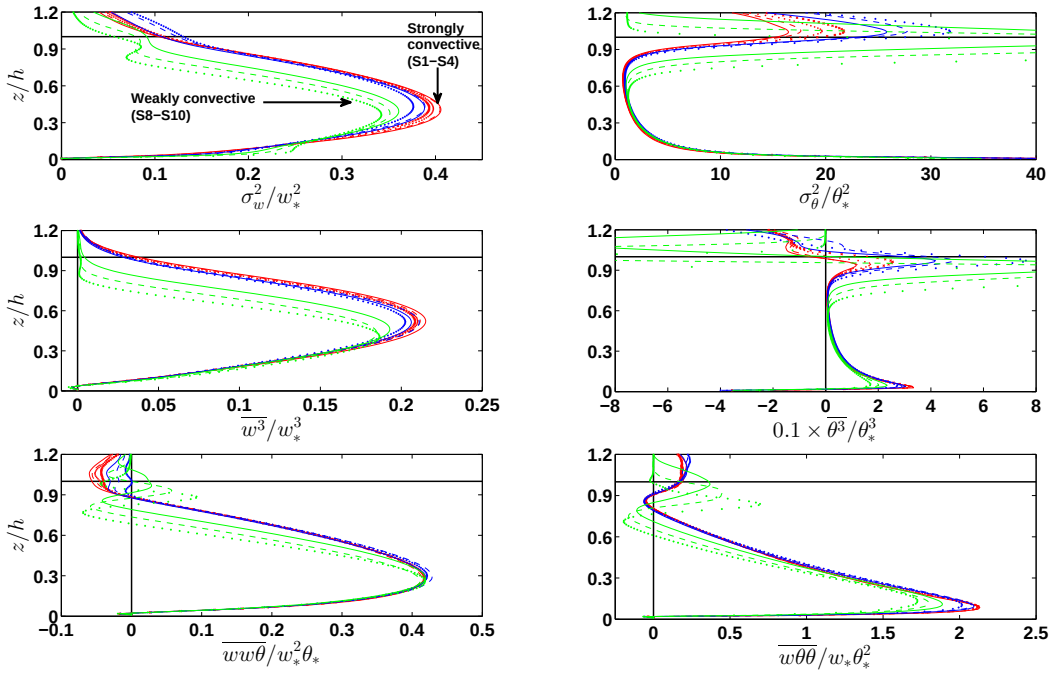

FIGURE 4.3: Vertical profiles for the second and third-order moments of vertical velocity and potential temperature for the ten LES runs. The profiles are normalized by the appropriate combination of convective velocity (w_*) and temperature (θ_*) scales, where θ_* is defined by the relation $w_*\theta_* = \overline{w\theta}_0$. The red color indicates the strongly convective cases (S1-S4), blue color for moderately convective (S5-S7), and green color for weakly convective (S8-S10). See Table 4.1 for details of the simulations. The horizontal black line corresponds to $z/h = 1$.

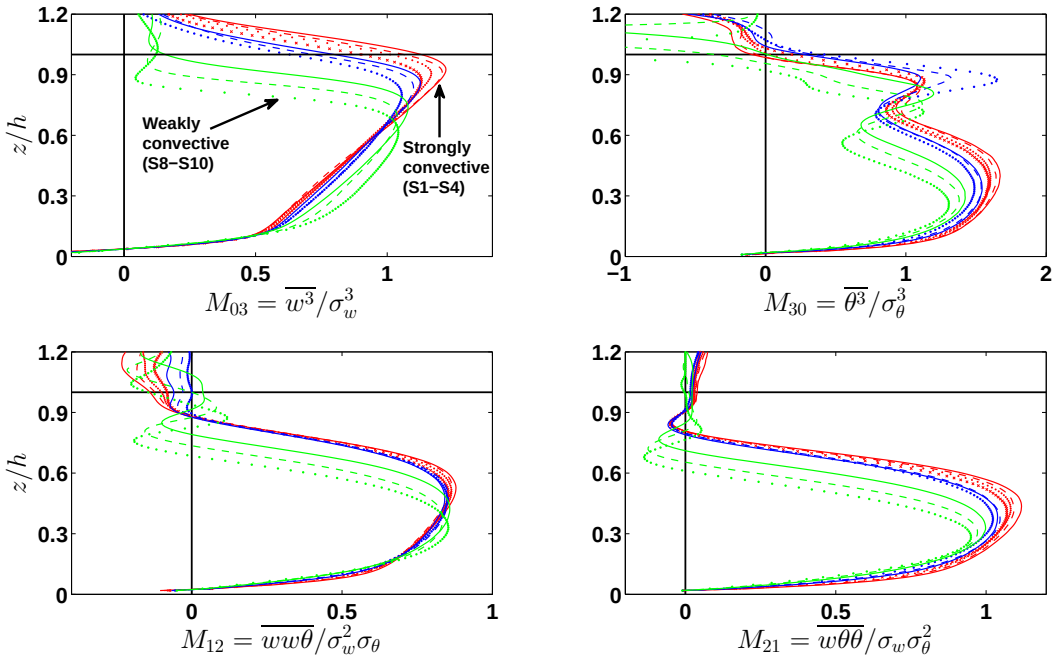

FIGURE 4.4: Same as Figure 4.3 but normalized by the standard deviations σ_w and σ_θ to show the moments M_{jk}. The red color indicates the strongly convective simulations (S1-S4), blue color for moderately convective (S5-S7), and green color for weakly convective (S8-S10).

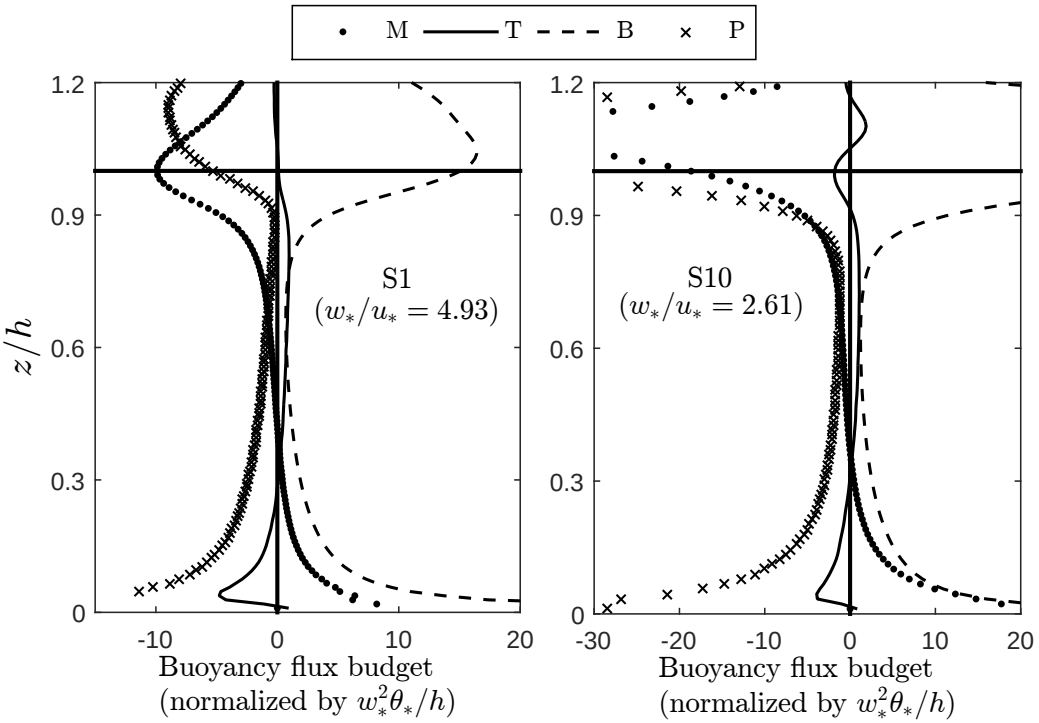

FIGURE 4.5: The heat flux budget terms in Eq. (4.11) normalized by the convective velocity and temperature scales and the boundary layer height. The simulations with highest (S1) and lowest (S10) ratio of w_*/u_* are shown for illustration. These simulations are described in Table 4.1.

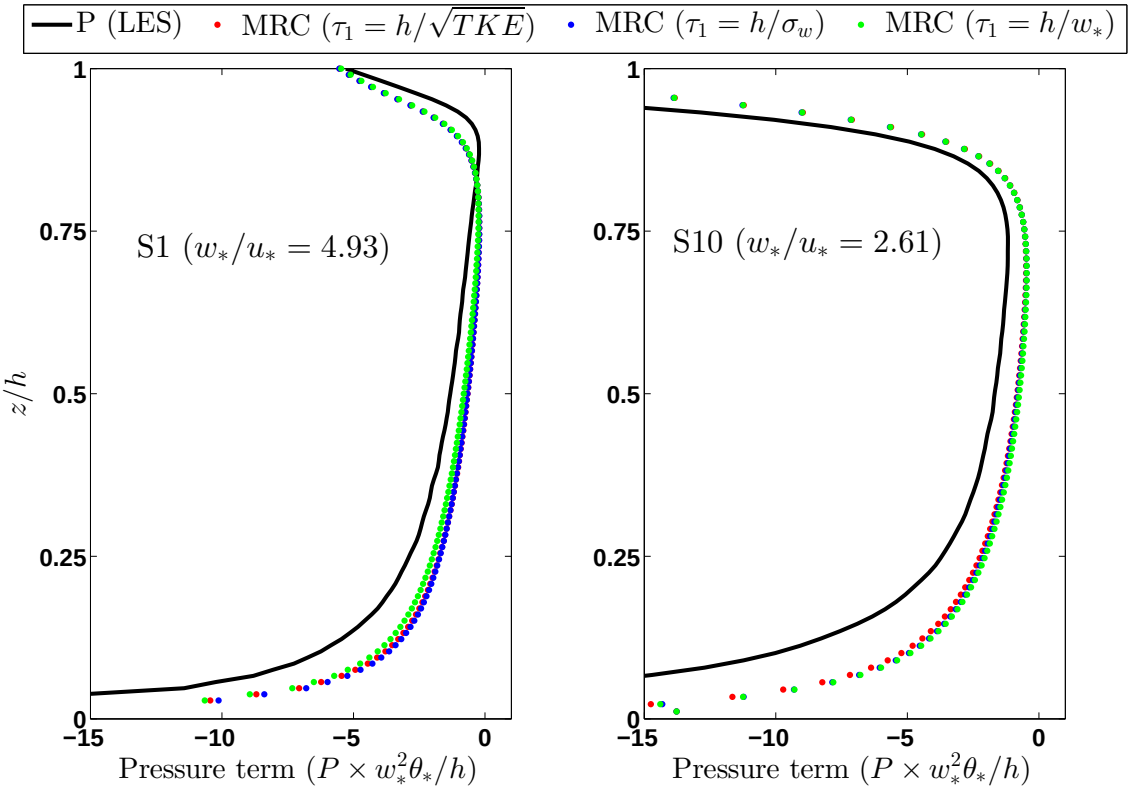

FIGURE 4.6: The modified Rotta closure (MRC) model for the pressure gradient-temperature covariance term (P) from Eq. (4.12) with several profiles of the timescale τ_1. The black line represents the term (P) obtained as a residual to the heat flux budget (Eq. (4.11)) from the LES runs.

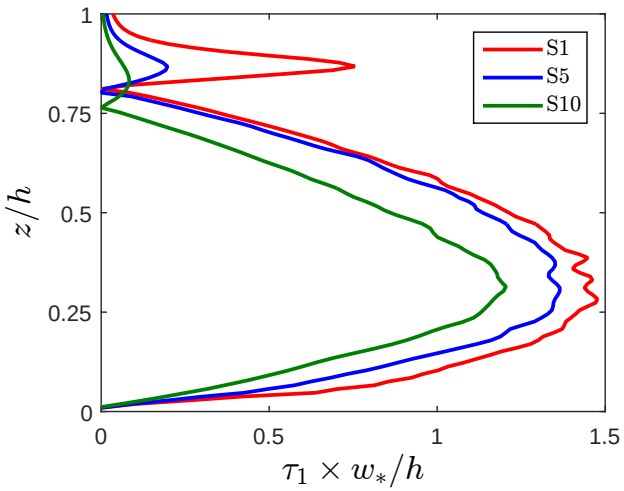

FIGURE 4.7: The return to isotropy timescale normalized by the large-eddy turnover timescale (h/w_*) and calculated from the LES profiles (Eq. (4.25)) for simulations S1, S5, and S10.

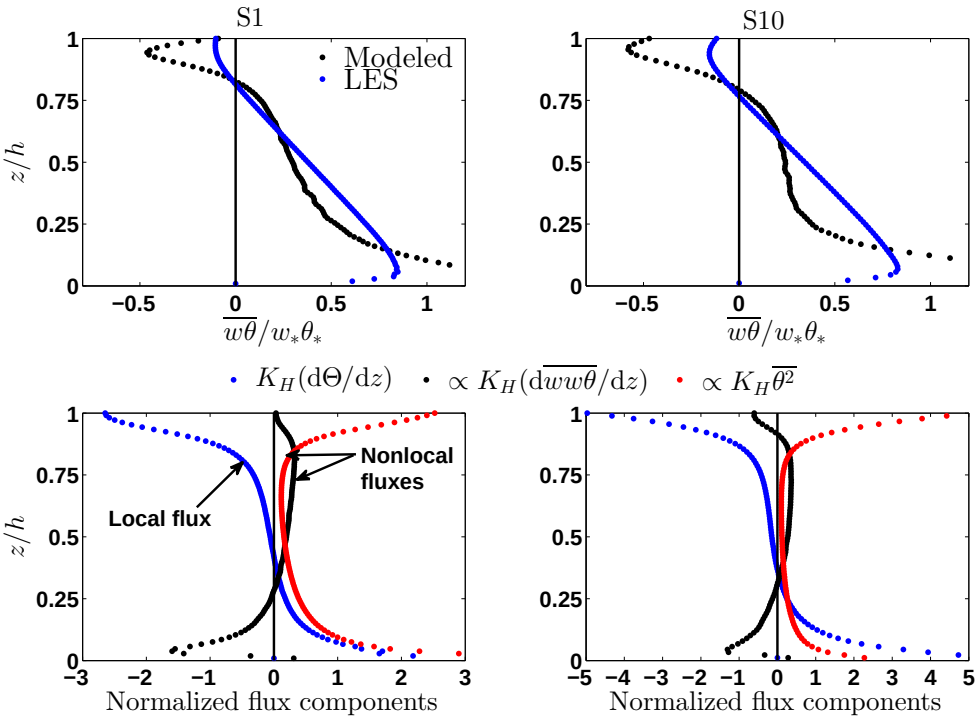

FIGURE 4.8: Top: Comparison of the heat flux profiles obtained from the LES output (blue dots) and from the model in Eq. (4.13) with $\tau_1 = h/\sigma_w$ (black dots). Bottom: The contribution of each term (normalized by $w_*\theta_*$) in Eq. (4.13) to the modeled heat flux. Left and right columns are for simulations S1 and S10 respectively.

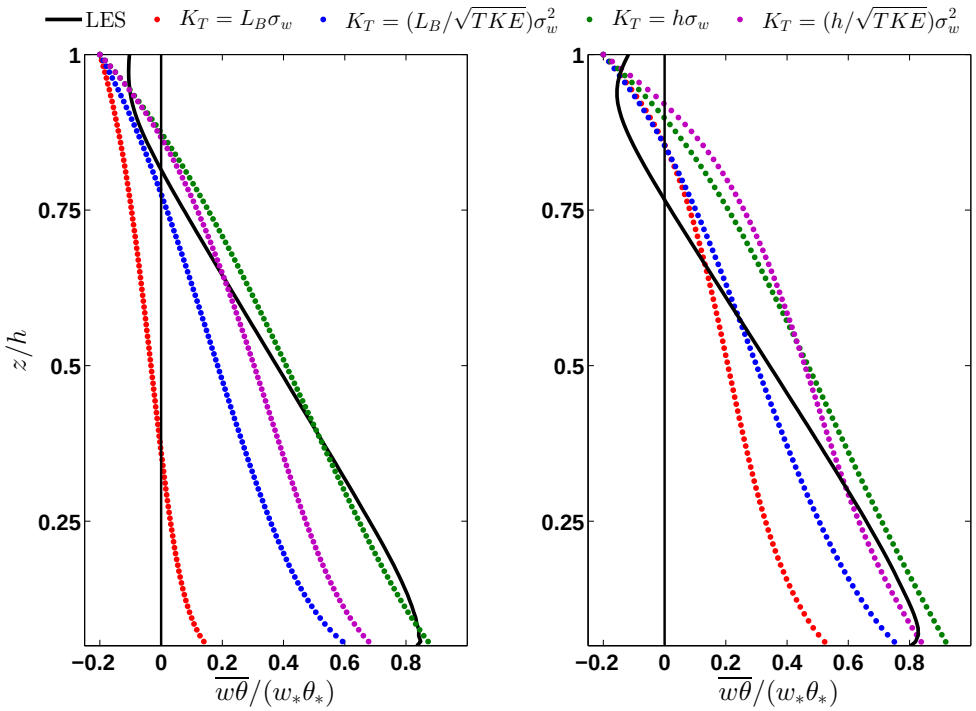

FIGURE 4.9: Comparison of the modeled heat flux profiles (normalized by surface heat flux) using Eq. (4.16) with the LES output (black line). The modeled profiles (red, blue, green, and magenta dots) are obtained using different eddy-diffusivity (K_T) profiles in Eq. (4.16) (see legend). L_B is the Blackadar lengthscale (see text). Left and right panels are for simulations S1 and S10 respectively.

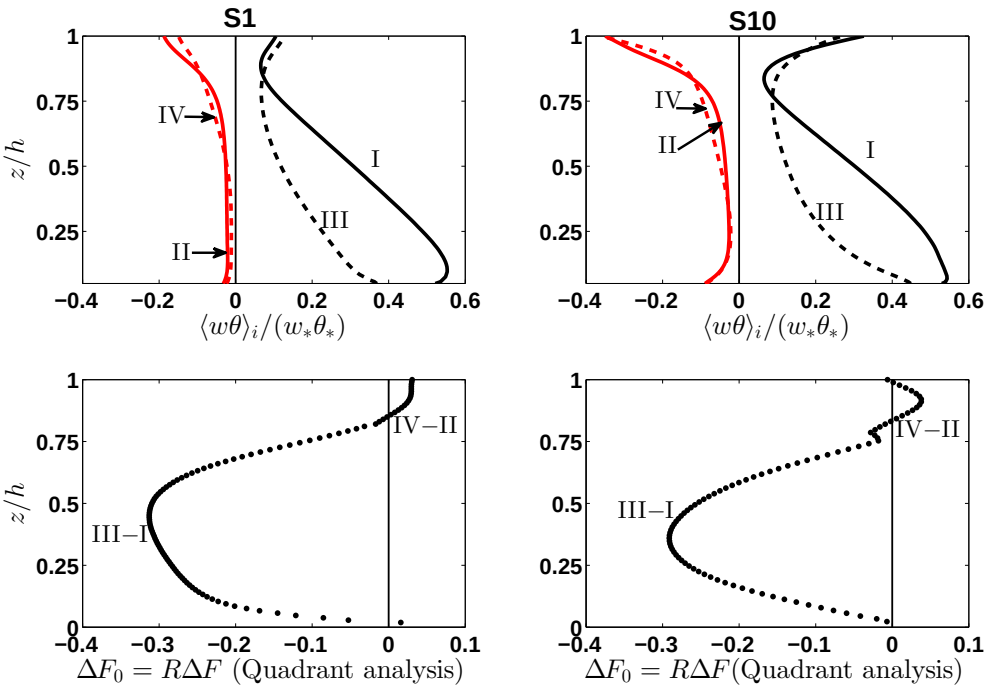

FIGURE 4.10: Conditional sampling and quadrant analysis of the (w, θ) scatter plot from the LES output. Top: The fractional contributions $\langle w\theta \rangle_i$ of each quadrant (i =**I**, **II**, **III**, and **IV**) to the total heat flux (see Figure 4.2 for definition of quadrants). Bottom: The imbalance in these contributions quantified by $\Delta F_0 = R\Delta F$ (see text in section 4.4.3). Left and right columns are for simulations S1 and S10 respectively.

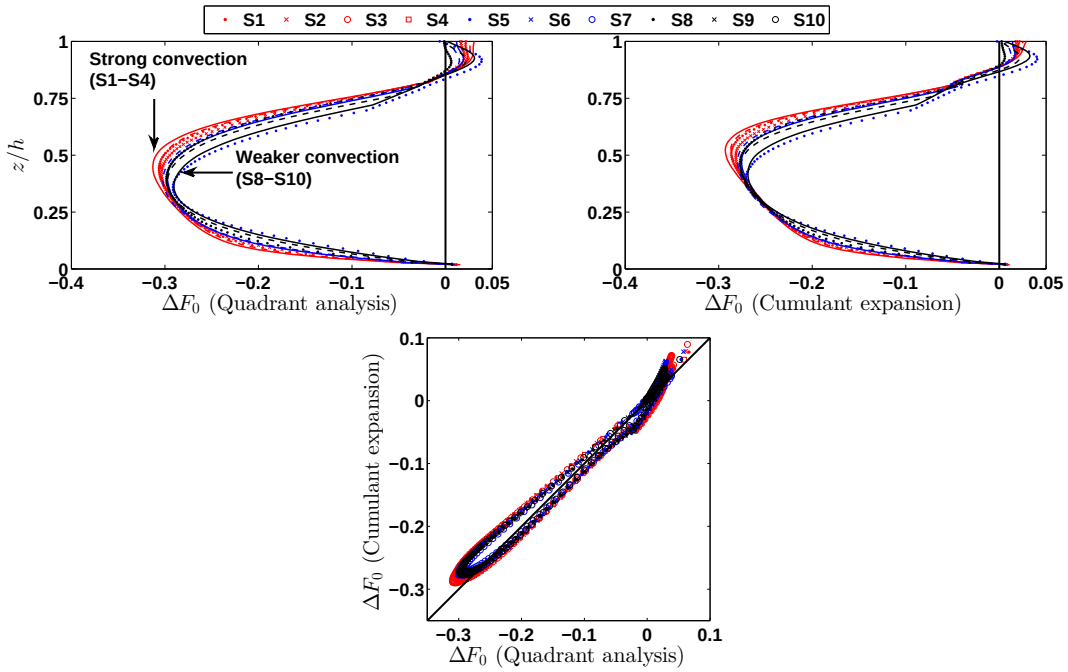

FIGURE 4.11: Comparison of the quantity ΔF_0 from conditional sampling (quadrant analysis) (top left) and the cumulant expansion in Eq. (4.23) (top right). Red colors are for simulations S1 to S4, blue colors for S5-S7, and black colors for S8-S10. The 1:1 line (black color) in the bottom figure is shown for reference.

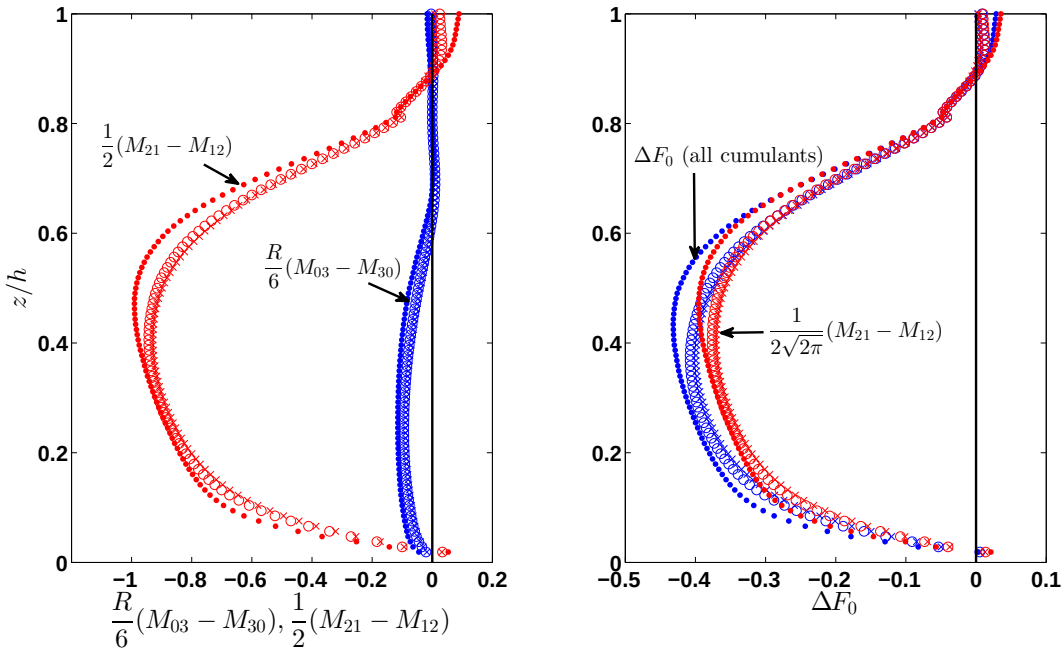

FIGURE 4.12: Left: The relative contribution of the two terms in Eq. (4.23): $\frac{R}{6}(M_{03}-M_{30})$ (blue color) and $\frac{1}{2}(M_{21}-M_{12})$ (red color) to the quantity $\Delta F_0 = R\Delta F$. Right: The quantity ΔF_0 calculated using all the cumulants (full equation) in Eq. (4.23) (blue color) and from the mixed moments term only ($\frac{1}{2\sqrt{2\pi}}(M_{21} - M_{12})$) (red color). The individual symbols are for S1 ($\cdot$), S5 ($\circ$), and S10 (x).

Table 4.1: Properties of the numerical simulations.

Parameter	U_g m s^{-1}	$\overline{w\theta}_0$ K m s^{-1}	h m	$\lvert L\rvert$ m	$-h/L$ -	u_* m s^{-1}	w_* m s^{-1}	w_*/u_* -
S1	9	0.24	1238	25.3	48.9	0.43	2.12	4.93
S2	10	0.24	1238	31.3	39.5	0.46	2.12	4.60
S3	11	0.24	1238	38.6	32.1	0.50	2.12	4.30
S4	12	0.24	1238	46.1	26.8	0.53	2.12	4.04
S5	13	0.24	1238	54.6	22.4	0.56	2.12	3.80
S6	14	0.24	1238	64.0	19.3	0.59	2.12	3.62
S7	15	0.24	1238	73.8	16.8	0.61	2.12	3.45
S8	15	0.18	1163	91.8	12.7	0.60	1.89	3.15
S9	15	0.14	1113	113.9	9.8	0.59	1.71	2.89
S10	15	0.10	1075	150.1	7.2	0.58	1.52	2.61

5

Conclusions and future directions

The structure and scaling laws of turbulence in the ABL are examined in a context that challenges the classical view of shear-dominated wall-bounded flows. As opposed to smooth or rough walls/surfaces in canonical turbulent boundary-layers, the land surface has two distinct aspects that can alter classical scaling laws. These are the existence of tall roughness elements (e.g. vegetation canopies) and the effects of surface heating (typically during daytime). In this context, the work here relied on laboratory experiments, field measurements, and numerical simulations to explore the effects of these two aspects on ABL flows. A summary of each chapter along with the findings is as follows

- **Chapter 1** provided the background and motivation for the dissertation, along with its intellectual merit and broader implications. The study of ABL flows is contextualized here as an integral component of biosphere-atmosphere interactions and climate change research, where the parametrization of such flows in coarse-scale numerical weather prediction and climate models requires knowledge of turbulence processes and dominant length scales that dictate energy and matter transport, mixing, and dissipation. This context set up the discussion into study-

ing various layers of the ABL encompassing the statistics of turbulence within and above the roughness elements (vegetation canopies here), and in the mixed-layer where the effects of buoyancy on large-eddy heat transport are important.

- **Chapter 2** addressed the issue of ergodicity of scalar statistics within canopies. It has been long-recognized that homogeneous and stationary turbulence is ergodic, but less is known about the effects of inhomogeneity introduced by the presence of canopies on the turbulence statistics. A high resolution (temporal and spatial) flume experiment with vertical stainless-steel rods mounted at the channel bottom mimicking a dense rigid canopy is used here. Dye was injected in the upstream water flow, illuminated with laser-induced fluorescence technique, and a sequence of planar (parallel to channel bottom) images were recorded to provide spatial (2D) and temporal statistics of the dye concentration. Operational ergodicity was defined here as the convergence of both temporal and spatial statistics to their ensemble counterpart. The findings indicate that within-canopy scalar statistics have a tendency to be ergodic, mostly in shallow layers (close to canopy top) where the sweeping flow events appear to randomize the statistics. Deeper layers within the canopy are dominated by low-dimensional (quasi-deterministic) von Kármán vortices that tend to break ergodicity.

- **Chapter 3** used five field and laboratory experiments to examine the existence of a logarithmic scaling in the structure function of the longitudinal ($D_{uu}(r)$) and vertical ($D_{ww}(r)$) velocity components. The experimental data sets spanned the roughness sub-layer (RSL) above vegetation canopies (two experiments), the atmospheric surface-layer (ASL) above a lake and a grass field (two experiments), and one open channel experiment. The findings indicate that both the k^{-1} scaling in E_{uu} and/or $\ln(r)$ in D_{uu} exist within the RSL, ASL, and canonical turbulent boundary layers, although the extent of this anisotropic range varies across ex-

periments, with the RSL exhibiting shorter extent due to the small separation of scales (the integral length scale is smaller than its ASL counterpart). Conversely, these scaling laws are absent in E_{ww} or D_{ww} for the vertical velocity components, except at large distances from the wall where a short extent of anisotropy emerges. Phenomenological aspects of the coherent eddies reveal that the statistics of velocity increments Δu and Δw approach a Gaussian-like behavior at large r. These findings are in broad agreement with the accepted picture of canonical turbulent boundary layers. Eddies associated with these large anisotropic r are further responsible for momentum/energy production corroborated by large positive (negative) excursions in Δu accompanied by negative (positive) ones in Δw. In terms of similarity, normalizing the separation distance r by the inertial length scale κz or l_ϵ shows comparable performance in collapsing the structure functions D_{uu} and D_{ww} at different heights in the ASL, where the ratio P/ϵ does not deviate appreciably from unity. In contrast, l_ϵ collapses these structure functions in the RSL better than z, albeit with some discrepancies at the larger scales.

- **Chapter 4** reconciled various closure schemes that correct for the failure of gradient-diffusion (K-theory) when modeling heat transport in the convective atmospheric boundary-layer (CABL). Using LES runs for the CABL, the role of the turbulent flux transport term in the second-order heat budget and its contribution to the sensible heat flux was examined, which revealed that the third-order moments do shape such nonlocal effects. First, a modified Rotta closure for the pressure gradient-potential temperature term and a downgradient-diffusion approach for closing the flux transport term were evaluated with a variety of closure time- and length- scales. The analysis indicates that the height of the CABL and the vertical velocity variance are acceptable closure length and velocity scales. Second, a diagnostic framework that reveals the role of the third-order moments in

shaping the asymmetry in vertical diffusion of scalars in the CABL was developed and characterized. This framework relies on conditional sampling and quadrant analysis of the joint probability density function (JPDF) of vertical velocity and potential temperature, which is indicative of the contributions of each quadrant and physical flow mechanism to the total heat flux. The imbalance between these quadrants is tied to ejections and sweeps in the flow field and was expanded in terms of the third-order moments of the Gram-Charlier expansion of the JPDF. The EDCG, TA, TOMP, and EDMF models were linked to different approximations of the JPDF, particularly to assumptions on the asymmetry and imbalance between ejections and sweeps.

The near-term future research directions build upon the findings above and will make use of the flume experiment to connect the scale-wise statistics of scalars within canopies to their scaling laws. In particular, the degree of organization or entropy of the spatial statistics at each scale, spanning the viscous, inertial, and large scale motion will be connected to their spectral scaling laws counterpart. These are functions of the flow field at each layer within the canopy, where the statistics at the canopy top are frequently affected by sweeping flow motion from above, while deeper layers tend to be dominated by von Kármán vortices. In addition, the role of stability/buoyancy in modifying the results of Chapter 3 will be addressed in a future study, with a focus on mildly-unstable to convective conditions.

The mid-range future research direction will rely on both closure models and large eddy simulations to address the concept of baroclinic ABL flows, i.e. when horizontal temperature gradients exist in the boundary layer under different stability conditions (mildly stable, near-neutral, and mildly unstable). This is in contrast to the typically assumed planar homogeneous ABL, and hence is important in contexts when transitions in land use (e.g. water-land interfaces) are encountered. The outcome

of this research is intended to serve an improved parametrization the ABL in numerical weather prediction models along with a refined representation of boundary layer turbulence in modeling scalar transport, shallow cloud formation, and aerosol deposition.

In the longer range, reducing the dimensionality and complexity of turbulent flows is warranted in natural settings such as the atmosphere. To find simpler representations of turbulence, both in its mean flow and statistics, concepts from classical thermodynamics (statistical mechanics) and perturbation theory can offer a promising starting point in deriving more robust laws. The notion that any dynamical system, when perturbed, tends to restore its equilibrium by following a trajectory in phase space that maximizes its entropy will be relied upon to infer some characteristics of turbulence, and compared to the well-studied scaling laws. This requires setting up models that use thermodynamic equations (that retain the continuum hypothesis) and entropy budgets in a simplified context, along with numerical simulations to verify/justify such simplifications.

Bibliography

Abdella, K. and McFarlane, N. (1997), "A new second-order turbulence closure scheme for the planetary boundary layer," J. Atmos. Sci., 54, 1850–1867.

Andrén, A. and Moeng, C.-H. (1993), "Single-point closures in a neutrally stratified boundary layer," J. Atmos. Sci., 50, 3366–3379.

Anselmet, F., Gagne, Y., Hopfinger, E., and Antonia, R. (1984), "High-order velocity structure functions in turbulent shear flows," J. Fluid Mech., 140, 63–89.

Antonia, R. (1981), "Conditional sampling in turbulence measurement," Annu. Rev. Fluid Mech., 13, 131–156.

Baker, J., Norman, J., and Bland, W. (1992), "Field-scale application of flux measurement by conditional sampling," Agr. Forest Meteorol., 62, 31–52.

Baldocchi, D. and Meyers, T. (1998), "On using eco-physiological, micrometeorological and biogeochemical theory to evaluate carbon dioxide, water vapor and trace gas fluxes over vegetation: a perspective," Agric. For. Meteorol., 90, 1–25.

Banerjee, T. and Katul, G. G. (2013), "Logarithmic scaling in the longitudinal velocity variance explained by a spectral budget," Phys. Fluids, 25, 125106.

Banerjee, T., Katul, G., Salesky, S., and Chamecki, M. (2015), "Revisiting the formulations for the longitudinal velocity variance in the unstable atmospheric surface layer," Quart. J. Roy. Meteor. Soc., 141, 1699–1711.

Blackadar, A. K. (1962), "The vertical distribution of wind and turbulent exchange in a neutral atmosphere," J. Geophys. Res., 67, 3095–3102.

Bogard, D. and Tiederman, W. (1987), "Characteristics of ejections in turbulent channel flow," J. Fluid Mech., 179, 1–19.

Bou-Zeid, E., Meneveau, C., and Parlange, M. (2005), "A scale-dependent Lagrangian dynamic model for large eddy simulation of complex turbulent flows," Phys. Fluids, 17, 025105.

Bou-Zeid, E., Vercauteren, N., Parlange, M. B., and Meneveau, C. (2008), "Scale dependence of subgrid-scale model coefficients: An a priori study," Phys. Fluids, 20, 115106.

Busch, N. E. and Panofsky, H. A. (1968), "Recent spectra of atmospheric turbulence," Quart. J. Roy. Meteor. Soc., 94, 132–148.

Businger, J. A. and Oncley, S. P. (1990), "Flux measurement with conditional sampling," J. Atmos. Ocean. Tech., 7, 349–352.

Canuto, V., Minotti, F., Ronchi, C., Ypma, R., and Zeman, O. (1994), "Second-order closure PBL model with new third-order moments: Comparison with LES data," J. Atmos. Sci., 51, 1605–1618.

Cava, D., Katul, G., Scrimieri, A., Poggi, D., Cescatti, A., and Giostra, U. (2006), "Buoyancy and the sensible heat flux budget within dense canopies," Boundary-Layer Meteorol., 118, 217–240.

Chamecki, M. and Dias, N. L. (2004), "The local isotropy hypothesis and the turbulent kinetic energy dissipation rate in the atmospheric surface layer," Quart. J. Roy. Meteor. Soc., 130, 2733–2752.

Chamecki, M., Dias, N. L., Salesky, S. T., and Pan, Y. (2017), "Scaling Laws for the Longitudinal Structure Function in the Atmospheric Surface Layer," J. Atmos. Sci., 74, 1127–1147.

Chen, J., Hu, Y., Yu, Y., and Lü, S. (2014), "Ergodicity test of the Eddy correlation method," Atmos. Chem. Phys. Discuss., 14, 18207âĂŞ18254, 2014, 14, 18207–18254.

Chung, D., Marusic, I., Monty, J., Vallikivi, M., and Smits, A. (2015), "On the universality of inertial energy in the log layer of turbulent boundary layer and pipe flows," Exp. Fluids, 56, 141.

Constantin, P., Glatt-Holtz, N., and Vicol, V. (2013), "Unique ergodicity for fractionally dissipated, stochastically forced 2D Euler equations," Comm. Math. Phys., pp. 1–39.

Cuijpers, J. and Holtslag, A. (1998), "Impact of skewness and nonlocal effects on scalar and buoyancy fluxes in convective boundary layers," J. Atmos. Sci., 55, 151–162.

DaPrato, G. and Debussche, A. (2003), "Ergodicity for the 3D stochastic Navier-Stokes equations," J. Math. Pures Appl., 82, 877âĂŞ947.

Davidson, P. and Krogstad, P.-Å. (2009), "A simple model for the streamwise fluctuations in the log-law region of a boundary layer," Phys. Fluids, 21, 055105.

Davidson, P. and Krogstad, P.-Å. (2014), "A universal scaling for low-order structure functions in the log-law region of smooth-and rough-wall boundary layers," J. Fluid Mech., 752, 140–156.

Davidson, P., Nickels, T., and Krogstad, P.-Å. (2006), "The logarithmic structure function law in wall-layer turbulence," J. Fluid Mech., 550, 51–60.

de Silva, C., Marusic, I., Woodcock, J., and Meneveau, C. (2015), "Scaling of second- and higher-order structure functions in turbulent boundary layers," J. Fluid Mech., 769, 654–686.

Deardorff, J. (1972), "Theoretical expression for the countergradient vertical heat flux," J. Geophys. Res., 77, 5900–5904.

Deardorff, J. W. (1966), "The counter-gradient heat flux in the lower atmosphere and in the laboratory," J. Atmos. Sci., 23, 503–506.

Deardorff, J. W. (1970), "Convective velocity and temperature scales for the unstable planetary boundary layer and for Rayleigh convection," J. Atmos. Sci., 27, 1211–1213.

Deardorff, J. W. (1974), "Three-dimensional numerical study of turbulence in an entraining mixed layer," Boundary-Layer Meteorol., 7, 199–226.

Del Alamo, J. C., Jiménez, J., Zandonade, P., and Moser, R. D. (2004), "Scaling of the energy spectra of turbulent channels," J. Fluid Mech., 500, 135–144.

Drobinski, P., Carlotti, P., Newsom, R. K., Banta, R. M., Foster, R. C., and Redelsperger, J.-L. (2004), "The structure of the near-neutral atmospheric surface layer," J. Atmos. Sci., 61, 699–714.

Drobinski, P., Carlotti, P., Redelsperger, J.-L., Masson, V., Banta, R. M., and Newsom, R. K. (2007), "Numerical and experimental investigation of the neutral atmospheric surface layer," J. Atmos. Sci., 64, 137–156.

Duman, T., Trakhtenbrot, A., Poggi, D., Cassiani, M., and Katul, G. G. (2016), "Dissipation Intermittency Increases Long-Distance Dispersal of Heavy Particles in the Canopy Sublayer," Boundary.-Layer Meteorol., 159, 41–68.

Ertel, H. (1942), "Der vertikale turbulenz-wärmestrom in der atmosphäre," Meteor. Z, 59, 250–253.

Finnigan, J. (2000a), "Turbulence in plant canopies," Annu. Rev. Fluid Mech., 32, 519–571.

Finnigan, J. (2000b), "Turbulence in plant canopies," Annu. Rev. Fluid Mech., 32, 519–571.

Frech, M. and Mahrt, L. (1995), "A two-scale mixing formulation for the atmospheric boundary layer," Boundary-Layer Meteorol., 73, 91–104.

Freire, L. S., Gerken, T., Ruiz-Plancarte, J., Wei, D., Fuentes, J. D., Katul, G. G., Dias, N. L., Acevedo, O. C., and Chamecki, M. (2017), "Turbulent mixing and removal of ozone within an Amazon rainforest canopy," J. Geophys. Res. Atmos., 122, 2791–2811, 2016JD026009.

Fuentes, J. D., Chamecki, M., dos Santos, R. M. N., Randow, C. V., Stoy, P. C., Katul, G., Fitzjarrald, D., Manzi, A., Gerken, T., Trowbridge, A., Freire, L. S., Ruiz-Plancarte, J., Maia, J. M. F., TÃşta, J., Dias, N., Fisch, G., Schumacher, C., Acevedo, O., Mercer, J. R., and YaÃśez-Serrano, A. M. (2016), "Linking Meteorology, Turbulence, and Air Chemistry in the Amazon Rain Forest," Bull. Amer. Meteor. Soc., 97, 2329–2342.

Galanti, B. and Tsinober, A. (2004), "Is turbulence ergodic?" Phys. Lett. A, 330, 173âĂŞ180.

Garratt, J. R. (1994), "Review: the atmospheric boundary layer," Earth-Sci. Rev., 37, 89–134.

Gerken, T., Ruddell, B. L., Fuentes, J. D., Araújo, A., Brunsell, N. A., Maia, J., Manzi, A., Mercer, J., dos Santos, R. N., von Randow, C., et al. (2017), "Investigating the mechanisms responsible for the lack of surface energy balance closure in a central Amazonian tropical rainforest," Agric. For. Meteorol.

Germano, M., Piomelli, U., Moin, P., and Cabot, W. H. (1991), "A dynamic subgrid-scale eddy viscosity model," Phys. Fluids, 3, 1760–1765.

Ghannam, K. and Konings, A. (2017), "On the correlation structure between surface soil moisture and vegetation water content with global carbon fluxes." To be submitted to: J. Hydrometeorol.

Ghannam, K., Poggi, D., Porporato, A., and Katul, G. G. (2015), "The spatio-temporal statistical structure and ergodic behaviour of scalar turbulence within a rod canopy," Boundary.-Layer Meteorol., 157, 447–460.

Ghannam, K., Nakai, T., Paschalis, A., Oishi, C. A., Kotani, A., Igarashi, Y., Kumagai, T., and Katul, G. G. (2016), "Persistence and memory timescales in root-zone soil moisture dynamics," Water Resour. Res., 52, 1427–1445.

Ghannam, K., Duman, T., Salesky, S. T., Chamecki, M., and Katul, G. (2017a), "The non-local character of turbulence asymmetry in the convective atmospheric boundary layer," Quart. J. Roy. Meteor. Soc., 143, 494–507.

Ghannam, K., Katul, G. G., Bou-Zeid, E., Gerken, T., and Chamecki, M. (2017b), "Scaling and similarity of the anisotropic coherent eddies in near-surface atmospheric turbulence." To be submitted to: J. Atmos. Sci.

Gleicher, S. C., Chamecki, M., Isard, S. A., Pan, Y., and Katul, G. G. (2014), "Interpreting three-dimensional spore concentration measurements and escape fraction in a crop canopy using a coupled EulerianâĂŞLagrangian stochastic model," Agric. For. Meteorol., 194, 118 – 131.

Gryanik, V. M. and Hartmann, J. (2002), "A turbulence closure for the convective boundary layer based on a two-scale mass-flux approach," J. Atmos. Sci., 59, 2729–2744.

Heinze, R., Mironov, D., and Raasch, S. (2016), "Analysis of pressure-strain and pressure gradient-scalar covariances in cloud-topped boundary layers: A large-eddy simulation study," J. ADV. MODEL. EARTH SY.

Higgins, C., Froidevaux, M., Simeonov, V., Vercauteren, N., Barry, C., and Parlange, M. (2012), "The effect of scale on the applicability of TaylorâĂŹs Frozen turbulence hypothesis in the atmospheric boundary layer," Boundary-Layer Meteorol., 143, 379–391.

Higgins, C., Katul, G., Froidevaux, M., Simeonov, V., and Parlange, M. B. (2013), "Are atmospheric surface layer flows ergodic?" Geophys. Res. Lett., 40, 3342âĂŞ3346.

Högström, U., Hunt, J., and Smedman, A.-S. (2002), "Theory and measurements for turbulence spectra and variances in the atmospheric neutral surface layer," Boundary.-Layer Meteorol., 103, 101–124.

Holtslag, A. and Boville, B. (1993), "Local versus nonlocal boundary-layer diffusion in a global climate model," J. Climate, 6, 1825–1842.

Holtslag, A. and Moeng, C.-H. (1991), "Eddy diffusivity and countergradient transport in the convective atmospheric boundary layer," J. Atmos. Sci., 48, 1690–1698.

Hsieh, C.-I. and Katul, G. G. (1997), "Dissipation methods, Taylor's hypothesis, and stability correction functions in the atmospheric surface layer," J. Geophys. Res., 102, 16391–16405.

Huang, C.-W., Launiainen, S., Grönholm, T., and Katul, G. G. (2014), "Particle deposition to forests: An alternative to K-theory," Atmos. Environ., 94, 593–605.

Huang, C.-W., Chu, C.-R., Hsieh, C.-I., Palmroth, S., and Katul, G. G. (2015), "Wind-induced leaf transpiration," Adv. Water Resour., 86, 240–255.

Hunt, J. and Carlotti, P. (2001), "Statistical structure at the wall of the high Reynolds number turbulent boundary layer," Flow Turbul. Combust., 66, 453–475.

Hutchins, N., Chauhan, K., Marusic, I., Monty, J., and Klewicki, J. (2012), "Towards reconciling the large-scale structure of turbulent boundary layers in the atmosphere and laboratory," Boundary-Layer Meteorol., 145, 273–306.

Jiménez, J. (2012), "Cascades in wall-bounded turbulence," Annu. Rev. Fluid Mech., 44, 27–45.

Jones, W. and Musonge, P. (1984), "Modelling of scalar transport in homogeneous turbulent flows," in 4th Symposium on Turbulent Shear Flows, vol. 1, p. 17.

Kaimal, J. C., Wyngaard, J. C., Izumi, Y., and CotÃľ, O. R. (1972), "Spectral characteristics of surface-layer turbulence," Quart. J. Roy. Meteor. Soc., 98, 563–589.

Katul, G. and Albertson, J. (1998), "An investigation of higher-order closure models for a forested canopy," Boundary-Layer Meteorol., 89, 47–74.

Katul, G. and Chu, C.-R. (1998), "A theoretical and experimental investigation of energy-containing scales in the dynamic sublayer of boundary-layer flows," Boundary-Layer Meteorol., 86, 279–312.

Katul, G., Kuhn, G., Schieldge, J., and Hsieh, C.-I. (1997a), "The ejection-sweep character of scalar fluxes in the unstable surface layer," Boundary-Layer Meteorol., 83, 1–26.

Katul, G., Hsieh, C.-I., and Sigmon, J. (1997b), "Energy-inertial scale interactions for velocity and temperature in the unstable atmospheric surface layer," Boundary.-Layer Meteorol., 82, 49–80.

Katul, G., Lai, C.-T., Schäfer, K., Vidakovic, B., Albertson, J., Ellsworth, D., and Oren, R. (2001), "Multiscale analysis of vegetation surface fluxes: from seconds to years," Adv. Water Resour., 24, 1119–1132.

Katul, G. G. (1994), "A model for sensible heat flux probability density function for near-neutral and slightly-stable atmospheric flows," Boundary-Layer Meteorol., 71, 1–20.

Katul, G. G., Finkelstein, P. L., Clarke, J. F., and Ellestad, T. G. (1996), "An investigation of the conditional sampling method used to estimate fluxes of active, reactive, and passive scalars," J. Appl. Meteorol., 35, 1835–1845.

Katul, G. G., Mahrt, L., Poggi, D., and Sanz, C. (2004), "One-and two-equation models for canopy turbulence," Boundary-Layer Meteorol., 113, 81–109.

Katul, G. G., Porporato, A., and Nikora, V. (2012), "Existence of k^{-1} power-law scaling in the equilibrium regions of wall-bounded turbulence explained by Heisenberg's eddy viscosity," Phys. Rev. E, 86, 066311.

Katul, G. G., Manes, C., Porporato, A., Bou-Zeid, E., and Chamecki, M. (2015), "Bottlenecks in turbulent kinetic energy spectra predicted from structure function inflections using the Von Kármán-Howarth equation," Phys. Rev. E, 92, 033009.

Katul, G. G., Banerjee, T., Cava, D., Germano, M., and Porporato, A. (2016), "Generalized logarithmic scaling for high-order moments of the longitudinal velocity component explained by the random sweeping decorrelation hypothesis," Phys. Fluids, 28, 095104.

Kolmogorov, A. N. (1941), "The local structure of turbulence in incompressible viscous fluid for very large Reynolds numbers," Dokl. Akad. Nauk SSSR, 30, 299–303.

Kumar, V., Kleissl, J., Meneveau, C., and Parlange, M. B. (2006), "Large-eddy simulation of a diurnal cycle of the atmospheric boundary layer: Atmospheric stability and scaling issues," Water. Resour. Res., 42.

Kunkel, G. J. and Marusic, I. (2006), "Study of the near-wall-turbulent region of the high-Reynolds-number boundary layer using an atmospheric flow," J. Fluid Mech., 548, 375–402.

Landau, L. D. and Lifshitz, E. M. (1980), Course of theoretical physics, Elsevier.

Lesieur, M. (1990), Turbulence in Fluids, Kluwer Acad., Dordrecht.

Li, D., Katul, G. G., and Gentine, P. (2016), "The kâĹŠ1 scaling of air temperature spectra in atmospheric surface layer flows," Quart. J. Roy. Meteor. Soc., 142, 496–505.

Manoli, G., Domec, J.-C., Novick, K., Oishi, A. C., Noormets, A., Marani, M., and Katul, G. (2016), "Soil-plant-atmosphere conditions regulating convective cloud formation above southeastern US pine plantations," Glob. Chang. Biol., 22, 2238–2254.

Marusic, I., McKeon, B. J., Monkewitz, P. A., Nagib, H. M., Smits, A. J., and Sreenivasan, K. R. (2010), "Wall-bounded turbulent flows at high Reynolds numbers: Recent advances and key issues," Phys. Fluids, 22, 065103.

Marusic, I., Monty, J. P., Hultmark, M., and Smits, A. J. (2013), "On the logarithmic region in wall turbulence," J. Fluid Mech., 716, R3.

Mattingly, J. and Weinan, E. (2001), "Ergodicity for the Navier-Stokes equation with degenerate random forcing: Finite-dimensional approximation," Comm. Pure Appl. Math., 54, 1386âĂŞ1402.

McComb, W. (2004), Renormalization methods: a guide for beginners., Clarendon Press.

Mellor, G. L. and Yamada, T. (1974), "A hierarchy of turbulence closure models for planetary boundary layers," J. Atmos. Sci., 31, 1791–1806.

Mellor, G. L. and Yamada, T. (1982), "Development of a turbulence closure model for geophysical fluid problems," Rev. Geophys., 20, 851–875.

Meneveau, C. and Marusic, I. (2013), "Generalized logarithmic law for high-order moments in turbulent boundary layers," J. Fluid Mech., 719.

Metzger, M. M. and Klewicki, J. C. (2001), "A comparative study of near-wall turbulence in high and low Reynolds number boundary layers," Phys. Fluids, 13, 692–701.

Mironov, D., Gryanik, V. M., Lykossov, V., and Zilitinkevich, S. (1999), "Comments on âĂIJA New Second-Order Turbulence Closure Scheme for the Planetary Boundary LayerâĂİ*," J. Atmos. Sci., 56, 3478–3481.

Mironov, D. V. (2001), "Pressure-potential-temperature covariance in convection with rotation," Quart. J. Roy. Meteor. Soc., 127, 89–110.

Moeng, C.-H. and Wyngaard, J. C. (1984), "Statistics of conservative scalars in the convective boundary layer," J. Atmos. Sci., 41, 3161–3169.

Moeng, C.-H. and Wyngaard, J. C. (1986), "An analysis of closures for pressure-scalar covariances in the convective boundary layer," J. Atmos. Sci., 43, 2499–2513.

Moeng, C.-H. and Wyngaard, J. C. (1989), "Evaluation of turbulent transport and dissipation closures in second-order modeling," J. Atmos. Sci., 46, 2311–2330.

Monin, A. (1970), "The atmospheric boundary layer," Annu. Rev. Fluid Mech., 2, 225–250.

Monin, A. and Yaglom, A. (1971), Statistical Fluid Mechanics: Mechanics of Turbulence, vol. 1, MIT Press.

Monin, A. and Yaglom, A. M. (1975), Statistical fluid mechanics: Mechanics of Turbulence. Vol. 2, vol. 2, MIT Press, Cambridge, MA, 874 pp.

Monin, A. S. and Obukhov, A. M. (1954), "Osnovnye zakonomernosti turbulentnogo peremesivanija v prizemnom sloe atmosfery," Trudy geofiz. inst. AN SSSR, 24, 163–187.

Nakagawa, H. and Nezu, I. (1977), "Prediction of the contributions to the Reynolds stress from bursting events in open-channel flows," J. Fluid Mech., 80, 99–128.

Nathan, R., Katul, G. G., Horn, H. S., Thomas, S. M., Oren, R., Avissar, R., Pacala, S. W., and Levin, S. A. (2002), "Mechanisms of long-distance dispersal of seeds by wind," Nat. Lett., 418, 409–413.

Nikora, V. (1999), "Origin of the " −1" Spectral Law in Wall-Bounded Turbulence," Phys. Rev. Lett., 83, 734–736.

Obukhov, A. (1949), "The local structure of atmospheric turbulence," Dokl. Akad. Nauk. SSSR, 67, 643–646.

Pan, Y. and Chamecki, M. (2016), "A scaling law for the shear-production range of second-order structure functions," J. Fluid Mech., 801, 459–474.

Pan, Y., Chamecki, M., and Nepf, H. M. (2016), "Estimating the Instantaneous Drag–Wind Relationship for a Horizontally Homogeneous Canopy," Boundary.-Layer Meteorol., 160, 63–82.

Perry, A. and Abell, C. (1977), "Asymptotic similarity of turbulence structures in smooth-and rough-walled pipes," J. Fluid Mech., 79, 785–799.

Perry, A., Henbest, S., and Chong, M. (1986), "A theoretical and experimental study of wall turbulence," J. Fluid Mech., 165, 163–199.

Poggi, D. and Katul, G. (2006), "Two-dimensional scalar spectra in the deeper layers of a dense and uniform model canopy," Boundary-Layer Meteorol., 121, 267 – 281.

Poggi, D. and Katul, G. (2007), "The ejection-sweep cycle over bare and forested gentle hills: a laboratory experiment," Boundary-Layer Meteorol., 122, 493–515.

Poggi, D., Porporato, A., and Ridolfi, L. (2002), "An experimental contribution to near-wall measurements by means of a special laser Doppler anemometry technique," Exp. Fluids, 32, 366–375.

Poggi, D., Porporato, A., Ridolfi, L., Albertson, J., and Katul, G. (2004a), "The effect of vegetation density on canopy sub-layer turbulence," Boundary-Layer Meteorol., 111, 565–587.

Poggi, D., Porporato, A., Ridolfi, L., Albertson, J., and Katul, G. (2004b), "The effect of vegetation density on canopy sub-layer turbulence," Boundary.-Layer Meteorol., 111, 565–587.

Poggi, D., Katul, G., and Albertson, J. (2004c), "Momentum transfer and turbulent kinetic energy budgets within a dense model canopy," Boundary-Layer Meteorol., 111, 589 – 614.

Poggi, D., Katul, G., and Albertson, J. (2006), "Scalar dispersion within a model canopy: measurements and three-dimensional Lagrangian models," Adv Water Resour., 29, 326–335.

Poggi, D., Katul, G., and Cassiani, M. (2008), "On the anomalous behavior of the Lagrangian structure function similarity constant inside dense canopies," Atmos. Environ., 42, 4212 – 4231.

Poggi, D., Katul, G., and Vidakovic, B. (2011), "The role of wake production on the scaling laws of scalar concentration fluctuation spectra inside dense canopies," Boundary-Layer Meteorol., 139, 83–95.

Prandtl, L. (1925), "Bericht über Untersuchungen zur ausgebildeten Turbulenz," Z. Angew. Math. Mech., 5, 136–139.

Priestley, C. and Swinbank, W. (1947), "Vertical transport of heat by turbulence in the atmosphere," in P. Roy. Soc. Lond. A Mat., vol. 189, pp. 543–561, The Royal Society.

Raupach, M. (1981), "Conditional statistics of Reynolds stress in rough-wall and smooth-wall turbulent boundary layers," J. Fluid Mech., 108, 363–382.

Raupach, M. R., Finnigan, J. J., and Brunet, Y. (1996), "Coherent Eddies and Turbulence in Vegetation Canopies: The Mixing-Layer Analogy," Boundary.-Layer Meteorol., 78, 351–382.

Rotta, J. (1951), "Statistische theorie nichthomogener turbulenz," Zeitschrift für Physik, 129, 547–572.

Salesky, S. T. and Chamecki, M. (2012), "Random errors in turbulence measurements in the atmospheric surface layer: implications for Monin–Obukhov similarity theory," J. Atmos. Sci., 69, 3700–3714.

Salesky, S. T., Chamecki, M., and Bou-Zeid, E. (2017), "On the Nature of the Transition Between Roll and Cellular Organization in the Convective Boundary Layer," Boundary.-Layer Meteorol., 163, 41–68.

Siebesma, A. and Cuijpers, J. (1995), "Evaluation of parametric assumptions for shallow cumulus convection," J. Atmos. Sci., 52, 650–666.

Siebesma, A. and Teixeira, J. (2000), "An advection-diffusion scheme for the convective boundary layer, description and 1D results," in Preprints, 14th Symp. on Boundary Layers and Turbulence, Aspen, CO, Amer. Meteor. Soc, vol. 4.

Siebesma, A. P., Soares, P. M., and Teixeira, J. (2007), "A combined eddy-diffusivity mass-flux approach for the convective boundary layer," J. Atmos. Sci., 64, 1230–1248.

Sreenivasan, K. R. and Antonia, R. (1997), "The phenomenology of small-scale turbulence," Annu. Rev. Fluid Mech., 29, 435–472.

Stanisic, M. (1985), Mathematical Theory of Turbulence, Springer, New York.

Stevens, R. J., Wilczek, M., and Meneveau, C. (2014), "Large-eddy simulation study of the logarithmic law for second-and higher-order moments in turbulent wall-bounded flow," J. Fluid Mech., 757, 888–907.

Stull, R. B. (1988), An introduction to boundary layer meteorology, vol. 13, Springer Science & Business Media.

Sutton, M., Schjorring, J., Wyers, G., Duyzer, J., Ineson, P., and Powlson, D. (1995), "Plant-Atmosphere Exchange of Ammonia [and Discussion]," Philos. Trans. Roy. Soc., 351, 261–278.

Taylor, G. (1938a), "The spectrum of turbulence," Proc. R. Soc. London Ser. A, 164, 476.

Taylor, G. I. (1938b), "The spectrum of turbulence," Proc. R. Soc. London A, 164, 476–490.

Tchen, C.-M. (1953), "On the spectrum of energy in turbulent shear flow," J. Res. Nat. Bur. Stand., 50, 51–62.

Townsend, A. (1961), "Equilibrium layers and wall turbulence," J. Fluid Mech., 11, 97–120.

Townsend, A. A. (1976), The structure of turbulent shear flow, Cambridge university press.

Troen, I. and Mahrt, L. (1986), "A simple model of the atmospheric boundary layer; sensitivity to surface evaporation," Boundary-Layer Meteorol., 37, 129–148.

UCAR/NCAR Earth Observing Laboratory (1990), " NCAR Integrated Surface Flux System (ISFS). NCAR/Earth Observing Laboratory," .

Vallikivi, M., Ganapathisubramani, B., and Smits, A. (2015), "Spectral scaling in boundary layers and pipes at very high Reynolds numbers," J. Fluid Mech., 771, 303.

van Dop, H. and Verver, G. (2001), "Countergradient transport revisited," J. Atmos. Sci., 58, 2240–2247.

Vercauteren, N., Bou-Zeid, E., Parlange, M. B., Lemmin, U., Huwald, H., Selker, J., and Meneveau, C. (2008), "Subgrid-Scale Dynamics of Water Vapour, Heat, and Momentum over a Lake," Boundary.-Layer Meteorol., 128, 205–228.

von Kármán, T. (1930), "Mechanische änlichkeit und turbulenz," Gött. Nachr., pp. 58–76.

von Kármán, T. and Howarth, L. (1938), "On the statistical theory of isotropic turbulence," Proc. R. Soc. Lond. A, 164, 192–215.

Wyngaard, J. C. and Brost, R. A. (1984), "Top-down and bottom-up diffusion of a scalar in the convective boundary layer," J. Atmos. Sci., 41, 102–112.

Wyngaard, J. C. and Clifford, S. F. (1977), "Taylor's Hypothesis and HighâĂŞFrequency Turbulence Spectra," J. Atmos. Sci., 34, 922–929.

Wyngaard, J. C. and Moeng, C.-H. (1992), "Parameterizing turbulent diffusion through the joint probability density," Boundary-Layer Meteorol., 60, 1–13.

Wyngaard, J. C. and Weil, J. C. (1991), "Transport asymmetry in skewed turbulence," Phys. Fluids, 3, 155–162.

Zeman, O. and Lumley, J. L. (1976), "Modeling buoyancy driven mixed layers," J. Atmos. Sci., 33, 1974–1988.

Zilitinkevich, S., Gryanik, V. M., Lykossov, V., and Mironov, D. (1999), "Third-Order Transport and Nonlocal Turbulence Closures for Convective Boundary Layers*," J. Atmos. Sci., 56, 3463–3477.

Biography

My name is Khaled Ghannam, born on November, 15, 1984, in Borgholia town, Tyr city, Lebanon. My Education is as follows:

- Ph.D., 2017, Duke University, North Carolina, USA
  Research focus: Surface Hydrology and Boundary-Layer Meteorology
- M.Sc. in Environmental Engineering, 2011, American University of Beirut, Lebanon
- B.Sc. in Physics, 2006, Beirut Arab University, Lebanon

Next position (July,2017 to July,2018): Postdoctoral Research Associate at the Department of Civil and Environmental Engineering, Princeton University, NJ, USA. I will be joining the Environmental Fluid Mechanics research group under the supervision of Prof. Elie Bou-Zeid.